

NORTHWESTERN UNIVERSITY

Observed Performance and Inverse Analysis of a Sheet Pile-Supported Excavation
in Chicago Clays

A DISSERTATION

SUBMITTED TO THE GRADUATE SCHOOL
IN PARTIAL FULFILLMENT OF THE REQUIREMENTS

for the degree

DOCTOR OF PHILOSOPHY

Field of Civil and Environmental Engineering

By

Sangrae Kim

EVANSTON, ILLINOIS

September 2018

© Copyright by Sangrae Kim 2018

All Rights Reserved

Abstract

Observed Performance and Inverse Analysis of a Sheet Pile-Supported Excavation in Chicago Clays

Sangrae Kim

When constructing buildings with basements in urban areas, the deformation levels during the excavation process must be carefully evaluated to prevent or minimize damage to adjacent structures. Because of uncertainties in predicting ground deformations during the design phase for a project, a robust monitoring program should be included in significant excavation projects. The adaptive management approach uses field data and updates key parameters affecting the computed deformation via numerical analysis during early stages of a construction project. The new parameters and subsequent numerical analyses form the basis of new simulations to predict responses of later stages. For this process, inverse analysis is carried out to optimize soil parameters based on the field observations. In this thesis, results of the inverse analysis method are used to study the effects of various soil models to predict lateral wall movements of a sheet pile-supported excavation in Chicago.

The ground and wall deformations of the Louis A. Simpson and Kimberly K. Querry Biomedical Research Center are summarized and evaluated in light of subsurface conditions,

construction activities and support system stiffness. The responses are compared with other nearby excavations and semi-empirical correlations.

Inverse analysis is carried out for the excavation process using three soil models in the clay layers, the Hardening Soil Model, the Hardening Soil Model with Small-Strain Stiffness and the Hypoplastic Constitutive Model. PLAXIS 2D is used for the finite element simulation of the excavation. Lateral deformations at the wall are used as the observations in the optimization. Optimized parameters are determined at various stages of the excavation to evaluate the most appropriate soil model for these conditions.

Acknowledgements

I would like to extend my deepest gratitude to my advisor, Professor Richard Finno, for his inspiration, guidance and support during my years at Northwestern. I also thank Professors Charles Dowding, Giuseppe Buscarnera and James Hambleton for their valuable suggestions, comments and advice.

I also want to acknowledge past and current members of the GeoGroup. Many thanks to all my other friends in Evanston, and also far away in Seoul.

Most importantly, I would like to thank my family. This work would not have been possible without the help and encouragement of my family. Their support has been an immense part of my life during my days at Northwestern.

Table of Contents

Chapter 1 Introduction	19
Chapter 2 Technical Background and Literature Review	21
2.1 Introduction	21
2.2 Adaptive Management Approach	22
2.3 Performance of Deep Excavations	23
2.4 Inverse Analysis	24
2.4.1 Objective Function	29
2.4.2 Parameter Selection for Optimization	30
2.4.2.1 Sensitivity Analysis	30
2.4.2.2 Correlation Analysis	31
2.4.3 Weights of Observations	33
2.5 Constitutive Soil Models	34
2.5.1 Hardening Soil Model (HS Model)	35
2.5.2 Hardening Soil Model with Small-Strain Stiffness (HSS Model)	36

	7
2.5.3 Hypoplastic Constitutive Model (HC Model)	40
2.6 Geotechnical Inverse Analysis: Literature Review	45
2.6.1 HS Model Optimization based on Field Observations at the Chicago-State Excavation	45
2.6.2 HS Model Optimization based on Field Observations at the Lurie Center Excavation	53
2.6.3 HS Model Optimization based on Field Observations at the Ford Center Excavation	56
2.6.4 Summary of HS Model Optimizations	59
2.6.5 HS and HSS Model Optimizations based on Field Observations at the Block 37 Excavation	60
2.6.6 HC Model Optimization	64
2.6.6.1 Laboratory Test Data Optimization	64
2.6.6.2 Application to OMPW Excavation	66
2.7 Summary	69

Chapter 3 Observed Performance of Louis A. Simpson and Kimberly K. Querry Biomedical Research Center	71
---	-----------

	8
3.1 Introduction	71
3.2 Site Description	72
3.2.1 Subsurface Conditions	72
3.2.2 Excavation Support System	74
3.2.3 Instrumentation	79
3.3 Construction Sequence	82
3.4 Traditional Inclinometer Data	86
3.5 Observed Performance	89
3.5.1 Settlements during Sheet Pile Installation	92
3.5.2 Movements during Excavation	94
3.5.2.1 Settlements Adjacent to North Wall	94
3.5.2.2 Lateral Wall Movements	98
3.5.3 Movements after Final Grade Attained	102
3.6 Evaluation of Measured Responses	103
3.6.1 Comparison with Other Excavation Performances	103
3.6.1.1 Settlement	104
3.6.1.2 Lateral Deformation	104
3.6.1.3 Comparison of Maximum Lateral and Vertical Deformations	106

3.6.1.4 Movements after Final Grade Attained	108
3.6.2 Evaluation of Performance through Semi-Empirical Method	108
3.7 Summary and Conclusions	111
Chapter 4 Optimizing Soil Parameters based on Lateral Wall Movements at SQBRC	113
4.1 Introduction	113
4.2 Problem Definition: 2D Finite Element Model	114
4.2.1 2D Mesh	115
4.2.2 Support System	116
4.2.3 Modeling Stages	119
4.2.4 Selection of Field Measurements	121
4.2.5 Estimates of Soil Parameters for Constitutive Models	123
4.2.5.1 HS Model	123
4.2.5.2 HSS Model	128
4.2.5.3 HC Model	134
4.3 Inverse Analysis	137
4.3.1 Parameter Selection for Optimization	137
4.3.1.1 Sensitivity Analysis	138

	10
4.3.1.2 Correlation Analysis	141
4.3.2 Optimized Soil Parameters	145
4.3.2.1 HS Model	145
4.3.2.2 HSS Model	150
4.3.2.3 HC Model	154
4.3.3 Comparison of Soil Models and Predictions	158
4.3.3.1 Evaluation of Fit	158
4.3.3.2 Prediction Capabilities	163
4.3.4 Time-Dependent Deformations	169
4.5 Summary and Conclusions	175
Chapter 5 Summary and Conclusions	179
5.1 Summary	179
5.2 Conclusions	181
References	185
Appendix	192

List of Tables

Table 2.1	Model parameters for the HS model	36
Table 2.2	Additional parameters used in the HSS model	38
Table 2.3	Reference model parameters for the HC model	40
Table 2.4	Small strain stiffness parameters for the HC model	42
Table 2.5	Small strain parameters for various clays	43
Table 2.6	Conventional calibration procedures for HS model parameters	46
Table 2.7	HS model parameters based on conventional calibration procedures	46
Table 2.8	HS model parameters based on optimization of laboratory data	47
Table 2.9	Initial values of HS model parameters for optimization based on field observations	49
Table 2.10	Optimized E_{50}^{ref} (kPa) values for each optimization stage	51
Table 2.11	Initial estimates of soil parameters for the HS model in the Lurie Center	54
Table 2.12	Optimized E_{50}^{ref} (kPa) values for the medium and stiff clay	55
Table 2.13	Initial estimates of soil parameters for the HS model in the Ford center	57
Table 2.14	Initial and final optimized E_{50}^{ref} (kPa) values for Ford Center	57
Table 2.15	Initial estimates of soil parameters for the HS model in Block 37	61

		12
Table 2.16	Initial additional HSS model parameters	62
Table 2.17	Optimized parameters for HS and HSS models	63
Table 2.18	HC model parameters optimized with laboratory test data	66
Table 2.19	HC model parameters of Chicago clays used for finite element model of OMPW	67
Table 3.1	Construction sequence	83
Table 3.2	Observed creep response in excavations in Chicago	108
Table 4.1	Structural properties of supports	117
Table 4.2	Modeling phases in relation to construction stages of Chapter 3	120
Table 4.3	Initial HS model parameters used for optimization	124
Table 4.4	E_{50}^{ref} (kPa) values optimized for various excavations in Chicago	124
Table 4.5	Initial HSS model parameters used for optimization	128
Table 4.6	Comparison of optimized Block 37 and initial SQBRC parameters	129
Table 4.7	Initial HC model parameters used for optimization	135
Table 4.8	Parameters with highest values of CSS based on sensitivity analysis	139
Table 4.9	Optimized E_{50}^{ref} values for HS model	145
Table 4.10	Optimized E_{50}^{ref} and $\gamma_{0.7}$ values for HSS model	146
Table 4.11	Optimized HS and HSS model parameters	152

Table 4.12	Comparison of optimized HSS model parameters from SQBRC and Block 37	153
Table 4.13	Optimized parameters for HC model	154
Table 4.14	Estimates of HC model large-strain parameters for various clays	155
Table 4.15	Estimates of HC model intergranular strain parameters for various clays	155
Table 4.16	RMSE values for computations using optimized parameters	162
Table 4.17	RMSE calculations of Stage 7 prediction using optimized parameters of SAA1Stage3,5	169
Table 4.18	Modeling phases including consolidation	170
Table 4.19	Permeabilities of clay layers	171
Table 4.20	Lateral wall movements (mm) for computations using various permeability cases	172
Table 4.21	Parameters optimized from undrained and consolidation-considered models ...	173

List of Figures

Figure 2.1	Adaptive Management Approach	23
Figure 2.2	Chart for estimating lateral wall movements for excavation support systems in clays (taken from Clough et al. 1989)	24
Figure 2.3	Inverse Analysis Procedure	26
Figure 2.4	Yield surface expansion due to plastic straining and yield cap surface (taken from Schanz et al. 1999)	35
Figure 2.5	Stiffness-strain behavior of soil with typical strain ranges (taken from Atkinson and Salfors 1991)	37
Figure 2.6	Small strain overlay and cut-off of degradation curve used in HSS model (taken from PLAXIS 2016)	39
Figure 2.7	Definition of model parameters λ^* , κ^* and N (taken from Masin 2005)	41
Figure 2.8	Calibration of constitutive parameters for the HC model with intergranular strains (taken from Masin 2011)	44
Figure 2.9	Visual fit between experimental and computed results (taken from Calvello and Finno 2004)	47

Figure 2.10	Measured and computed lateral displacements using initial parameters (taken from Calvello 2002)	50
Figure 2.11	Measured and computed lateral displacements using parameters based on Stage 1 observations (taken from Calvello 2002)	52
Figure 2.12	Measured and computed lateral displacements using parameters based on Stage 3 observations (taken from Calvello 2002)	53
Figure 2.13	Fit between observed and calculated displacements using optimized parameters (taken from Rechea 2006)	55
Figure 2.14	Observed and calculated displacements (taken from Rechea 2006)	58
Figure 2.15	E_{50}^{ref} in Deerfield vs. shear strain level for optimization cases (taken from Rechea 2006)	60
Figure 2.16	Inclinometer measurements used in optimization (taken from Mu et al. 2015)	63
Figure 2.17	Observed and computed results with the PLAXIS model of OMPW (taken from Arboleda-Monsalve 2014)	68
Figure 3.1	Subsurface conditions of SQBRC and Lurie Center	74
Figure 3.2	Earth retention systems along north and south walls	75
Figure 3.3	West-east cross-sectional view of retention systems	76

		16
Figure 3.4	Instrumentation plan for SQBRC	80
Figure 3.5	Access ramp along south wall	84
Figure 3.6	Excavated grade and micropile installation positions	85
Figure 3.7	Inclinometer measurements	87
Figure 3.8	Overview of lateral movements	90
Figure 3.9	Localized effects of micropile installation	92
Figure 3.10	Total settlement after sheet pile installation (at Stage 3)	93
Figure 3.11	Total settlement at Stage 5	95
Figure 3.12	Total settlement at Stage 7	95
Figure 3.13	Total settlement at Stage 9	96
Figure 3.14	Incremental settlement from Stage 3 to Stage 5	97
Figure 3.15	Incremental settlement from Stage 3 to Stage 7	97
Figure 3.16	Incremental settlement from Stage 3 to Stage 9	98
Figure 3.17	Lateral deformation of north wall with excavation stage	99
Figure 3.18	Lateral deformation of south wall with excavation stage	100
Figure 3.19	Lateral wall movements at end of mass excavation	105
Figure 3.20	Maximum lateral wall movements and maximum settlement	107
Figure 3.21	Computed and measured normalized wall movements	

		17
	(adopted from Clough et al. 1989)	109
Figure 4.1	Finite element mesh of north-south cross section of SQBRC	115
Figure 4.2	Deformations for SAA-1 used in inverse analysis	122
Figure 4.3	Computations of lateral deformation using initial HS parameters	127
Figure 4.4	Shear velocity data obtained from cross hole tests (taken from Finno et al. 2012)	130
Figure 4.5	G_0 calculated from shear velocity data vs. G_0 with depth calculated from assumed G_0^{ref} values	131
Figure 4.6	Computations of lateral deformation using initial HSS parameters	133
Figure 4.7	Computations of lateral deformation using initial HC parameters	136
Figure 4.8	CSS for Blodgett/Deerfield and Park Ridge for all optimization stages	140
Figure 4.9	PCC for Blodgett/Deerfield at SAA1Stage3	142
Figure 4.10	PCC for Blodgett/Deerfield at SAA1Stage3,5	142
Figure 4.11	PCC for Blodgett/Deerfield at SAA1Stage3,5,7	143
Figure 4.12	PCC for Park Ridge at SAA1Stage3	143
Figure 4.13	PCC for Park Ridge at SAA1Stage3,5	144
Figure 4.14	PCC for Park Ridge at SAA1Stage3,5,7	144
Figure 4.15	Shear strains corresponding to Stage 3	146

Figure 4.16	Shear strains corresponding to Stage 5	146
Figure 4.17	Shear strains corresponding to Stage 7	147
Figure 4.18	Optimized E_{50}^{ref} values of Blodgett/Deerfield with predominant shear strain ...	149
Figure 4.19	Optimized E_{50}^{ref} values of Blodgett/Deerfield with maximum lateral deformation	149
Figure 4.20	G^{ref} with shear strain using Blodgett/Deerfield optimized parameters	151
Figure 4.21	G^{ref} with shear strain using Park Ridge optimized parameters	151
Figure 4.22	Computed deformations using different optimization parameters	157
Figure 4.23	Deformations based on SAA1Stage3 optimization	159
Figure 4.24	Deformations based on SAA1Stage3,5 optimization	160
Figure 4.25	Deformations based on SAA1Stage3,5,7 optimization	161
Figure 4.26	Prediction capabilities of HS model	164
Figure 4.27	Prediction capabilities of HSS model	165
Figure 4.28	Prediction capabilities of HC model	167
Figure 4.29	Measurements and predictions of Stage 7 based on SAA1Stage3,5 optimization	168
Figure 4.30	Computed deformation using optimized parameters from SAA1Stage3,5,7	174

Chapter 1 Introduction

When constructing buildings with basements in urban areas, the deformation levels during the excavation process must be carefully evaluated to prevent or minimize damage to adjacent structures. Because of uncertainties in predicting ground deformations during the design phase for a project, a robust monitoring program should be included in significant excavation projects. The adaptive management approach uses field data and updates key parameters affecting the computed deformation via numerical analysis during early stages of a construction project. The new parameters and subsequent numerical analysis forms the basis of new simulations to predict responses at later, and potentially more critical stages of construction.

Inverse analysis procedures can be used to make parameter updates based on observations collected during the early stages of an excavation. Inverse analysis has been employed in conjunction with finite element simulations in the past to produce realistic and reliable results for performance-based geotechnical problems. This thesis will focus on an inverse analysis of data collected from a sheet pile-supported excavation in Chicago. Field measurements collected at various stages of the excavation and finite element model computations of the lateral soil deformation at those times are used to evaluate the effects of three soil models on the methodology.

Chapter 2 presents the technical background for the work conducted as part of this thesis. The adaptive management approach is introduced, and a brief summary of past studies on the performance of deep excavations is presented. The inverse analysis method based on the gradient method is described in detail. Three constitutive soil models considered in this thesis are

summarized and previous studies of inverse analysis applied to Chicago soils using these soil models are summarized.

Chapter 3 analyzes the observed performance of the Louis A. Simpson and Kimberly K. Query Biomedical Research Center (SQBRC) located in downtown Chicago. The measured ground and wall responses are described and correlated with construction activities. The responses are evaluated in light of subsurface conditions, support system stiffness and other nearby excavations. The expected performance based on semi-empirical correlations are compared with the measured response.

Chapter 4 describes the inverse analysis results that were carried out for the SQBRC excavation. PLAXIS 2D is used to simulate the plane strain conditions. The Hardening Soil Model (HS model), the Hardening Soil Model with Small-Strain Stiffness (HSS model) and the Hypoplastic Constitutive Model (HC model) are used to represent the two clay layers of interest. The HS model is chosen due to its simplicity and the wide application on Chicago clays in past case studies. The HSS and HC models are chosen due to their consideration on small-strain stiffness. Soil parameters optimized in early stages of the project are used to predict the soil deformation of later stages. Predictions made by the three soil models are compared and analyzed. In addition to the undrained finite element simulations, consolidation effects are numerically considered to assess the time-dependent deformations that are observed in the field measurements.

Chapter 5 summarizes the thesis, and presents conclusions based on this research.

Chapter 2 Technical Background and Literature Review

2.1 Introduction

It is crucial to minimize or prevent damage to adjacent structures and utilities while making deep excavations in urban environments. For this purpose, one must evaluate ground responses during the entire construction process. To make predictions and assess performance of supported excavations, the use of finite element modeling (FEM) has steadily increased. When properly executed, these finite element models may produce realistic and reliable results which are very useful for these projects.

Ground movements caused by excavations are affected by many factors including stratigraphy, soil properties, support system details, construction activities and workmanship. While numerical simulations have become more common to analyze the ground response to excavations as part of the design process, finite element predictions contain uncertainties related to soil properties, support system details and construction procedures. If one wants to predict and subsequently evaluate the overall performance of a design, a procedure must be defined that incorporates a quantitative means to evaluate the results of the predictive analysis. The procedure to accomplish this is referred to as the “observational method” (Peck 1969, Morgenstern 1995, Whitman 2000), a framework wherein construction and design features are adjusted based on field measurements made as construction proceeds.

This chapter presents a brief literature review of performance of deep excavations and inverse analysis techniques used for the application of the adaptive management approach, in

essence, an automated observational approach, to practical geotechnical problems. Case studies of inverse analyses carried out for Chicago clays also are summarized.

2.2 Adaptive Management Approach

Efforts to properly monitor, simulate and predict the performance of excavations have led to the enhancement of the observational approach, allowing a cycle of measurement and prediction update in near real time. This enhancement, called “adaptive management”, can be used to predict, monitor and control the performance during geotechnical constructions (e.g., Finno 2007, Finno 2008, Finno et al., 2017). After data sets are collected at early stages of a project, updated parameters form the basis of new simulations to predict responses at later, and potentially more critical stages of construction.

Figure 2.1 summarizes the adaptive management process. A finite element or difference code can be used as the platform for the numerical analysis. Field performance data is collected during the field monitoring of the construction process. Using the measured and computed outputs of past and current construction stages, soil parameters can be optimized by minimizing the difference between the two outputs. If the updated predictions based on the optimized soil parameters indicate that movements will be larger than allowed in the design, problems foreseen in the design of the latter stages may be mitigated by countermeasures planned in advance to prevent major damage to adjacent structures or utilities. This thesis will focus on inverse analysis using data from supported excavations. Details of the inverse analysis procedure used in this thesis are presented in Section 2.4.

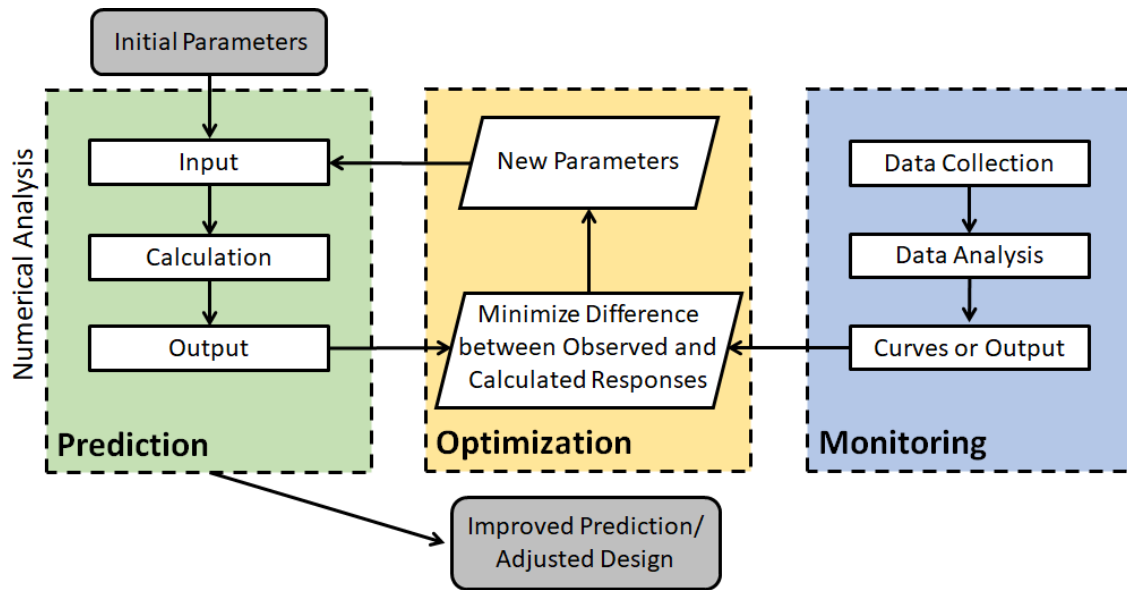


Figure 2.1 Adaptive management approach

2.3 Performance of Deep Excavations

Field measurements of deep excavations in urban areas are collected to ensure that the impacts of these deep excavations on adjacent structures are minimized. These field measurements must be evaluated in light of various construction activities to assess the effects of the individual activities. For this purpose, factors that influence the performance including system stiffness, subsurface conditions, excavation sequence and workmanship, and other related construction activities (e.g., pile driving, caisson installation or removal of existing foundations) must be properly understood.

Numerous empirical studies on the performance of deep excavations have been reported (e.g., Peck 1969, Lambe 1970, Goldberg et al. 1976, O'Rourke 1981, Clough and O'Rourke 1990).

Studies showed that factors such as soil type, depth of excavation, workmanship, stiffness of supports, timing and preloading of supports, and other construction activities such as dewatering and deep foundation installations may largely impact the performance of deep supported excavations. These empirical studies are beneficial as they capture the effects of many secondary construction activities that are not considered in numerical processes.

Clough et al. (1989) presented a semi-empirical design chart applicable to excavations in clay where the maximum lateral wall movements were related to the support system stiffness and factor of safety against basal heave (Figure 2.2).

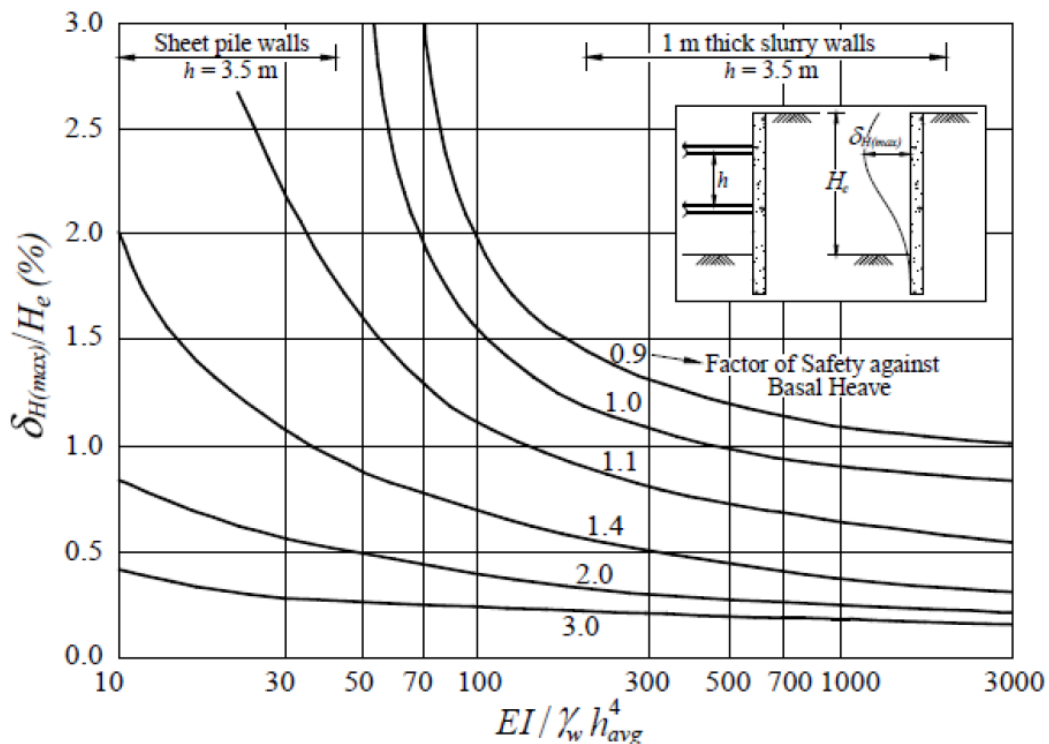


Figure 2.2 Chart for estimating lateral wall movements for excavation support systems in clays
(taken from Clough et al. 1989)

In this chart, the factor of safety against basal heave proposed by Terzaghi (1943) was employed. The system stiffness, η , is defined as:

$$\eta = \frac{EI}{\gamma_w h^4} \quad (2.1)$$

where E is the Young's modulus of the wall material, I is the moment of inertia of the wall, h is the average spacing between support levels, and γ_w is the unit weight of water used as a normalizing factor. The Clough et al. chart was developed based on numerical modeling, and does not consider the secondary construction activities that may have impacted results in empirical studies.

The following factors are the most influential for the performance of deep excavations (e.g., Peck 1969, Lambe 1970, O'Rourke 1981, Goldberg et al. 1976, Clough et al. 1989, Clough and O'Rourke 1990, Finno and Bryson 2002, Bryson and Zapata-Medina 2012): (a) soil type and properties, (b) construction sequence and technique, workmanship, and secondary construction activities, (c) geometry of the excavation, (d) stiffness of the support system, and (e) consolidation of clays.

2.4 Inverse Analysis

In inverse analysis, changes are iteratively made in parts of a model until the optimized model adequately represents the actual system. Figure 2.3 shows a schematic of an inverse analysis procedure for updating performance predictions during deep excavations.

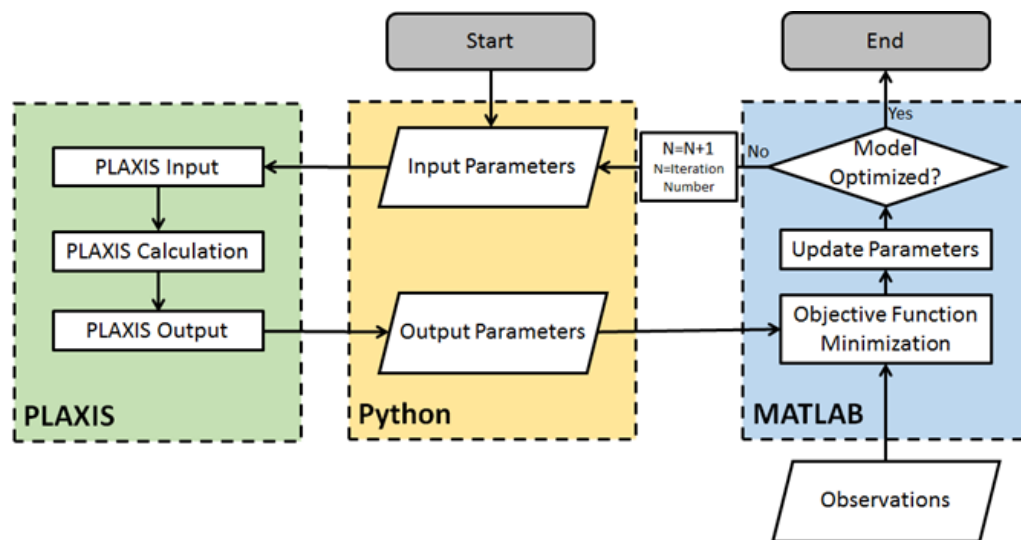


Figure 2.3 Inverse analysis procedure

The initial input parameters are assessed by conventional means (e.g., laboratory data and/or field test results). Next a numerical simulation of the problem is made and the outputs, lateral wall deformations for this thesis, are stored. The computed results are then compared to the field observations and a regression analysis is performed to minimize the “objective function.” The objective function quantifies the fit between computed and measured results. The model fit is considered an “optimal solution” either when parameter values change less than a preset fractional

amount between iterations or when perturbations in the input parameters change the objective function values by less than a preset fractional amount (e.g., 0.1 %). Regressions are repeated until an optimum fit is reached.

Optimization may be conducted with inverse analysis based on a gradient method. Herein, it is accomplished by coupling the optimization toolbox in MATLAB with the finite element code PLAXIS. A program is written in PYTHON to transfer data between PLAXIS and MATLAB. The program is provided in the Appendix. A Gauss-Newton method modified by the addition of damping and Marquardt parameters is used to find a best fit between the computed and observed values, as defined by a weighted least-squares objective function, $S(b)$. Parameters used in the non-linear regression analysis are presented in detail by Calvello (2002) and Rechea (2006).

The benefit of inverse modeling is its ability to automatically calculate parameter values that produce the best fit between observed and computed results (e.g., Ou and Tang 1994, Ledesma et al. 1996, Finno and Calvello 2005, Hashash and Finno 2008). Through this automated process, time is substantially saved compared to trial-and error methods. Inverse analysis also provides statistical quantities that indicate the quality of a calibration. However, convergence by inverse analysis does not necessarily mean that the finite element simulation is properly calibrated. For a model to be considered “reliably” calibrated, not only the fit between computed and observed results must be satisfactory (i.e., errors are within desired and/or accepted accuracy) but also the best-fit values of the parameters must be reasonable and within those expected for the soil (Finno et al. 2017).

Optimizations based on the gradient method allows convergence to the same set of parameter values even when the regression starts from different initial points; if all the

optimizations converge to the same set of parameter values, then the solution can be considered unique (Rechea 2006). Uniqueness is a difficulty inherent to inverse modeling algorithms applied to complex real systems. Because systems are non-linear, sometimes problems arise, such as (a) insensitivity, when the observations do not contain enough information to support estimation of parameters, (b) non-uniqueness, when different combinations of parameter values match the observations equally well and (c) instability, when slight changes in model variables radically change optimization results (Calvello 2002).

When solving inverse analysis problems, the sources of error must be taken into consideration (e.g., Calvello 2002, Finno et al. 2017). Uncertainties arise from approximations made when converting a physical system to a numerical model, assumptions made in the analysis procedure, and the final subjective judgement of the results of analysis. For geotechnical problems, the following uncertainties must be considered: (a) modeling error due to geometry, boundary conditions and the constitutive models used, (b) accuracy and reliability of the field observations, and (c) numerical errors present throughout the entire inverse analysis process. For the work presented in this thesis, it will be assumed that the errors in the modeling due to the geometry and boundary conditions are negligible. The accuracy and reliability of the field measurements will be considered through implementation of a weighting function. In this thesis, it will be assumed that the only uncertainty is the material response characterized by various constitutive soil models, and all other factors are known and contain no errors.

2.4.1 Objective Function

The fit between calculations and measurements is assessed through an objective function, $S(b)$. Optimized parameters are those that minimize the objective function. In inverse analysis, the parameters that minimize the objective function may be found by a number of ways:

- Deterministic: Trial-and-error process is conventionally used.
- Statistical: Procedures such as (a) the weighted least-squares method and (b) the simple least-squares method are employed.

A common expression for the objective function with no prior information is:

$$S(b) = [y - y'(b)]^T \cdot \underline{w} \cdot [y - y'(b)] \quad (2.2)$$

where y indicates the observation; $y'(b)$ is the computed quantity of the observed parameter; \underline{w} is the covariance operator that reflects errors in the measurements. Equation 2.2 refers to the weighted least squares method. Within this thesis, this weighted least squares method is used for the objective function calculations.

The goal of inverse analysis is to minimize the $S(b)$ value, and thus produce an optimum fit between the computed and measured values. However, when the objective function has multiple local optimum points, or the function is flat around the optimum point making convergence unsuccessful, inverse analyses suffer from non-uniqueness and instability of the solutions. These limitations come not only from the physical nature of the problem, but also from the limited quantity and poor quality of observations (Honjo et al. 1994). To help overcome these limitations, the inverse analyses within this thesis only employ reasonable observations of good quality.

2.4.2 Parameter Selection for Optimization

Optimization-related statistics provide information regarding which parameters can be estimated through optimization with respect to particular field observations and whether certain parameters can be estimated simultaneously (e.g., Calvello and Finno 2004, Finno et al. 2017). Two statistics used in this work are the Composite Scaled Sensitivity (CSS) and the Parameter Correlation Coefficient (PCC).

2.4.2.1 Sensitivity Analysis

The relative importance of the model parameters being simultaneously estimated can be defined using the Composite Scaled Sensitivity (CSS), and is defined as:

$$CSS_j = \left[\sum_{i=1}^{ND} \left(\frac{\partial y'_i}{\partial b_j} b_j w_{ii}^{1/2} \right)^2 / ND \right]^{1/2} \quad (2.3)$$

where y'_i is the i^{th} computed value; b_j is the j^{th} estimated parameter; $\partial y'_i / \partial b_j$ is the sensitivity of the i^{th} computed value with respect to the j^{th} parameter; w_{ii} is the weight of the i^{th} observation, and ND is the number of observations. Forward difference sensitivities are used for the sensitivity analysis calculations:

$$\frac{\partial y'_i}{\partial b_j} \approx \frac{\Delta y'_i}{\Delta b} = \frac{y'(b + \Delta b) - y'(b)}{\Delta b} \quad (2.4)$$

For non-linear problems, the sensitivities depend on the parameter values and the type of problem, so the CSS_j will be different for different initial parameter values. In addition, because

of the approximate way the sensitivities are calculated, their accuracy depends on the size of the parameter perturbations. A parameter perturbation that is too large can yield inaccurate sensitivities for non-linear parameters. However, perturbations that are too small can result in negligible differences if the extracted values or differences are obscured by round-off error (Poeter and Hill, 1998). Determining the appropriate perturbation size can be problematic and it is necessary to experiment with different values. For past work done by Rechea (2006), parameter perturbations of 0.01 (1 %) generally worked well. Therefore, perturbations of 0.01 are also employed in this thesis.

2.4.2.2 Correlation Analysis

Multicollinearity is a term used in multi-regression analysis where strong intercorrelations are found among the variables which would result in very high correlation among the regression coefficients, and thus makes it difficult to interpret the result (Honjo et al. 1994). Parameter correlation coefficients indicate whether the estimated parameter values are likely to be unique, and whether the parameters may be optimized at the same time.

The correlation coefficients are calculated from the Variance-Covariance matrix $\underline{V}(\underline{b}')$ for the estimated parameters \underline{b}' :

$$\underline{V}(\underline{b}') = s^2 \cdot (\underline{X}^T \cdot \underline{w} \cdot \underline{X})^{-1} \quad (2.5)$$

where $\underline{V}(\underline{b}')$ is an NP by NP matrix; \underline{X} is the sensitivity matrix; \underline{w} is the weighting matrix for the observations; and s^2 is the calculated error variance, which equals:

$$s^2 = \frac{S(b)}{ND - NP} \quad (2.6)$$

where $S(b)$ is the objective function; ND is the number of observations; and NP is the number of estimated parameters. The diagonal elements of matrix $\underline{V}(\underline{b}')$ indicate the parameter variances; the off-diagonal elements are the parameter covariances. For a problem with three estimated parameters, the matrix would appear as:

$$\underline{V}(\underline{b}')$$

$$= \begin{bmatrix} \text{var}(1) & \text{cov}(1,2) & \text{cov}(1,3) \\ \text{cov}(2,1) & \text{var}(2) & \text{cov}(2,3) \\ \text{cov}(3,1) & \text{cov}(3,2) & \text{var}(3) \end{bmatrix} \quad (2.7)$$

where $\text{var}(1)$ is the variance of parameter 1, $\text{cov}(1,2)$ is the covariance between parameters 1 and 2, and so on. The variance-covariance matrix is symmetric, so that $\text{cov}(1,2) = \text{cov}(2,1)$.

Parameter Correlation Coefficient (PCC) values are calculated as the covariance between two parameters divided by the product of their standard deviation. The correlation between the i^{th} and the j^{th} parameter is calculated as:

$$PCC = \text{cor}(i, j) = \frac{\text{cov}(i, j)}{\text{var}(i)^{1/2} \cdot \text{var}(j)^{1/2}} \quad (2.8)$$

PCC values range from -1.0 to 1.0, with values close to -1.0 and 1.0 indicating parameter values that cannot be uniquely estimated. Values above 0.9, in absolute value, indicate high correlations between the two considered parameters, and will result in unrealistic parameters when estimated simultaneously.

2.4.3 Weights of Observations

For the proper implementation of inverse analysis using field instrumentations, the solution must depend on weighting factors reflecting measurement errors. Weights allow one to use different types of data in an optimization, because the weighting function depends on the standard deviation of the measurement. Details are presented by Rechea (2006).

Measurement errors can be identified by the instrument's repeatability. Repeatability of Shape Acceleration Arrays (SAAs) indicates how close readings can come to the same reading each time the SAAs are read. When measuring lateral soil and wall movements, repeatability is the factor of interest, because how much the SAA moved relative to its original reading is of interest.

Based on the manufacturer's specifications, the system repeatability of the SAAs employed in this thesis were 1.5 mm / 32 m. The bottom of a SAA is assumed fixed and thus should be placed in a stratum that is not expected to move. The distance from the fixed bottom and the repeatability were used to calculate the weights of measurement points with varying depth (Appendix). As a result, SAA readings close to the bottom of the SAA were assigned larger weights compared to readings made at shallower depths.

2.5 Constitutive Soil Models

Three soil models will be used to represent the stress-strain-strength behavior of clay layers in the finite element simulations of this thesis. Because one of the objectives of this research is to develop tools or guidelines for geotechnical finite element simulations of excavations that are accessible to engineering practitioners, the potential candidates for constitutive models were restricted to models that have been implemented in commercial computer codes.

Nonlinear constitutive soil models that are considered herein include the Hardening Soil Model (HS model), the Hardening Soil Model with Small-Strain Stiffness (HSS model) and the Hypoplastic Constitutive Model (HC model). Although the HS model does not capture the nonlinear stiffness at small strain levels, the model has been used extensively in the past by researchers and in industry. The HSS model includes the ability to represent the nonlinear response at small strains. The HC model is not developed using the elastoplastic framework but is based on the hypoplastic laws presented by Kolymbas (1991). The HS and HSS models have been used in inverse analysis with field measurement data from several sites in downtown Chicago (e.g., Calvello 2002, Finno and Calvello 2005, Rechea 2006, Mu et al. 2015, Mu and Huang 2016). The HC model has been applied to Chicago glacial clays using only triaxial test data (Sarabia 2012) but not field measurement data.

The following sections briefly summarize the three soil models used herein. References are provided in which the interested reader can find complete details of the formulations.

2.5.1 Hardening Soil Model (HS Model)

The HS model is an elasto-plastic model with multiple yield surfaces that can expand due to plastic straining (Schanz et al., 1999) up to a failure condition. The HS model employs the Mohr-Coulomb (M-C) failure criteria (Figure 2.4). Two types of hardening are implemented in the HS model: shear hardening and compression hardening. Shear hardening models the irreversible plastic strains due to primary deviatoric loading. Increments of plastic strain are non-associative on the shearing yield surface, and are controlled by the plastic potential, γ_p . Compression hardening models the irreversible plastic volumetric strains due to primary compression and is controlled by a yield cap surface (Figure 2.4). The flow rule is associative on this yield cap. The cap yield surface expands as a function of pre-consolidation stress. The basic parameters for the HS model are listed in Table 2.1.

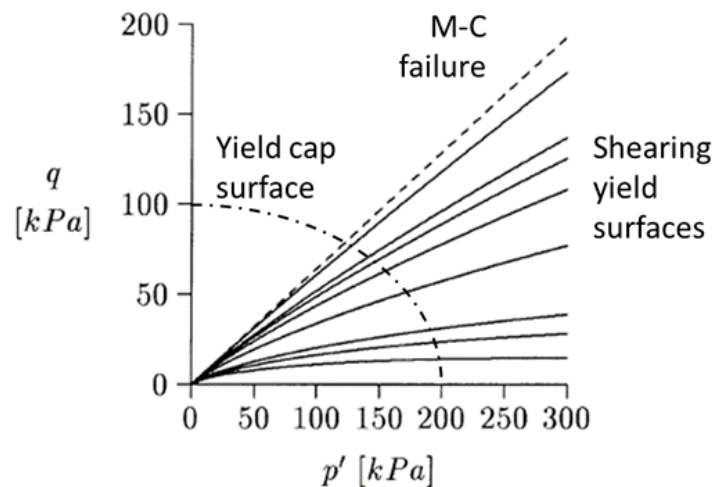


Figure 2.4 Yield surface expansion due to plastic straining and yield cap surface

(taken from Schanz et al. 1999)

Table 2.1 Model parameters for the HS model

Model parameter	Description
m	Power law coefficient incorporating stress dependent stiffness
E_{50}^{ref}	Models plastic straining due to primary deviatoric loading
$E_{\text{oed}}^{\text{ref}}$	Models plastic straining due to primary compression
$E_{\text{ur}}^{\text{ref}}, \nu_{\text{ur}}$	Elastic unloading/reloading parameters
c, φ, ψ	Failure parameters

The main advantage of the HS model is the stress level dependency of soil stiffness. The reference moduli are stress-dependent stiffness parameters for deviatoric, constrained compression and unloading/reloading, and are calculated by:

$$E^{\text{ref}} = E \left(\frac{c \cos \varphi - \sigma_3' \sin \varphi}{c \cos \varphi + p^{\text{ref}} \sin \varphi} \right)^{-m} \quad (2.9)$$

where E^{ref} values represent the reference stiffness values at the reference confining pressure, p^{ref} . The actual stiffness depends on the minor principal stress, which is the confining pressure in drained, isotropic compression. The degree of stress dependency is described by the power m . In the equation, compressive stresses are taken as negative.

2.5.2 Hardening Soil Model with Small-Strain Stiffness (HSS Model)

The HS model assumes elastic behavior during unloading and reloading. However, the range in which soils can be considered truly elastic is limited to very small strains. With increasing strain, nonlinear decay of soil stiffness is observed (Figure 2.5). The figure shows the characteristic shear strains that are representative of those that develop near geotechnical structures and the

applicable strain ranges that can be measured in various laboratory tests. At the minimum strain that can be measured in conventional (e.g., triaxial) laboratory tests, the soil stiffness has often decreased to less than half the initial actual value.

When trying to compute relatively small deformations associated with wall design and geotechnical structures, the soil stiffness that should be used is not the one that corresponds to the relatively larger strain at the end of construction. For better evaluations of the soil response during excavations, very small-strain stiffness and its non-linear dependency on strain should be properly represented in a constitutive model.

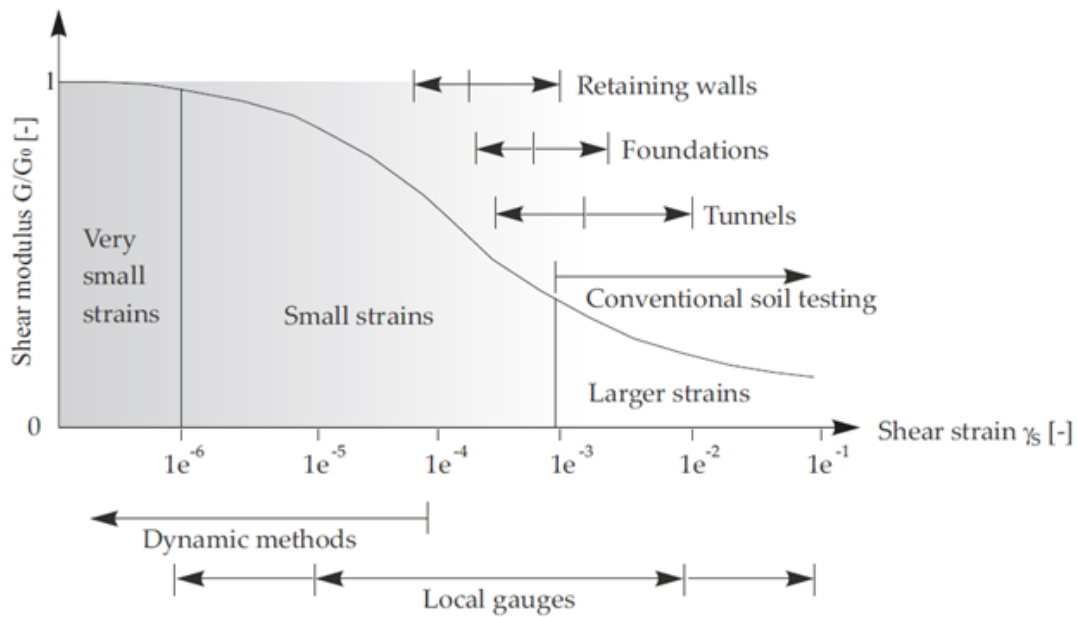


Figure 2.5 Stiffness-strain behavior of soil with typical strain ranges

(taken from Atkinson and Salfors 1991)

The HSS model was developed by Benz (2006) and allows for direct representation of these very small strains. It also includes all the features of the HS model. In addition to the same parameters as the HS model uses, two more variables are included to describe the variation of stiffness with strain (Table 2.2).

Table 2.2 Additional parameters used in the HSS model

Model parameter	Description
G_0	Initial (very small-strain) shear modulus
$\gamma_{0.7}$	Shear strain level where the secant shear modulus is reduced to 70% of G_0

For small-strain stiffness, the HSS model employs the well-known Hardin-Drnevich relationship (Hardin and Drnevich 1972). From test data, the stress-strain curve can be adequately described by a hyperbolic law. The shear strain at which the secant shear modulus is reduced to approximately 70% of its initial value, $\gamma_{0.7}$, is used as a model parameter:

$$\frac{G_t}{G_0} = \frac{1}{\left(1 + 0.385 \left| \frac{\gamma}{\gamma_{0.7}} \right| \right)^2} \quad (2.10)$$

where G_t is the tangent shear modulus and γ is the considered shear strain.

The extension of the HS model to the HSS model has been proposed by Benz (2006) in the form of a small-strain overlay model. The lower cut-off of G_t is introduced at the unloading-reloading stiffness G_{ur} which is defined by the material parameters E_{ur} and ν_{ur} :

$$G_t \geq G_{ur} \text{ where } G_{ur} = \frac{E_{ur}}{2(1+\nu_{ur})} \text{ and } G_t = \frac{E_t}{2(1+\nu_{ur})} \quad (2.11)$$

An example of the stiffness reduction curve is shown in Figure 2.6.

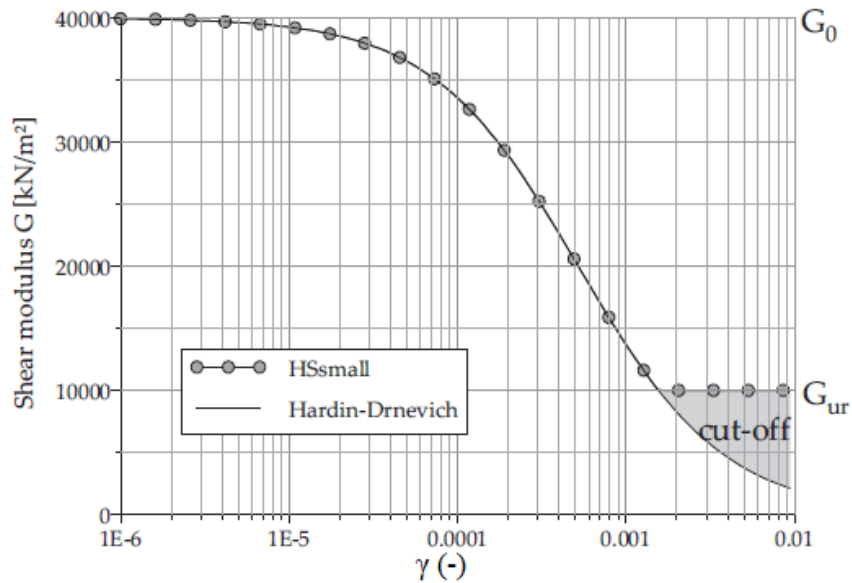


Figure 2.6 Small strain overlay and cut-off of degradation curve used in HSS model
(taken from PLAXIS 2016)

As in the HS model, the reference moduli, E^{ref} are stress-dependent stiffness parameters for deviatoric, constrained compression and unloading/reloading. The G^{ref} values are calculated in the same fashion as:

$$G^{ref} = G \left(\frac{c \cos \varphi - \sigma_3' \sin \varphi}{c \cos \varphi + p^{ref} \sin \varphi} \right)^{-m} \quad (2.12)$$

2.5.3 Hypoplastic Constitutive Model (HC Model)

The HC model for clays proposed by Masin (2014) is a model that uses basic principles of critical state soil mechanics to represent the behavior of fine grained soils following different stress paths. The model is not based on a conventional elasto-plastic framework that decomposes strains in elastic and plastic components, and therefore does not involve complex yield surface and plastic potential definitions. The model captures the nonlinear behavior of soils at large strains in the framework of critical state soil mechanics by means of the Matsuoka-Nakai shape of the critical state locus in the stress space.

The reference model (Masin 2005) that defines behavior at large strains is defined by five soil model parameters shown in Table 2.3 and Figure 2.7.

Table 2.3 Reference model parameters for the HC model

Model parameter	Description
λ^*	Slope of virgin compression line in $\ln p' - \ln(1+e)$ plane
κ^*	Slope of unload/reload line in $\ln p' - \ln(1+e)$ plane
N	Value of $\ln(1+e)$ on virgin compression line at $p'=1$
ϕ'_c	Critical state friction angle
ν_{pp}	Controls ratio of bulk and shear stiffness

Parameters λ^* and κ^* define the gradient of the isotropic normal compression line and the isotropic unloading line, respectively, in the $\ln(1+e) - \ln(p')$ plot of Figure 2.7. Parameter N defines the natural logarithm of the specific volume $(1+e)$ on the isotropic normal compression line at $p'=1$ kPa.

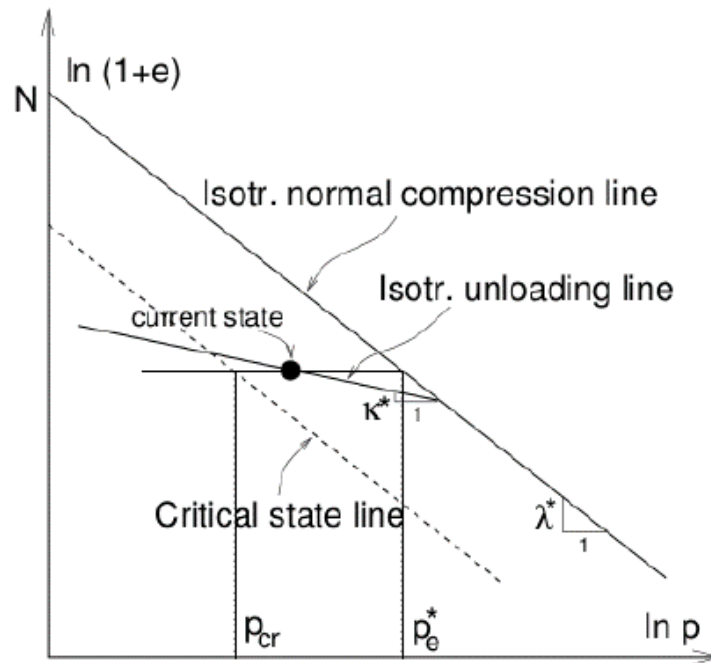


Figure 2.7 Definition of model parameters λ^* , κ^* and N (taken from Masin 2005)

Parameter v_{pp} is a fitting parameter which is typically obtained from parametric studies based on stress-strain curves of undrained triaxial compression and extension tests. It controls the shear stiffness and is related to the bulk-to-shear stiffness ratio, r , by:

$$v_{pp} = \frac{3r(\lambda^* + \kappa^*) - 4\kappa^*}{6r(\lambda^* + \kappa^*) + 4\kappa^*} \quad (2.13)$$

Parameter r was originally used in the reference HC model proposed by Masin (2005). Improvements in the original model were made by introducing parameter v_{pp} (Masin 2013). This improved reference model is the version employed in PLAXIS (Gudehus et al. 2008).

By incorporating the intergranular strain concept (Niemunis and Herle 1997), Masin (2005) extended the capabilities of the reference model to capture the small strain non-linear soil stiffness. This HC model has evolved over time (Masin 2014) and later implemented in PLAXIS with model parameters shown in Table 2.4.

Table 2.4 Small strain stiffness parameters for the HC model

Model parameter	Description
$\alpha_G, \alpha_E, \alpha_v$	Anisotropy ratios for very small stiffness, Young's modulus and Poisson's ratio $\alpha_G = G_h / G_v \quad (2.14)$
A_g, n_g	Very small strain shear stiffness $G_{vh} = p_r A_g \left(\frac{p'}{p_r} \right)^{n_g} \quad (2.15)$ <p>where p_r is a reference pressure parameter of 1 kPa</p>
m_{rat}	Parameters controlling very small strain behavior upon strain path reversals $m_{rat} = m_R / m_T \quad (2.16)$
R	Size of elastic range in strain space
β_r, χ	Parameters controlling the rate of degradation of stiffness with strain

Note that for applications of the HC model prior to the development of the advanced HC model (Masin 2013), model parameters m_R and m_T are used instead of $\alpha_G, \alpha_E, \alpha_v, A_g, n_g$ and m_{rat} (e.g., Sarabia 2012). The original and new model parameters are directly correlated to each other with the equations in Table 2.4. Parameters R, β_r and χ are used in both the original and

advanced HC models. HC model parameters are described in detail by Masin (2005, 2013, 2014), Gudehus et al. (2008).

Figure 2.8 shows the effects of the intergranular strain parameters R , β_r and χ on the shear stress-shear strain relationship. Parameters β_r and χ control the degradation of stiffness from maximum shear modulus, G_{vh} or G_{vh} , to the reference model stiffness. Parameter R controls the magnitude of the intergranular strain region. Masin (2011) performed parametric studies to determine the influence of those parameters in the stiffness degradation of soils and provided ranges of variation for several soils (Table 2.5).

Table 2.5 Small strain parameters for various clays

	R_{max}	β	χ
London clay (reconstituted)	1.0×10^{-04}	0.20	6.0
London clay (natural)	5.0×10^{-05}	0.10	1.0
Brno clay	1.0×10^{-04}	0.20	0.8
Koper silty clay	2.0×10^{-05}	0.09	0.7

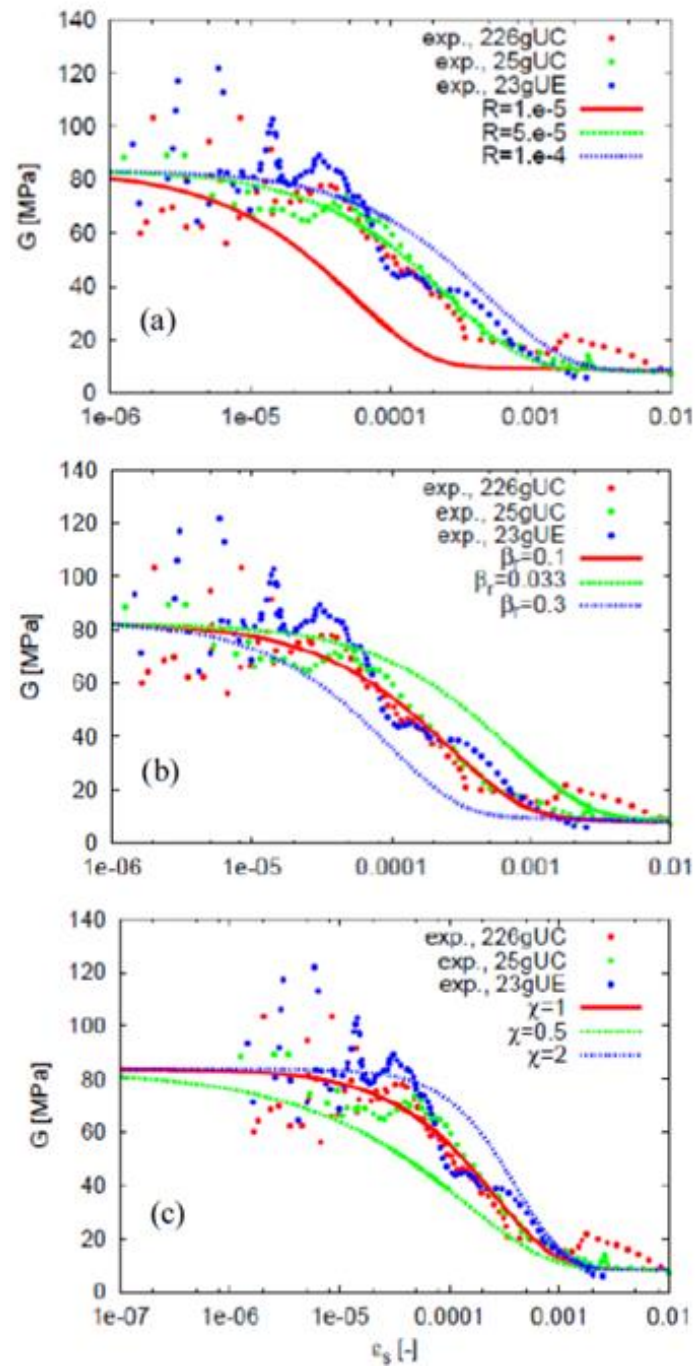


Figure 2.8 Calibration of constitutive parameters for the HC model with intergranular strains:

- (a) size of elastic range R ,
- (b) degradation rate parameter β
- and (c) degradation rate parameter χ (taken from Masin 2011)

2.6 Geotechnical Inverse Analysis: Literature Review

In geotechnical engineering, inverse analysis techniques have been applied to field problems such as tunnels, embankments and excavations to assess the structure response (e.g., Honjo et al. 1994, Ou and Tang 1994, Gioda and Locatelli 1999, Finno and Calvello 2005, Rechea 2006, Mu et al. 2016). It also has been applied to laboratory tests to calibrate the constitutive models (e.g., Cavello 2002, Sarabia 2012). Examples of inverse analyses carried out for laboratory tests and field problems for Chicago clays are presented in the following sections.

2.6.1 HS Model Optimization based on Field Observations at the Chicago-State Excavation

Inverse analysis was used to calibrate model parameters for four Chicago clay stratum, Upper Blodgett, Lower Blodgett, Deerfield and Park Ridge present at the Chicago Avenue and State Street CTA subway station (Chicago-State) (Calvello 2002). The soil specimens used for the laboratory tests were thin-walled tube samples of clay obtained during site exploration for the Chicago-State project. Stress-strain and excess pore water pressure data found in isotropically consolidated drained and undrained triaxial compression tests were used as the observations in the inverse analysis. The HS model parameters were calibrated using the parameter optimization algorithm UCODE and the finite element program PLAXIS.

The initial values of the HS input parameters were computed according to conventional calibration procedures of Table 2.6. The values of the soil parameter values obtained by Roboski (2001) are shown in Table 2.7.

Table 2.6 Conventional calibration procedures for HS model parameters

Parameter	Description	Calibration procedures
ϕ	Friction angle	Slope of failure line in σ_n - τ stress space
c	Cohesion	y-axis intercept in σ_n - τ stress space
ψ	Dilatancy angle	Function of ϕ_{peak} and $\phi_{failure}$
E_{50}^{ref}	Secant stiffness in standard drained triaxial test	y-axis intercept in $\log(\sigma_3/p^{ref})$ - $\log(E_{50})$ space
E_{oed}^{ref}	Tangent stiffness for primary oedometer loading	y-axis intercept in $\log(\sigma_v/p^{ref})$ - $\log(E_{50})$ space
E_{ur}^{ref}	Unloading-reloading stiffness	default = $3E_{50}^{ref}$
m	Power for stress level dependency of stiffness	Slope of trendline in $\log(\sigma_3/p^{ref})$ - $\log(E_{50})$ space
ν_{ur}	Poisson's ratio	default = 0.2
R_f	Failure ration q_f/q_a	default = 0.9
k_0	k_0 value for normally consolidated soil conditions	default = $1 - \sin\phi$

Table 2.7 HS model parameters based on conventional calibration procedures

Parameter	Upper Blodgett	Lower Blodgett	Deerfield	Park Ridge
ϕ ($^\circ$)	24.1	27.0	28.9	31.4
c (kPa)	0.05	0.05	0.05	0.05
ψ ($^\circ$)	0	0	0	0
E_{50}^{ref}	2,350	3,700	4,000	11,700
m	1.00	0.91	1.00	0.94

Using the estimates of the soil parameters in Table 2.7, sensitivity and correlation analyses were carried out to select the model parameters to be optimized. Details of the parameter selection process are described in Calvello and Finno (2004). They concluded that parameters ϕ , E_{50}^{ref} and m should be optimized for all layers. Note that p^{ref} is 100 kPa for the reference stiffness values given in this thesis. Table 2.8 shows the best-fit values of the HS parameters for the four clay layers based on optimization procedures using laboratory data for the observations. Figure 2.9

shows the fit improvement using optimized model parameters for the Deerfield layer. Other clay layers also showed similar improvement through the optimization.

Table 2.8 HS model parameters based on optimization of laboratory data

Parameter	Upper Blodgett	Lower Blodgett	Deerfield	Park Ridge
ϕ (°)	23.4	23.5	25.6	32.8
c (kPa)	0.05	0.05	0.05	0.05
ψ (°)	0	0	0	0
E_{50}^{ref} (kPa)	4,700	7,250	6,000	8,580
m	0.74	0.68	0.85	0.84

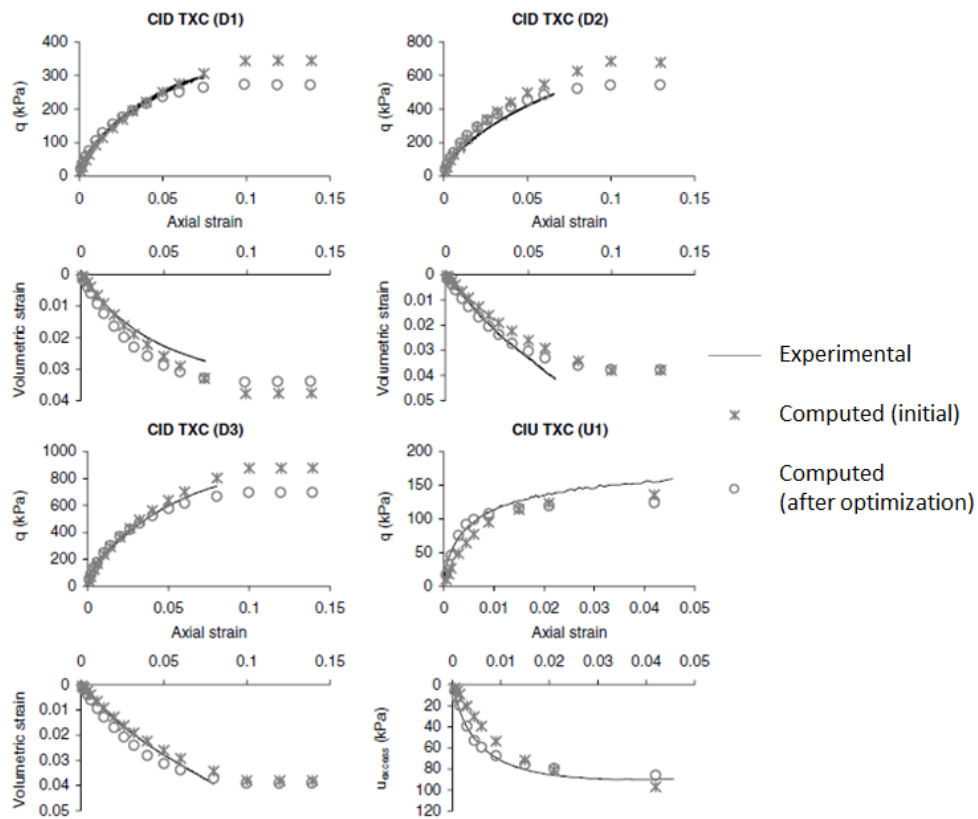


Figure 2.9 Visual fit between experimental and computed results
(taken from Calvello and Finno 2004)

The optimized values given in Table 2.8 were used as the initial parameter values of the inverse analysis carried out with field measurements of the Chicago-State excavation, where 12.2 m of soft to medium stiff clay was excavated to expose the existing Red line subway so it could be renovated. Details of the excavation are presented by Bryson (2002). The support system consisted of a secant pile wall with three levels of support, with pipe struts at the first level and tieback anchors at the lower two levels. Lateral movements of the soil behind the secant pile wall were recorded using five inclinometers located around the site. Inclinometer data from 5 stages of excavation from 2 locations directly opposite one another on the east and west sides of the excavation were used as the observations in the analyses.

PLAXIS 2D was used to compute the response of the soil around the excavation, assuming plane strain conditions. Details about the definition of the finite element model, the calculation phases, and the model parameters used in the simulation can be found in Calvello (2002).

Table 2.9 shows the basic HS model input parameters for the five clay layers that were calibrated by inverse analysis of laboratory tests (Table 2.8). Note that the values of parameter m for the Upper and Lower Blodgett layers, parameter E_{50}^{ref} for Lower Blodgett are slightly different from the values shown in Table 2.8. These values were adjusted to produce values of E_{50}^{ref} and m that consistently increase with depth. The initial values of the parameters for Tinley were selected to minimize movements in that stratum with the equation $(E_{50}^{ref})_{Tinley} = 1.5(E_{50}^{ref})_{Park Ridge}$. The sand and fill layer was modeled with an elastoplastic Mohr-Coulomb model.

Figure 2.10 shows the visual fit between the observations and the results computed before the calibration by inverse analysis. Note that the west inclinometer data do not exist after Stage 3

because it had been destroyed. It can be seen that the computations using initial parameter values based on laboratory test data do not result in a good fit with the field measurements.

Table 2.9 Initial values of HS model parameters for optimization based on field observations

Parameter	Upper Blodgett	Lower Blodgett	Deerfield	Park Ridge	Tinley
ϕ ($^{\circ}$)	23.4	23.4	25.6	32.8	32.8
c (kPa)	0.05	0.05	0.05	0.05	0.05
ψ ($^{\circ}$)	0	0	0	0	0
E_{50}^{ref} (kPa)	4,700	4,700	6,000	8,580	12,870
$E_{\text{oed}}^{\text{ref}}$ (kPa)	3,290	3,290	4,200	6,006	9,009
$E_{\text{ur}}^{\text{ref}}$ (kPa)	14,100	14,100	18,000	25,740	38,610
m	0.8	0.8	0.85	0.85	0.85
k (m/day)	0.00009	0.00009	0.00009	0.00009	0.00009
$k_{0(\text{NC})}$	0.60	0.60	0.57	0.46	0.46

Sensitivity and correlation analyses were carried out using the HS model parameters in Table 2.9 prior to optimization of the field measurements (Calvello and Finno 2004). As for the optimization using laboratory test data, E_{50}^{ref} , m and ϕ showed the highest sensitivities. The parameter ϕ was not considered because the excavation-induced stress conditions were far from failure. Correlation analysis indicated that E_{50}^{ref} and m cannot be simultaneously optimized. The parameter E_{50}^{ref} was chosen over m because E_{50}^{ref} was considered more “representative” of the calibration of all HS model stiffness parameters. Therefore, E_{50}^{ref} of the clay layers were chosen to be optimized.

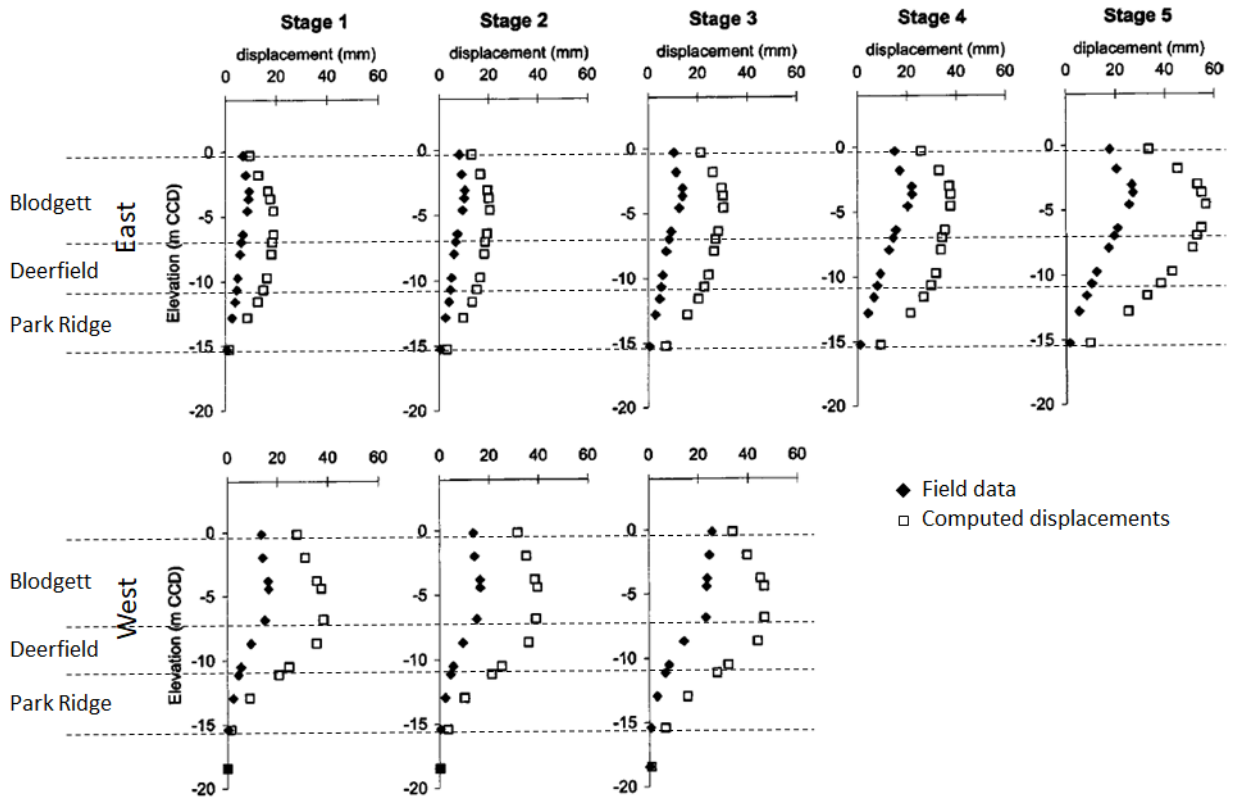


Figure 2.10 Measured and computed lateral displacements using initial parameters
(taken from Calvello 2002)

The Upper Blodgett and Lower Blodgett layers were considered as a single Blodgett layer for simplicity of the optimization process. All observations (i.e., Stages 1, 2, 3, 4 and 5) were used to calibrate the model. The simulation was calibrated starting at Stage 1 and recalibrated at every subsequent construction stage using the inclinometer data available up to that stage. Optimized parameters are shown in Table 2.10.

Table 2.10 Optimized E_{50}^{ref} values for each optimization stage

Optimized stage	Upper Blodgett	Lower Blodgett	Deerfield	Park Ridge	Tinley
Initial	4,700		6,000	8,600	12,900
Stage 1	6,370		17,960	42,310	63,465
Stage 2	6,820		17,530	44,000	66,000
Stage 3	7,550		15,670	53,610	80,415
Stage 4	7,550		15,670	53,610	80,415
Stage 5	7,550		15,670	53,610	80,415

Results of Table 2.10 indicate that the initial estimates of the stiffness parameters based on the laboratory test results are significantly lower than the parameters optimized with the field observations. This trend is expected because the initial values were based on results of triaxial compression tests for specimens taken from thin-wall tubes.

Figures 2.11 and 2.12 show the visual fit between the observations and the results computed after the calibration by inverse analysis at Stage 1 and Stage 3, respectively. Boxes indicate the stages that were used in the calibration. Plots outside the box are predictions made with the optimized parameters. Optimization based on Stage 1 observations (Figure 2.11) show that the optimized parameters produce a reasonable prediction of later stages. Optimization using Stage 3 observations (Figure 2.12) show very close fits between the computations and measurements. Optimized parameters show no changes from optimization made at Stage 3 through Stage 5.

Although the predictions using optimized parameters of Stage 3 show better fits with the measurements compared to using the optimized parameters of Stage 1, the Stage 1 optimization still shows results with reasonable predictions of later stages. This result illustrates the utility of

the inverse analysis approach where optimizations of soil parameters of earlier stages of a project provide a basis for a new simulation in which reasonable predictions of later stages may be made.

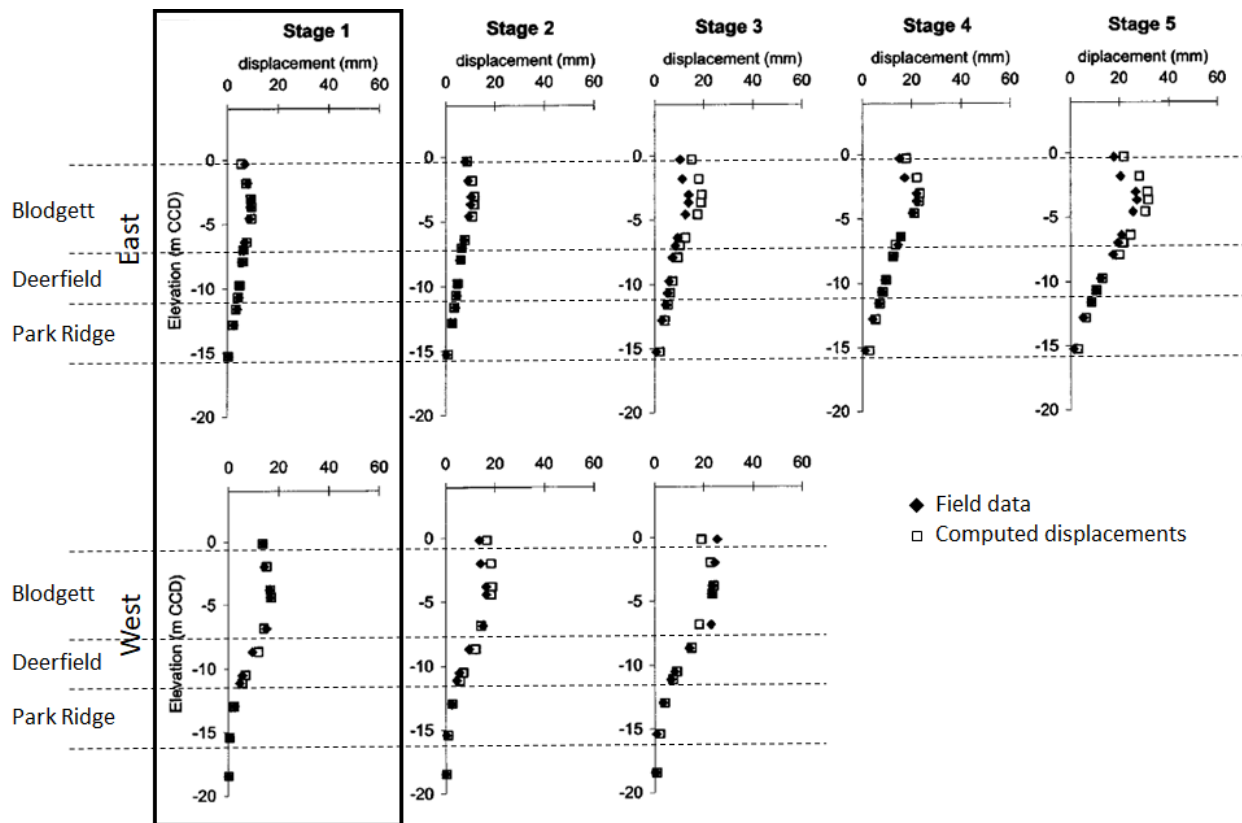


Figure 2.11 Measured and computed lateral displacements using parameters optimized based on Stage 1 observations (taken from Calvello 2002)

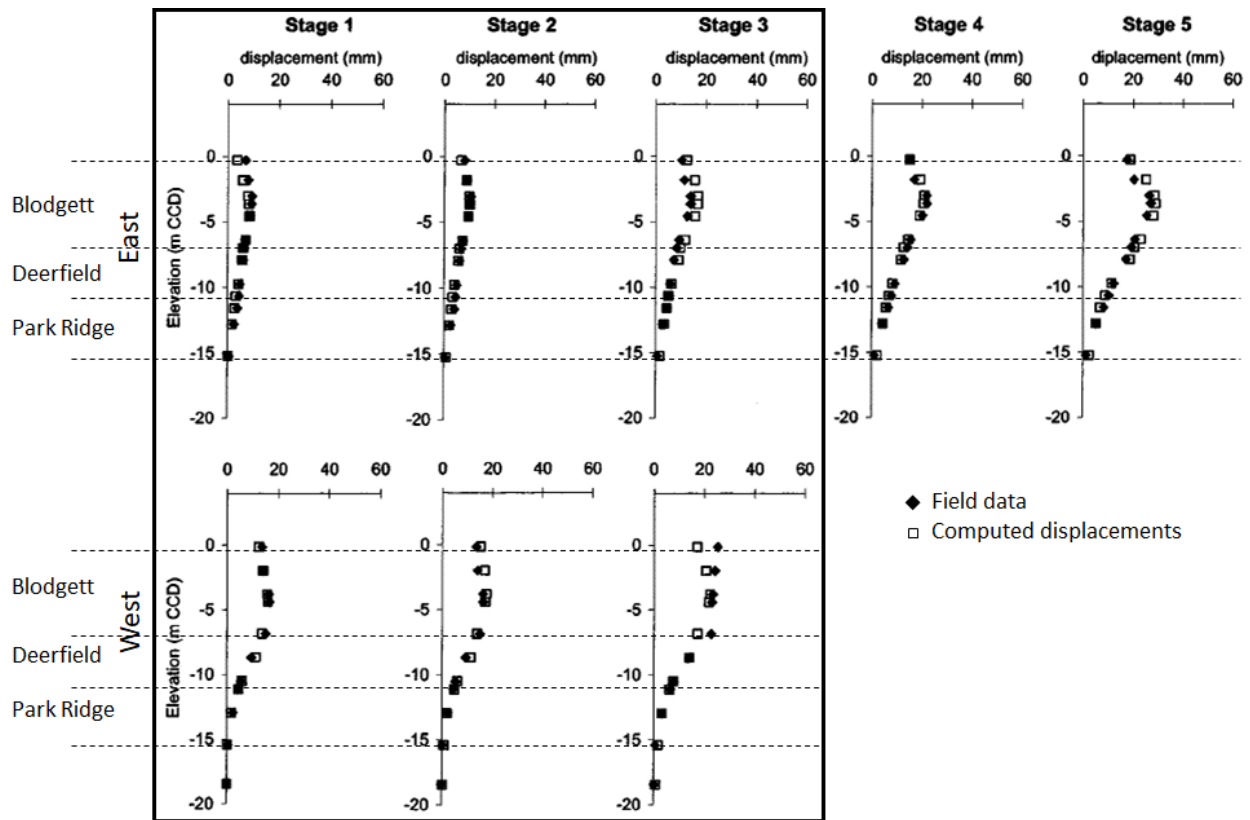


Figure 2.12 Measured and computed lateral displacements using parameters optimized based on Stage 3 observations (taken from Calvello 2002)

2.6.2 HS Model Optimization based on Field Observations at the Lurie Center Excavation

The Robert H. Lurie Medical Research Center (Lurie Center) excavation located in downtown Chicago consisted of a 12.8 m deep cut for two basement levels and a flexible retaining system consisting of PZ-27 sheet pile walls. Three levels of tieback ground anchors were typically installed around the site. Because of the proximity of the utilities and the use of a relatively flexible excavation support system, extensive monitoring points were established around the site. Detailed responses of the inclinometers with major construction stages are described by Roboski (2004),

Finno and Roboski (2005) and Roboski and Finno (2006). Inclimeters LR6 and LR8, which were within 2 m of the west and south walls, respectively, were used in the inverse analysis.

The south and west walls of the Lurie site were modeled with PLAXIS 2D by Rechea (2006). All soil layers were modeled with the HS model. Initial values for the HS model for the Lurie center case are shown in Table 2.11. These parameters were based on results of the Chicago-State excavation optimization, adjusted for differences in the stratigraphy between the two sites.

Table 2.11 Initial estimates of soil parameters for the HS model in the Lurie Center

Soil parameters	Soil strata				
	Fill	Sand	Blodgett/Deerfield	Park Ridge	Tinley
Type	Drained	Drained	Undrained	Undrained	Undrained
E_{50}^{ref} (kPa)	13,500	48,000	5,000	150,000	$1.5(E_{50}^{\text{ref}})_{\text{Park Ridge}}$
$E_{\text{oed}}^{\text{ref}}$ (kPa)	13,500	48,000	3,500	105,000	$0.7(E_{50}^{\text{ref}})_{\text{Tinley}}$
$E_{\text{ur}}^{\text{ref}}$ (kPa)	40,500	144,000	15,000	450,000	$3.0(E_{50}^{\text{ref}})_{\text{Tinley}}$
p^{ref} (kPa)	100	100	100	100	100
m	0.5	0.5	0.8	0.85	0.6
c^{ref} (kPa)	19	0.2	0.2	0.2	0.2
ϕ (°)	30	35	26	32	35
ψ (°)	2	5	0	0	0
v_{ur}	0.2	0.2	0.2	0.2	0.2
OCR	1	1.1	1.4	1.5	2.5

Following the recommendations of Finno and Calvello (2005), the parameters chosen for optimization were the reference values of the primary loading stiffness, E_{50}^{ref} , in the Blodgett/Deerfield and Park Ridge layers. The value of E_{50}^{ref} in the Park Ridge was optimized in

an indirect way by making it equal to 1.5 times E_{50}^{ref} of the stiff clay. Table 2.12 shows the final optimized values of E_{50}^{ref} .

Table 2.12 Optimized E_{50}^{ref} (kPa) values for the medium and stiff clay

	Stage 4		Stage 6	
	LR6	LR8	LR6	LR8
Blodgett/Deerfield (medium clay)	11,300	13,000	5,060	6,000
Park Ridge (stiff clay)	78,900	93,900	129,000	52,200

Figure 2.13 shows the visual fit between measured and calculated displacements, which indicates a very good fit in the clay layers.

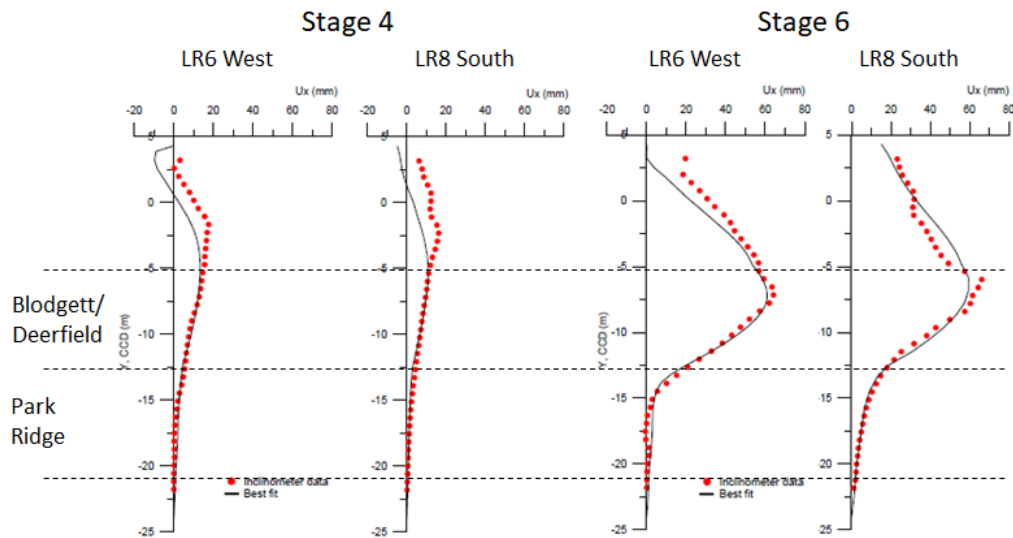


Figure 2.13 Fit between observed and calculated displacements using optimized parameters
(taken from Rechea 2006)

2.6.3 HS Model Optimization based on Field Observations at the Ford Center Excavation

Inverse analysis of the Ford Motor Company Engineering Design Center (Ford Center) was also carried out by Rechea (2006). This is a relatively small excavation of 43 m by 35 m, with a maximum excavation depth of 7.6 m. The performance of this excavation has been described in detail by Blackburn (2005) and Blackburn and Finno (2007). The retaining system consists of a XZ-85 sheet pile wall with two levels of internal bracings. The cross-lot bracing consisted of pipe struts of 0.61 m diameter. The diagonal internal bracings were either pipe struts or wide flange beams. Instrumentation installed at the Ford Center site included conventional methods of monitoring soil and structural deformations, such as slope inclinometers and vibrating-wire strain gages. Inclinometer data from inclinometer INC-1 located near the center of the north wall was used for the inverse analysis because it was most representative for plane strain conditions.

The north side of the excavation was modeled using PLAXIS 2D. Due to the complex excavation sequence, correspondence between PLAXIS phases and performance data was only possible for Stages 9 and 11, when the excavated site geometry was symmetric with respect to the represented cross-section (Rechea 2006). All soil layers were modeled with the HS model. The initial soil parameters are shown in Table 2.13. These parameters were based on results of the Chicago-State excavation optimization, adjusted for differences in the stratigraphy between the two sites.

Following the recommendations of Finno and Calvello (2005), the parameters chosen for optimization are the reference values of the primary loading stiffness, E_{50}^{ref} , in the Blodgett, Deerfield and Park Ridge layers. The value of E_{50}^{ref} in the Park Ridge was optimized in an indirect way by making it equal to 1.5 times E_{50}^{ref} of the Deerfield. The other two reference stiffness values,

E_{oed}^{ref} and E_{ur}^{ref} were indirectly optimized with $E_{oed}^{ref} = 0.7 \cdot E_{50}^{ref}$ and $E_{ur}^{ref} = 3.0 \cdot E_{50}^{ref}$. Initial and optimized values of E_{50}^{ref} are shown in Table 2.14. Note that the initial E_{50}^{ref} values for the Stage 11 optimization were based on the optimization results of Stage 9.

Table 2.13 Initial estimates of soil parameters for the HS model in the Ford Center

Soil parameters	Soil strata					
	Fill/Sand	Clay crust	Blodgett	Deerfield	Park Ridge	Tinley
Type	Drained	Drained	Undrained	Undrained	Undrained	Undrained
E_{50}^{ref} (kPa)	20,000	30,000	10,000	18,000	$1.5(E_{50}^{ref})_{Deerfield}$	300,000
E_{oed}^{ref} (kPa)	20,000	30,000	7,000	12,600	$0.7(E_{50}^{ref})_{Park Ridge}$	210,000
E_{ur}^{ref} (kPa)	60,000	90,000	30,000	54,000	$3.0(E_{50}^{ref})_{Park Ridge}$	900,000
P^{ref} (kPa)	100	100	100	100	100	100
m	0.5	0.5	0.8	0.85	0.85	0.6
c^{ref} (kPa)	0.2	0.2	0.2	0.2	0.2	0.2
ϕ (°)	37	40	24	26	32	35
ψ (°)	5	15	0	0	0	0
v_{ur}	0.2	0.2	0.2	0.2	0.2	0.2
OCR	1.0	2.0	1.4	1.7	2.0	2.5

Table 2.14 Initial and final optimized E_{50}^{ref} (kPa) values for Ford Center

Soil strata	Stage 9		Stage 11	
	Initial	Final	Initial	Final
Blodgett	10,000	16,900	16,900	11,700
Deerfield	18,000	15,200	15,200	17,600
Park Ridge	27,000	22,800	22,800	26,400

Figure 2.14 shows the fit between computations made with optimized parameters and the measurement data from INC-1. Figures 2.14 (a) and 2.14 (b) show the computations made at Stages 9 and 11, respectively, using the optimized parameters from Stage 9. The bold line of Figure 2.14 (c) (Best fit (1)) indicates the computation of Stage 11 using optimized parameters from Stage 11. The dotted line (Best fit (2)) indicates computations of Stage 11 using parameters optimized using the inclinometer data and strut load data. Details of the optimization using strut load data are presented in Rechea (2006).

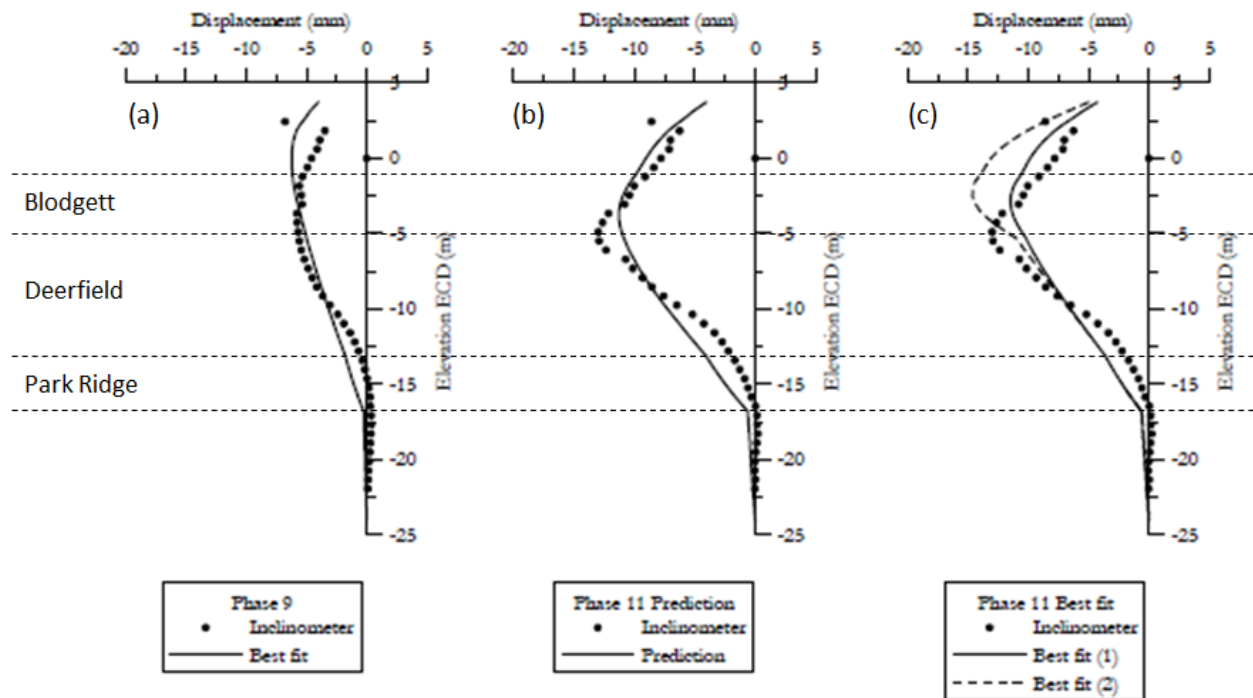


Figure 2.14 Observed and calculated displacements (taken from Rechea 2006)

In Figure 2.14, both the prediction of Stage 11 based on the optimized parameters from Stage 9 and the optimized parameters from Stage 11 show that the measurements and computed lateral deformations are not a good fit at Stage 11. This is due to the small deformation levels used for the observations in the optimization. The maximum measured lateral deformations were 6 and 13 mm for Stages 9 and 11, respectively. The strain level at Stage 11 corresponds to 0.08 %, which is far lower than the other excavation performance studies discussed previously.

2.6.4 Summary of HS Model Optimizations

Optimized E_{50}^{ref} from Chicago-State, Lurie Center and Ford Center were compared with the corresponding shear strains (Rechea 2006). The behavior of the soft clay greatly influences the performance of the support system. The deeper stiffer clays have been less studied and their parameters are usually selected so as to minimize movements rather than to match field or lab test data. Therefore, optimized parameters for the Deerfield layer are compared in Figure 2.15.

Figure 2.15 shows the decrease of E_{50}^{ref} of the Deerfield layer with the increase in shear strain. These results suggest that the HS model is not capable of making accurate predictions based on observations of early stages of excavation where shear strains are relatively small. To make proper predictions of later stages with different shear strain levels, a soil model that represents both small and large strain levels through the use of a single set of model parameters must be employed.

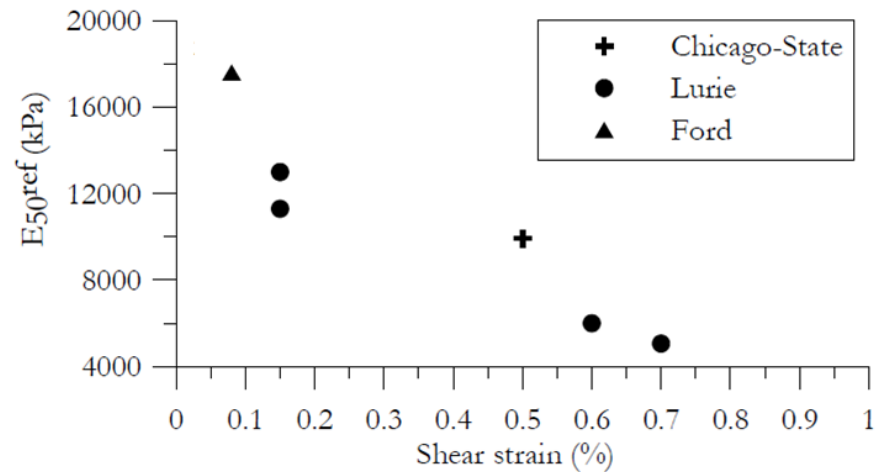


Figure 2.15 E_{50}^{ref} in Deerfield vs. shear strain level for optimization cases
(taken from Rechea 2006)

2.6.5 HS and HSS Model Optimizations based on Field Observations at the Block 37 Excavation

The Block 37 excavation was made through compressible soft to medium stiff Chicago clay to a depth of 15 m using a partial top-down construction technique. A reinforced concrete-slurry wall and four concrete slabs were installed to laterally support the excavation. Twenty-three inclinometers were installed for recording the deformations of the retaining. Details of the construction and measurements are presented by Kern (2011). To consider the middle section of the north wall, the inclinometer corresponding to that position was used as measurements in the inverse analysis.

The observed lateral movements during excavation formed the basis of optimization for both the HS and HSS models (Mu et al. 2015, Mu and Huang 2016). The HS model first was used

to represent all soil layers with parameters shown in Table 2.15. The initial E^{ref} parameters were taken from the optimized parameters from the Chicago-State case (Calvello and Finno 2004, Finno and Calvello 2005). The E_{50}^{ref} parameter was chosen to be optimized for the HS model optimization.

Table 2.15 Initial estimates of soil parameters for the HS model in Block 37

Soil parameters	Soil strata						
	Sand fill	Clay crust	Blodgett	Deerfield	Park Ridge	Tinley	Hardpan
Type	Drained	Undrained	Undrained	Undrained	Undrained	Undrained	Undrained
E_{50}^{ref} (kPa)	45,000	14,000	7,600	15,700	53,600	80,400	160,000
$E_{\text{oed}}^{\text{ref}}$ (kPa)	45,000	9,800	5,300	11,000	37,500	56,300	112,000
$E_{\text{ur}}^{\text{ref}}$ (kPa)	135,000	42,000	22,800	47,100	160,800	241,200	480,000
p^{ref} (kPa)	100	100	100	100	100	100	100
m	0.5	0.85	0.8	0.85	0.85	0.85	0.85
c^{ref} (kPa)	19.16	0.92	0	0	0	0	0
ϕ ($^{\circ}$)	35	32.8	29	30.6	30.6	45	45
ψ ($^{\circ}$)	0	0	0	0	0	0	3
v_{ur}	0.33	0.2	0.2	0.2	0.2	0.1	0.1
OCR	1.5	1.5	1.5	1.4	1.7	1.5	1.5

Another inverse analysis was carried out using the HSS model to represent the Blodgett, Deerfield and Park Ridge layers through two additional model parameters G_0^{ref} and $\gamma_{0.7}$ (Table 2.16). All other soil parameters were kept identical with the HS model parameters in Table 2.15. Initial G_0^{ref} values were obtained from bender element tests of Block 37 soil samples (Kim 2011) and the seismic CPT tests from the Block 37 site. Because G_0^{ref} was well-defined in both the bender

element tests and SCPT tests, the parameter was not chosen to be optimized. E_{50}^{ref} and $\gamma_{0.7}$ were chosen as the parameters to be optimized.

Table 2.16 Initial additional HSS model parameters

	Blodgett	Deerfield	Park Ridge
G_0^{ref} (kPa)	78,000	95,000	83,400
$\gamma_{0.7}$	1.00×10^{-04}	1.00×10^{-04}	1.00×10^{-04}

Figure 2.16 indicates the computed and observed lateral soil deformations measured from the north inclinometer. Because as much as 10 mm of wall deflection was induced by the potholing, the activities were also modeled using dimensions approximated from site photographs. The incremental deformation induced by excavation at Stage 1 from the potholing stage was used as the observation (noted as Stage 1') in the inverse analysis. Optimized parameters for the HS and HSS soil models are shown in Table 2.17.

Optimized E_{50}^{ref} values for the HS model are larger than the HSS model. This is expected when the deformation is relatively small because the full range of stiffness is not considered in the HS model, and a higher value is required to result in a smaller deformation.

Computations of the deformations using the optimized HS and HSS model parameters and the measurements made by the inclinometer are shown in Figure 2.16. The computed deformations based on the optimized parameters agree well with the measured deformations at Stage 1'. The optimized HS and HSS parameters were used to compute the deformations at Stage 4'. The

computations made by optimized HSS parameters are much more consistent with the measurements than computed with the HS model.

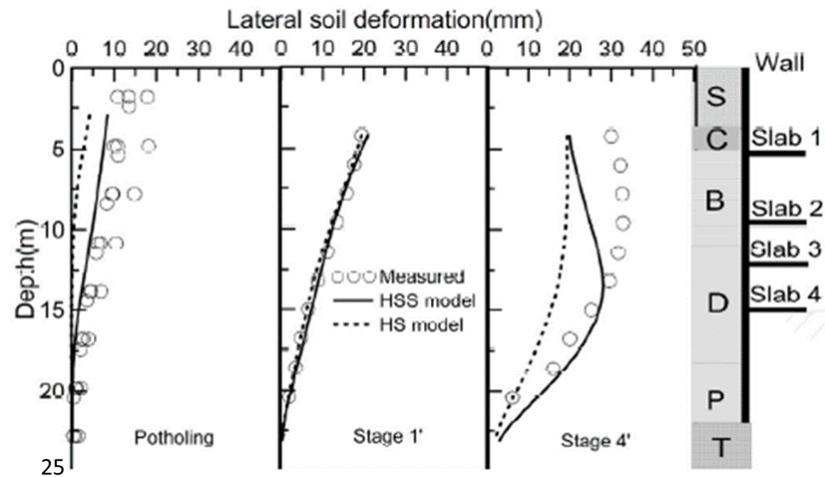


Figure 2.16 Inclinometer measurements used in optimization (taken from Mu et al. 2015)

Table 2.17 Optimized parameters for HS and HSS models

Soil strata	HS model	HSS model	
	E_{50}^{ref} (kPa)	E_{50}^{ref} (kPa)	$\gamma_{0.7}$
Blodgett	10,000	8,200	7.64×10^{-05}
Deerfield	14,000	7,600	6.56×10^{-05}
Park Ridge	32,000	12,700	7.21×10^{-05}

The HS model incorporates a large stiffness to consider the small strain at Stage 1', resulting in a small computed deformation also in the later stages as shown in Figure 2.16. Because the HSS model considers small-strain stiffness, a single set of model parameters can conceptually represent the soil response at a wider range of strains than the HS model. However, the HSS model

still does not properly represent the soil deformation characteristics in the Blodgett and Deerfield layers. This is due to the optimization made at a stage where deformation levels are too small. This shows the importance of using sufficient deformation levels in an optimization process.

2.6.6 HC Model Optimization

The HC model parameters can be divided in two groups: parameters which have a clear physical meaning and can be estimated from lab tests, and parameters whose effects cannot be easily isolated and are best identified using optimizing procedures. Sarabia (2012) estimated the HC model parameters through laboratory tests carried out for various soil samples in Chicago. Parameters that were not easily estimated through conventional means were optimized. Arboleda-Monsalve (2014) used the HC model parameters presented by Sarabia with some site-specific modifications to apply to a finite element simulation of One Museum Park West (OMPW). Deformation levels computed with the HC model parameters were compared with the field measurements.

2.6.6.1 Laboratory Test Data Optimization

Sarabia (2012) estimated the HC model parameters using laboratory test data carried out for various soil samples from Chicago excavation sites (i.e., Block 37, Ford Center and OMPW). Oedometer and k_0 triaxial consolidation tests from various soil samples in the Chicago area were utilized to estimate N and λ^* . The parameter κ^* was estimated by the test data on a soft Chicago clay presented by Butterfield (1979) and one triaxial consolidation test with an unloading cycle on

hard glacial tills performed by Wang (2011). The critical state friction angle was measured from results of drained or undrained triaxial tests. Parameter r cannot be obtained from laboratory test results. Therefore, parameter r was selected for optimization. Note that r can be directly related to v_{pp} by Equation 2.13. Parameter r was considered because the advanced HC model (Masin 2013) using parameter v_{pp} had not yet been introduced.

To estimate the magnitude of the parameter R , a triaxial test sheared to large strain levels followed by a 180° strain path reversal would be needed. In addition, accurate measurements of R in soft clays required the use of triaxial strain measuring devices with higher accuracies than the internal LVDTs. The parameter R is therefore hard to measure through laboratory tests. However, the magnitude of parameter R does not change significantly for a broad range of clays (Masin 2006): 2×10^{-05} to 1×10^{-04} . Consequently, parameter R was not optimized and was set constant with 5×10^{-05} . Parameters m_R and m_T representing the initial shear modulus were estimated using the cross-hole seismic logging tests performed at the OMPW site. Parameters β and χ are related to the intergranular strain, and cannot be obtained from laboratory test data. Therefore, these two parameters were also chosen to be optimized by Sarabia (2012).

The non-optimized model parameters were derived using correlations suggested through regression with numerous existing lab tests of Chicago soils. To optimize the three unknown HC model parameters r , β and χ , 21 drained and undrained triaxial compression and extension tests performed on block and Pitcher samples collected at different project sites around Chicago were used. Detailed descriptions of the performed tests are included in Sarabia (2012). The triaxial tests were modeled using a single four-node quadrilateral finite element (quad4) using the commercial

program Tochnog Professional. Optimized parameters of r , β and χ were 0.424, 0.179 and 1.277, respectively, as shown in Table 2.18.

Table 2.18 HC model parameters optimized with laboratory test data

Parameter	Blodgett	Upper Deerfield	Lower Deerfield	Upper Park Ridge	Lower Park Ridge	Tinley
λ^*	0.082	0.048	0.059	0.050	0.061	0.040
κ^*	0.023	0.014	0.017	0.014	0.017	0.011
N	1.029	0.635	0.759	0.660	0.784	0.535
φ_c	24.2	34.1	30.9	33.4	30.3	36.7
r	0.424	0.424	0.424	0.424	0.424	0.424
m_R	28.27	15.35	19.39	16.15	20.19	12.12
m_T	28.27	15.35	19.39	16.15	20.19	12.12
R	5×10^{-05}					
β	0.179	0.179	0.179	0.179	0.179	0.179
χ	1.28	1.28	1.28	1.28	1.28	1.28

2.6.6.2 Application to OMPW Excavation

Although optimizations using field measurements have not been carried out with the HC model, the model was applied to the finite element simulation of OMPW (Arboleda-Monsalve 2014). Numerical simulation of the entire construction sequence of OMPW was performed using a fully coupled-flow deformation analysis with PLAXIS 2D.

Table 2.19 summarizes the parameters used for each soil stratum. Parameters for the basic HC model were mostly obtained from the correlations suggested by Sarabia (2012), calibrated with site-specific index properties of the OMPW site. Parameters for the Park Ridge and Tinley layers

were obtained from regression analyses with water contents measured at OMPW. The parameter R was adjusted to capture the observed movements at the toe of the perimeter pile walls. Kim and Finno (2012) showed that α_G varies between 1.1 and 1.2 for compressible Chicago clays. α_E and α_v were both computed as 1.1 using correlations proposed by Masin and Rott (2014).

Table 2.19 HC model parameters of Chicago clays used for finite element model of OMPW

Parameter	Blodgett	Deerfield	Upper Park Ridge	Lower Park Ridge	Tinley
λ^*	0.062	0.062	0.055	0.050	0.055
κ^*	0.0113	0.0113	0.014	0.012	0.018
N	0.76	0.76	0.62	0.55	0.75
ϕ_c	25.3	31.7	36.0	37.8	35.8
v_{pp}	0.15	0.15	0.15	0.15	0.15
A_g	4,100	4,100	4,100	4,100	4,100
n_g	0.6	0.6	0.6	0.6	0.6
$\alpha_G, \alpha_E, \alpha_v$	1.1	1.1	1.1	1.1	1.1
m_{rat}	1	1	1	1	1
R	5×10^{-05}	5×10^{-05}	2.4×10^{-05}	2.4×10^{-05}	2.4×10^{-05}
β	0.18	0.18	0.18	0.18	0.18
χ	1.3	1.3	1.3	1.3	1.3

Results of the computed and observed incremental lateral wall deflections and ground settlements during the top-down stages of construction are shown in Figure 2.17. Relatively large movements occurred prior to the top-down construction at OMPW as a result of secant pile wall installation and cofferdam construction in the interior of the excavation for the construction of the central core of the building. These stages were also simulated, so the data shown represent relatively large strains.

Computed lateral deformations of the perimeter pile walls reasonably matched the field measurements throughout the excavation. Maximum lateral wall deflections occurred in the soft to medium stiff clay layers. Also, the computed and measured maximum ground settlements were similar, showing the capabilities of the model to capture the performance of the excavation.

The HC model parameters obtained from lab tests with some adjustments provided a good fit between the computed and measured deformations when applied to the OMPW site. This showed that the HC model provides reasonable soil parameters from lab tests that can properly represent the soil response in field problems. However, optimizations have not been carried out using the field measurement data for the HC model, and should be further studied.

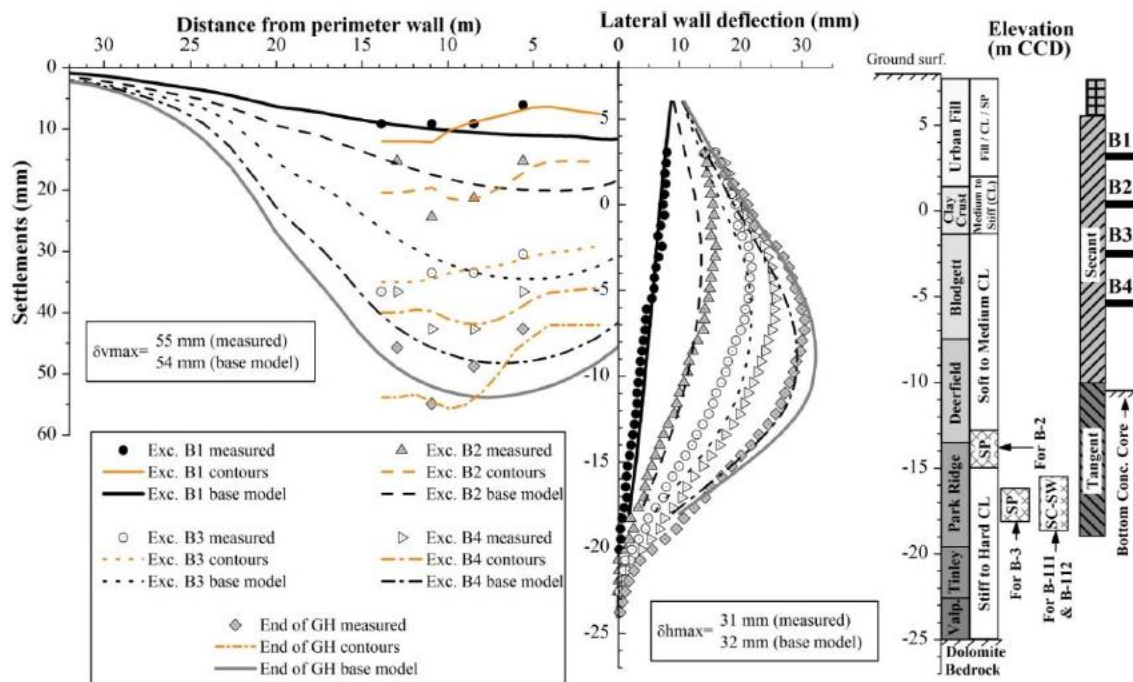


Figure 2.17 Observed and computed results with the PLAXIS model of OMPW

(taken from Arboleda-Monsalve 2014)

2.7 Summary

This chapter describes the adaptive management approach and presents a brief literature review of performance of deep excavations. Inverse analysis techniques applied to Chicago clays were summarized. Statistical measures relevant to selection of parameters for optimization were discussed.

The Hardening Soil Model, the Hardening Soil Model with Small-Strain Stiffness and the Hypoplastic Constitutive Model that are implemented in the inverse analysis of this thesis were summarized, along with the case studies in which the three soil models were used for Chicago soils.

The HS model has been applied to a number of case studies including Chicago-State, Lurie Center, Ford Center and Block 37 excavations. The HS model does not represent the small strain response of soils and this limitation became apparent when results of the various optimizations showed the values of optimized E_{50}^{ref} were proportional to the shear strain levels next to an excavation.

The HSS model consists of a small-strain stiffness overlay to the HS model. This model was applied to the Block 37 case. Although optimized results showed that the HSS model provided a better fit with measurements than the HS model, accurate “predictions” of later stages of the Block 37 case were hindered by the fact that the optimization was made at a stage where the deformation level was small.

Sarabia (2012) presented correlations between HC model parameters and index properties of Chicago soils through regression with numerous existing laboratory tests. Optimizations were

carried out for three HC model parameters that were hard to obtain from laboratory tests. Optimized HC model parameters, with some adjustments, were applied to the finite element model of OMPW, showing reasonable fits between field measurements and computations for the top-down stage of construction. The initial parameters based on the lab data led to good fit, illustrating the utility of the inverse analysis method.

As a result of the limitations of the HS model as shown in the case studies, the need for a soil model considering small strain stiffness is apparent if one wants to use early stages of construction to predict responses at latter stages. However, soil models considering small strain stiffness such as the HSS and HC models have not been thoroughly evaluated for optimizations of excavations in Chicago clays. In this thesis, the utility of inverse analysis using small strain stiffness soil models will be evaluated using the performance data from the SQBRC excavation described in the next chapter.

Chapter 3 Observed Performance of Louis A. Simpson and Kimberly K. Querry Biomedical Research Center

3.1 Introduction

Construction of the 14-story Louis A. Simpson and Kimberly K. Querry Biomedical Research Center (SQBRC) included a 13.1 to 18.0 m deep cut for two basement levels. The excavation serves as the test bed for this research. Van Winkle (2016) presented this case study in his MS thesis and pertinent parts are included in this thesis.

This chapter describes the subsurface conditions and the excavation support system at SQBRC, summarizes construction activities, presents field performance data, and relates observed movements to the construction procedures. After an overview of the responses during construction, movements are presented in terms of those that occurred during sheet pile installation, excavation and support installation, and after final excavated grade was first reached and the walls for the permanent structure were cast against the sheet pile wall.

Maximum lateral wall movements developed during excavation are compared with those expected based on system stiffness and factor of safety against basal heave (Clough et al. 1989). Comparisons are made between the observed performance of the SQBRC and the adjacent excavation for the Robert H. Lurie Medical Research Center (Lurie Center) (Finno and Roboski

2005; Roboski and Finno 2006). The data suggest the accuracy with which one can expect at best to predict lateral wall movements in similar projects.

3.2 Site Description

In November 2015, construction began on the 14-story Louis A. Simpson and Kimberly K. Querry Biomedical Research Center (SQBRC), including a 13.1 to 18.0 m deep cut for two basement levels. The site is located on the old Prentice Pavilion Hospital site, which was demolished prior to any activities related to SQBRC. The hospital included one basement level and was supported on drilled shafts. Existing shafts of Prentice were cut off at excavated grade for the new SQBRC structure. The shafts below that level were left in place and were not used as part of the new foundation system. Due to the proximity of adjacent utilities and structures, optical survey points, shape acceleration arrays (SAAs) and traditional inclinometers were established around the site and monitored.

3.2.1 Subsurface Conditions

The excavation site is located on the Chicago campus of Northwestern University. A steam tunnel which extends down to elev. +0.9 m Chicago City Datum (CCD) borders the north wall of the excavation. The Lurie Center and the Rehabilitation Institute of Chicago (RIC), both caisson-supported structures, abut the west and east walls, respectively, of the SQBRC excavation.

The subsurface conditions were analyzed using borehole data from the SQBRC site and the existing geotechnical investigation data from the Lurie Center. Figure 3.1 summarizes the stratigraphy at the SQBRC and Lurie Center projects, and shows water content and undrained shear strength, S_u , with depth. Values of S_u shown in the figure are based on either in situ field vane (FV) in the softer clays or pocket penetrometer (PP) tests in the harder clays. The subsurface conditions are quite similar at the two sites.

The ground surface is at elev. +4.3 m CCD. A loose to medium dense, surficial granular urban fill is underlain by medium dense, clean beach sand. Beneath the sand layer are strata of progressively stiffer ice-margin clays of increasing shear strength with depth. A 7.3 m thick stratum of soft to medium stiff clays (herein called Blodgett/Deerfield) are encountered below the beach sand. Detailed stress-strain data of specimens collected in this stratum at other projects in the area are summarized in Chung and Finno (1992), Finno and Chung (1992), Cho and Finno (2010), Finno and Cho (2011), Finno and Kim (2012) and Kim and Finno (2012). Both SQBRC and Lurie Center excavations bottomed out in this soft to medium stiff clay stratum. Stiff to very stiff clays (Park Ridge) and a basal till consisting of hard clays and clayey silts, locally known as Hardpan, are encountered atop dolomitic limestone bedrock. Elevations of the Park Ridge and Hardpan layer boundaries are different at the two excavation sites. This however did not result in significant differences in the assessment of performance or FEM computations due to the high stiffness in the lower part of Park Ridge. Groundwater was encountered at elev. 0 m CCD.

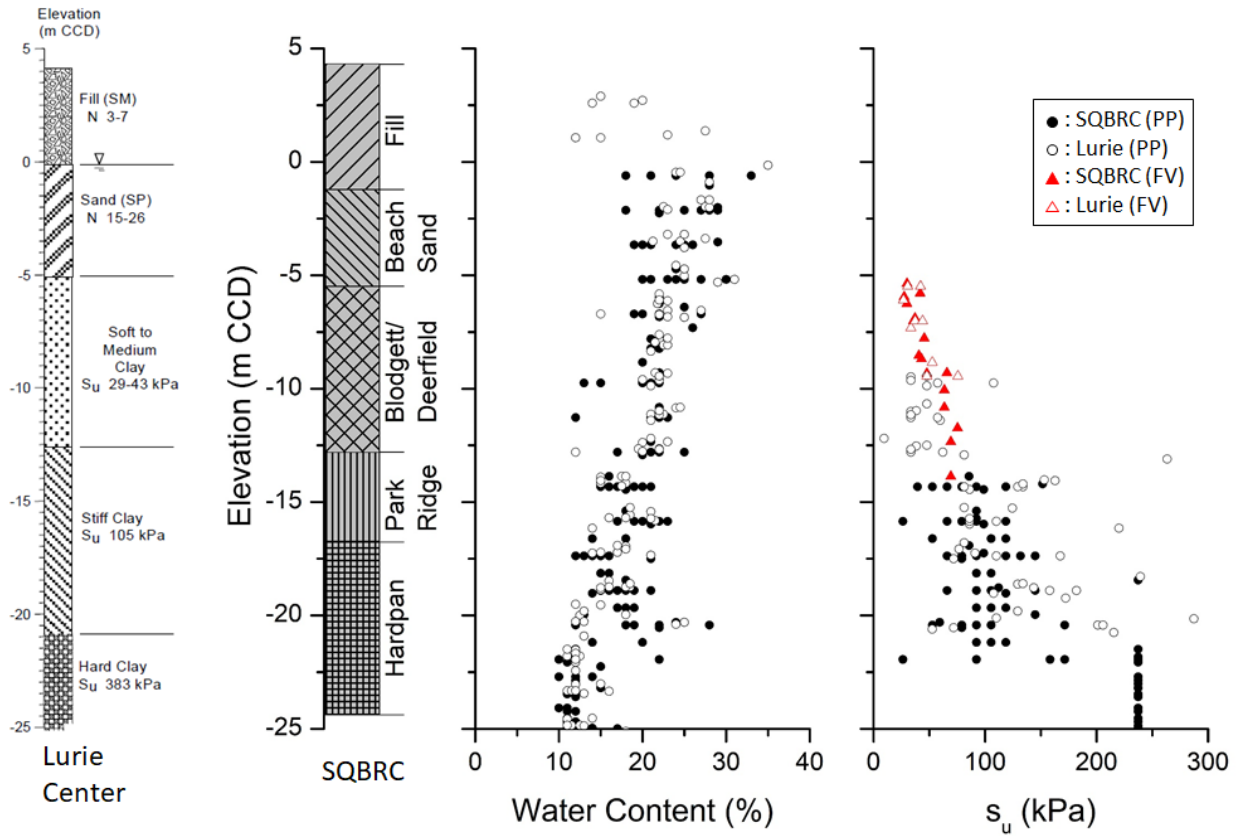


Figure 3.1 Subsurface conditions of SQBRC and Lurie Center

3.2.2 Excavation Support System

Figure 3.2 shows typical sections of the earth retention systems on the north and south walls in relation to the stratigraphy. Figure 3.3 shows the east-west section through the excavation and shows the supports at those walls.

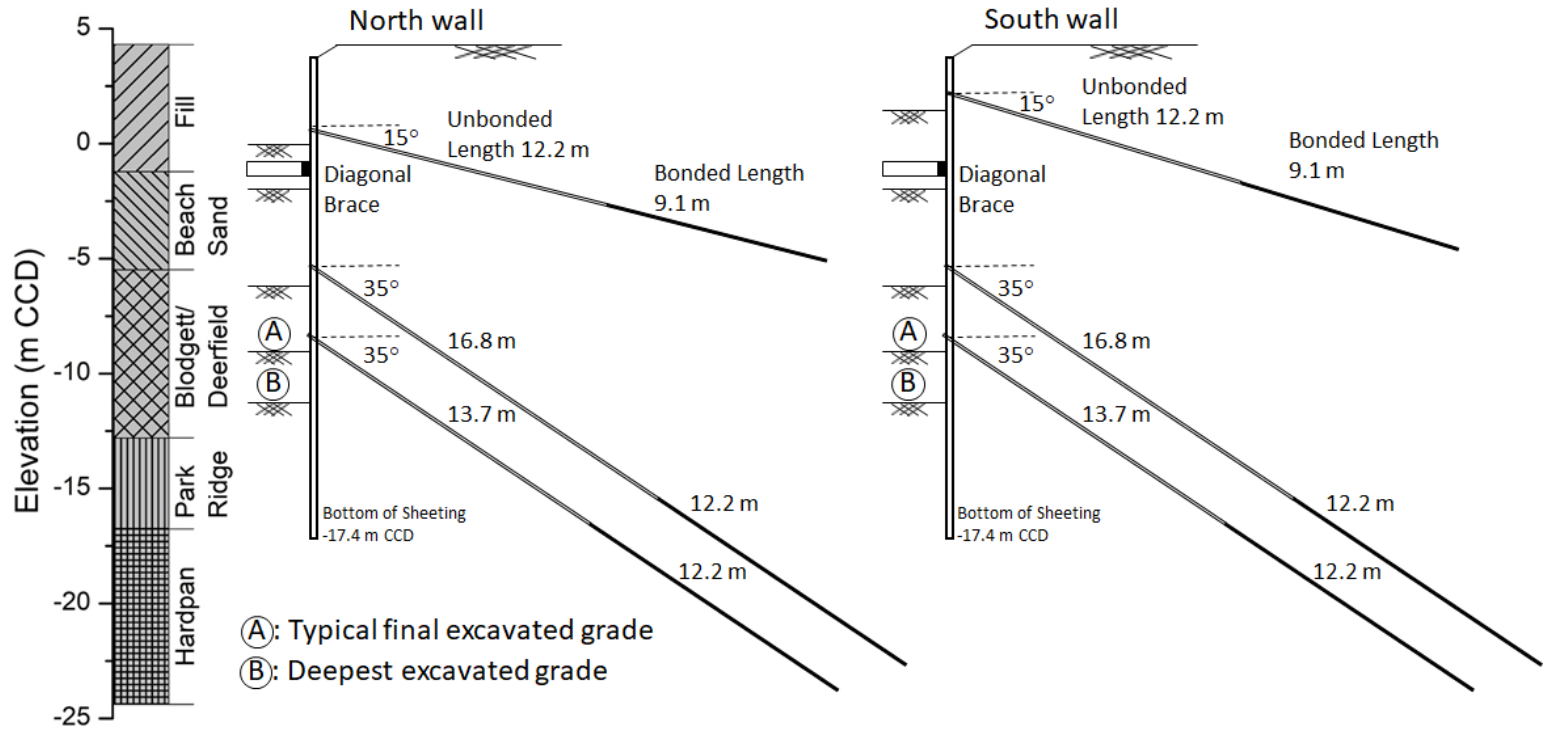


Figure 3.2 Earth retention systems along north and south walls

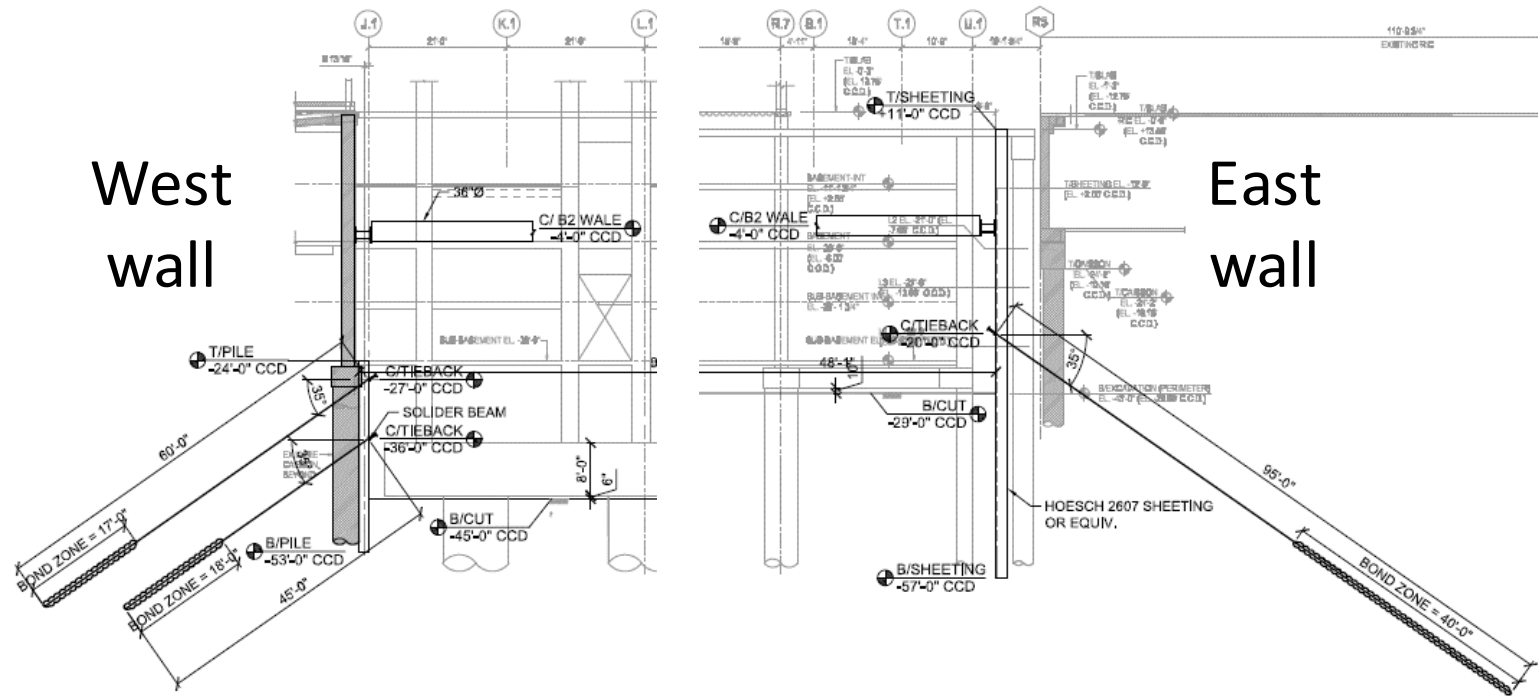


Figure 3.3 West-east cross-sectional view of retention systems

The east and west walls were adjacent to existing drilled shaft-supported structures with basements and as such, the relatively small lateral wall movements did not impact the buildings. Therefore, this chapter will focus on the responses of the north and south walls, although support systems along all four walls are presented for completeness.

The excavation is supported by hot-rolled H3707 sheet piles on the north and south walls, H2607 sheet piles on the east wall, and soldier piles and lagging on the west wall. On the north and south walls, typically two or three levels of tiebacks and one level of diagonal internal braces (elev. -1.2 m CCD) are installed. The first level tieback anchors on the north and south walls were installed at elev. +0.6 and +2.1 m CCD, respectively, with the anchor capacity derived within the beach sand. The second level tiebacks were installed at elev. -6.1 m CCD. At a few locations on the north and south walls, an additional third level of tiebacks was installed (elev. -8.2 m CCD) to allow deeper excavation depths (elev. -11.3 m CCD) for the installation of temporary tower crane foundations. The second and third levels of anchors derived support from the Park Ridge and Hardpan strata. Due to the presence of the basement of RIC to the east, one level of diagonal internal braces (elev. -1.2 m CCD) and only a single level of tiebacks (elev. -6.1 m CCD) are installed on the east wall. On the west wall, due to the existence of the Lurie Center basement, one level of diagonal internal braces (elev. -1.2 m CCD) along with a level of tiebacks (elev. -8.2 m CCD) are installed. At some locations on the west wall, an additional level of tiebacks is installed (elev. -11.0 m CCD) to support deeper excavations (elev. -13.7 m CCD) in the center west part of site.

The first level tieback anchors on the north (elev. +0.6 m CCD) and south (elev. +2.1 m CCD) walls were 15 mm diameter strands made of 1,860 MPa steel in four-strand configurations,

installed every 1.4 m in 150 mm diameter holes. The design loads of the first level anchors were 537 to 551 kN. Unless noted otherwise, lock-off loads were about 60% of the design load. In the case of the first level anchors, the actual lock-off loads were 320 kN. The second level tiebacks (elev. -6.1 m CCD) were 15 mm diameter strands in six-strand configurations, installed with horizontal spacings of 1.4 m on the north and south walls and 2.8 m on the east wall in 200 mm holes. The design loads of the second level anchors were 804 kN; the lock-off loads were 490 kN for all three walls. The third level tiebacks (elev. -8.2 m CCD) were 15 mm diameter strands in six-strand configurations, spaced every 1.4 m on the north and south walls in 200 mm holes. On the west wall, the anchors consisted of 15 mm diameter strands in two-strand configurations, spaced at 3.7 m in 150 mm holes. Tieback level 3 had design loads of 814 kN on the north and south walls, and 210 kN on the west wall. The lock-off loads on the north and south walls were approximately 420 kN. A fourth level of tiebacks (elev. -11.0 m CCD) was installed only on the west wall with 15 mm diameter strands in two-strand configurations, spaced every 3.7 m horizontally in 150 mm holes. The design loads were 248 kN. Loads from the tiebacks are distributed by two C15x33.9 steel sections connected by welded spacer plates acting as wales, allowing the tiebacks to pass between them.

Diagonal braces consisted of 915 mm diameter, 16 mm thick pipe struts and were used to avoid starting the tiebacks under the water table in the beach sand. In addition to helping support the excavation, these braces were designed to provide lateral resistance for the adjacent structures. The pipes were preloaded using hydraulic jacks to 1/3 of the design load before installing shim plates and welding them in place on all four walls. Loads from the internal bracings were transferred to the sheeting by two W27x281 steel sections. The connections between the wales and

the sheet piles were made with welded plates at each sheet. The longest internal braces were supported by a system of piles and connected HP-sections to restrict the unbraced length to prevent buckling.

Micropiles and a slab foundation were installed adjacent to the excavation on the south side of the site at existing grade to support heavy construction equipment. These micropiles consisted of 140 mm diameter steel pipes extending to elev. -25.9 m CCD, with a bonded zone starting at elev. -16.8 m CCD. Grout was injected with pressures between 970 and 2,400 kPa.

The SQBRC structure is supported by belled drilled shaft foundations. The bottom depth for these foundations ranged between elev. -24.4 and -25.9 m CCD. Shaft sizes ranged from 0.7 to 3.1 m in diameter with bell diameters between 1.8 and 6.7 m.

3.2.3 Instrumentation

Instrumentation locations are shown in Figure 3.4. To measure the lateral deformation of the sheet pile wall, Shape Acceleration Arrays (SAAs) were installed at six locations around the site – noted as SAA-1 through SAA-6. A SAA is very similar to a conventional inclinometer, but it remains in place throughout the excavation and can be programmed to take readings at specified time intervals. It consists of an array of rigid segments 0.5 m long with diameters of 25 mm. Each segment has three temperature-calibrated Micro Electro Mechanical System (MEMS) accelerometers and the segments are connected by flexible joints that can move in any direction but cannot twist. These SAAs were installed directly behind the sheet pile walls and initialized after the sheet piles were installed, but before excavation began.

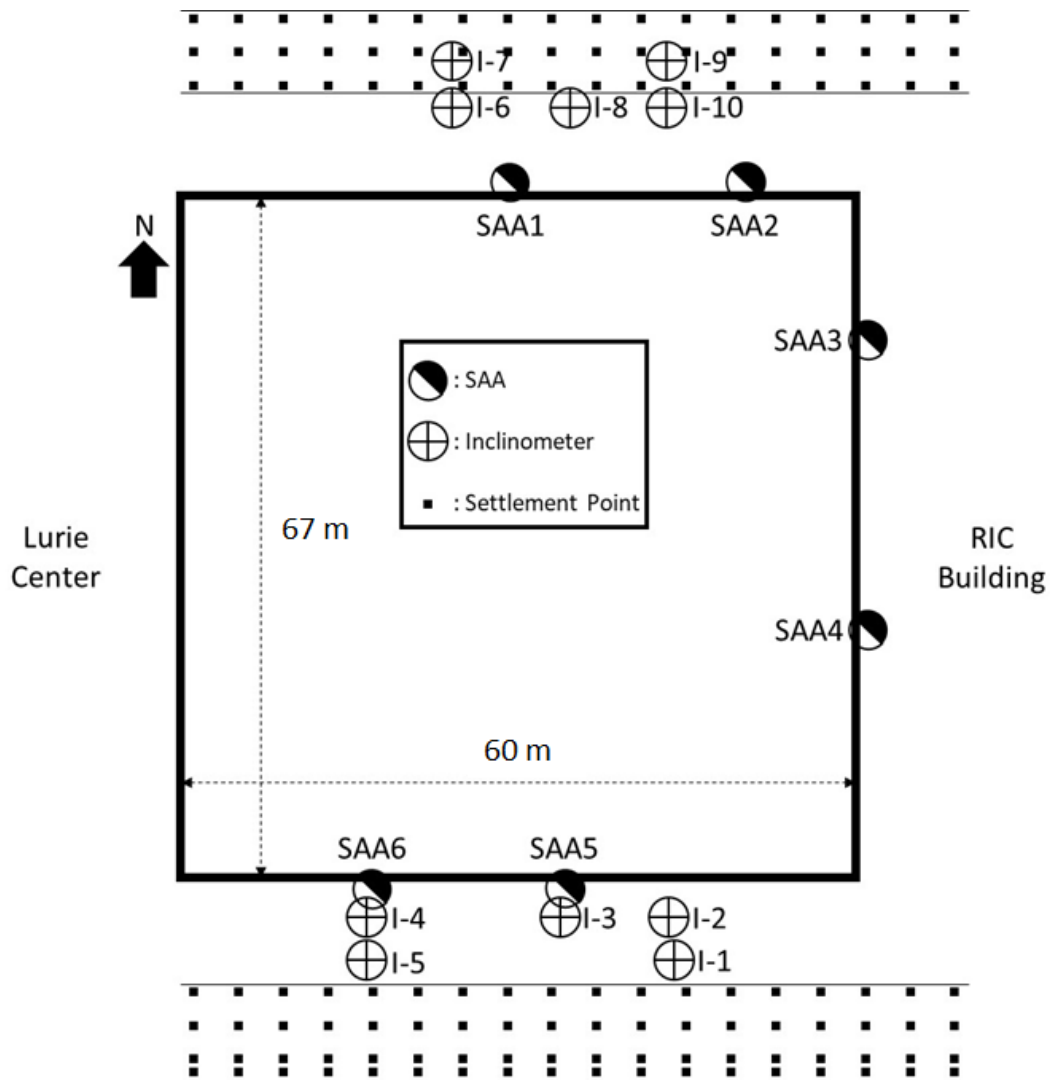


Figure 3.4 Instrumentation plan for SQBRC

In addition to the SAAs, a total of 10 conventional inclinometers were installed at various distances behind the north and south walls. Five inclinometers noted as I-6 through I-10 were installed 4.3 and 8.2 m from the north wall; five inclinometers noted as I-1 through I-5 were installed 0.3 and 4.0 m from the south wall. These inclinometers were initialized prior to any

construction activities on site. Use of these inclinometer data is restricted due to inconsistent trends of movement as will be discussed later in Section 3.4.

Conventional optical surveys were made using 126 surface settlement points (P.K. nails) established in the streets to the north and south of the site. Three rows of measurements were made behind the north wall at distances of 6.1, 9.0 and 11.9 m from the wall. Measurements were made in four rows behind the south wall at distances of 6.1, 9.0, 11.9, and 13.4 m.

Two robotic total stations were installed on adjacent buildings to measure deformations of the surrounding structures and the basement wall shared with the Lurie Center. Negligible movements of these structures were recorded, and therefore will not be presented in this thesis.

All remotely sensed data were displayed in real-time on a password-protected project web site so that progress of the work and associated ground movements were available to all parties in real-time. The purpose of the monitoring data was to verify that the measured horizontal movements did not exceed 50 mm. These restrictions were established by the City of Chicago to protect adjacent utilities from excessive deformations.

3.3 Construction Sequence

Drilled shafts to support the SQBRC were installed prior to any excavation and earth retention activities from December 2015 through February 2016. Activities at the north and south walls are organized into 12 stages (Stage 0 to Stage 11) as indicated Table 3.1. Sheet pile installation started on February 5, 2016, noted as construction day 0 in the table. Because the SAAs were not initialized until the sheet pile walls were installed and no lateral wall deformations were measured until then, the sheet pile installation activity was named Stage 0. Sheet pile sections were installed by an ABI MRZV 30W vibratory hammer. Due to the proximity of existing drilled shaft foundations at the east corner of the north wall and other locations, an impact hammer was utilized to complete placement of the sheeting around these obstructions.

As noted in Table 3.1, distinct excavation stages are defined as the period when grade was lowered below each support level and to final grade. Cycles of soil removal and support installation progressed until the excavation reached its final grade, for most of the site at elev. -8.8 m CCD (Stage 7). Excavated grade was maintained 0.6 to 0.9 m below each level of support as the supports were installed. As the diagonal braces were placed during Stage 4, 16 micropiles and a reinforced concrete slab were installed adjacent to the south wall to support heavy construction equipment. Figure 3.5 shows photographs of the south wall during Stage 4 and Stage 5 to illustrate the ephemeral nature of the access ramp. Its presence impacted the development of the lateral wall movements at the south wall, as discussed later.

Table 3.1 Construction sequence

Stage	Construction date (day)	Activity
0	2/5 - 2/26 (0 - 21)	Sheet pile wall installation
1	3/3 - 3/11 (27 - 35)	Excavation to elev. 0 m CCD (north); +1.5 m CCD (south)
2	3/3 - 3/28 (27 - 52)	First level tieback at elev. +0.6 m CCD (north); +2.1 m CCD (south) (Ramp construction: day 46)
3	3/25 - 4/13 (49 - 68)	Excavation to elev. -2.1 m CCD (Ramp removal, replacement: days 63 - 68)
4	4/16 - 5/8 (71 - 93)	Wale, diagonal strut installation (elev. -1.2 m CCD) (Micropile installation: days 67 - 77; SAA-5 re-initialization: day 78; Ramp removal, replacement: days 81 - 89)
5	5/9 - 6/17 (94 - 133)	Excavation to elev. -6.7 m CCD (Ramp removal: days 125 - 133)
6	5/21 - 7/9 (106 - 155)	Second level tieback at elev. -6.1 m CCD
7	6/23 - 7/19 (139 - 165)	Excavation to elev. -8.8 m CCD
8	6/25 - 7/29 (141 - 175)	Third level tieback at elev. -8.2 m CCD (at some locations)
9	7/14 - 8/6 (160 - 183)	Excavation to elev. -11.3 m CCD (at some locations)
10	8/6 - 12/11 (183 - 310)	Pile cap and grade beam installation
11	12/11 - 12/21 (310 - 320)	Diagonal bracing removed and temporary wall connected to permanent walls



Figure 3.5 Access ramp along south wall

Activities noted as Stages 8 and 9 occurred at locations along the north and south walls where the final excavation grades were below elev. -8.8 m CCD (Figure 3.6). Lower grades of elev. -11.3 m CCD were needed to construct foundations for the tower cranes at the center part of the north wall and the west corner area of the south wall. For these areas, an additional level of tiebacks was installed (third level tiebacks). Deeper excavations were made to elev. -11.3 m and -

13.7 m CCD in the center part of the site, but are not included in Table 3.1 because they are not representative of conditions at the north or south walls.

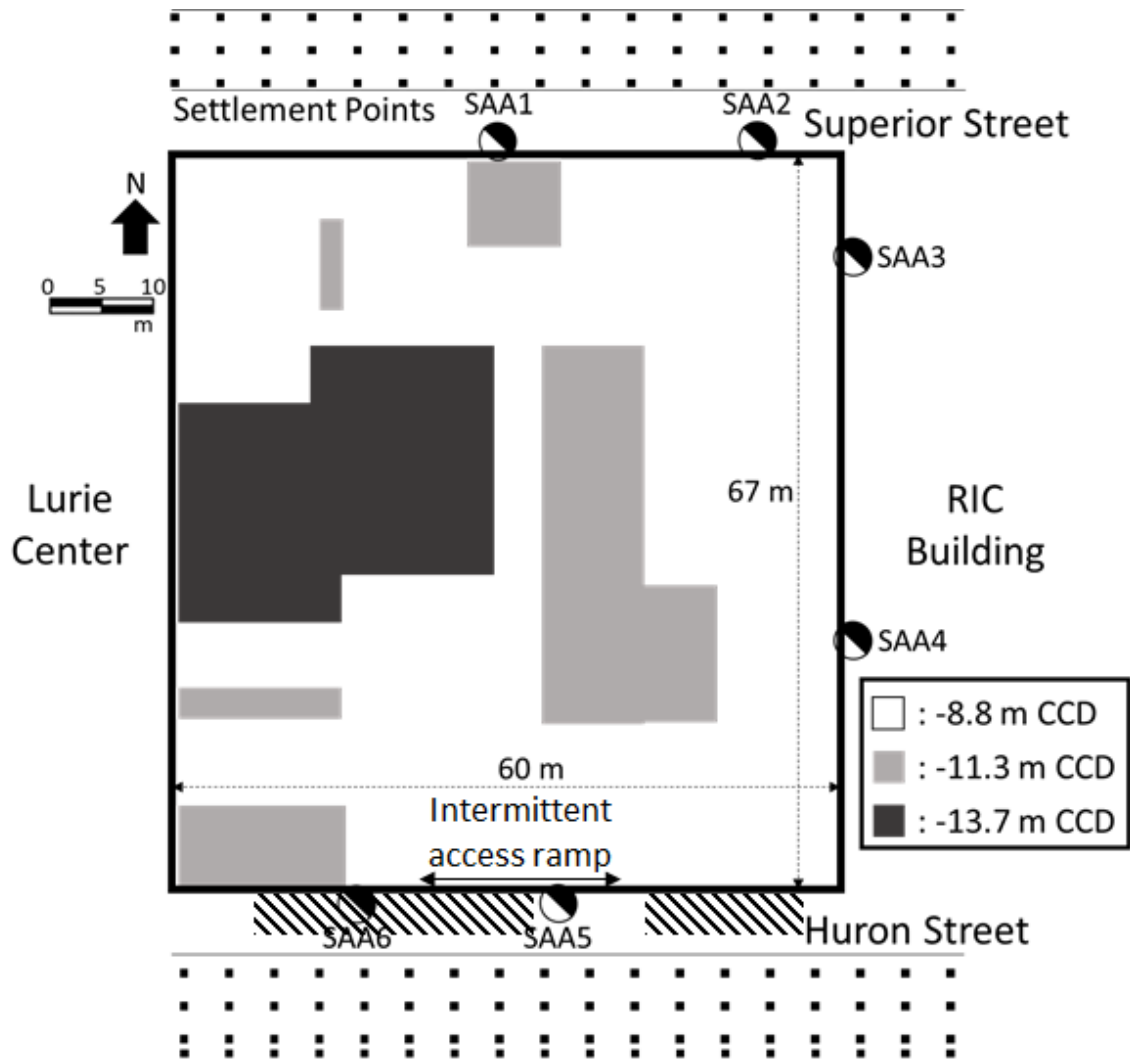


Figure 3.6 Excavated grade and micropile installation positions

Demolition of existing drilled shaft foundations for Prentice Pavilion occurred as they were uncovered during the excavation process. These foundations were demolished using backhoe-mounted jackhammers. The site was unwatered through nine wells around the site. The wells were installed within the excavation before the sheet pile walls were driven into place. They extended approximately 1.5 m into the upper clay stratum and were evenly spaced around the site with slight adjustments to avoid proposed or existing structural elements. After the initial unwatering, the wells were activated sporadically to remove water seeping through the interlocks. The unwatering did not remove groundwater from the deeper soil strata, and thus it is unlikely that the unwatering had any significant impact on the overall performance.

3.4 Traditional Inclinometer Data

Measurements were made with traditional inclinometers behind the north and south walls at locations shown in Figure 3.4. Ten inclinometers were installed – noted as I-1 through I-10. Lateral deformations at dates corresponding to Stages 1, 3, 5 and 7, which are the excavated stages before supports are installed, are plotted in Figure 3.7. Note that not all Stages 1, 3, 5 and 7 are plotted for some of the inclinometers due to the lack of data. Note that the measurements for I-10 do not exist because it had been destroyed.

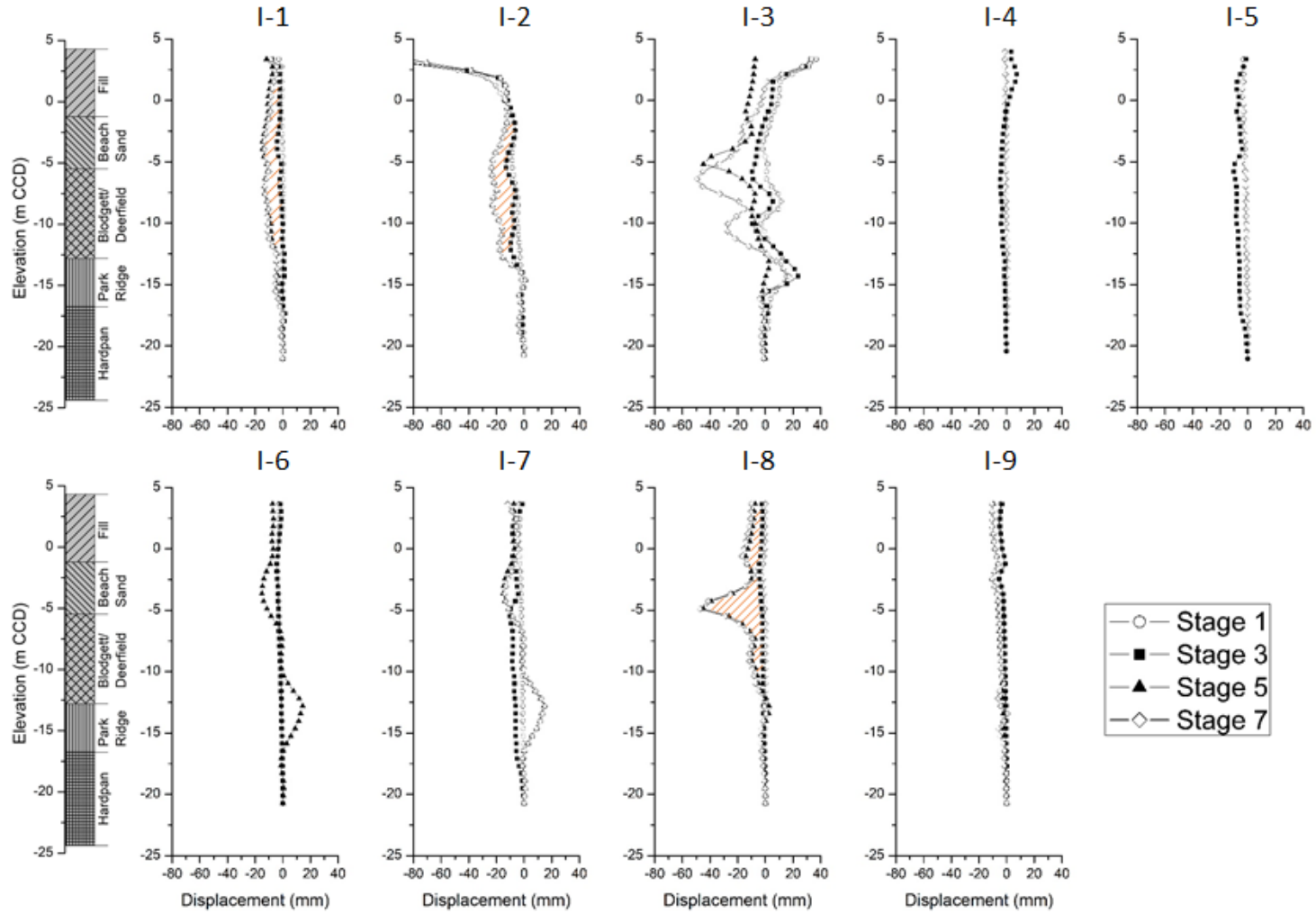


Figure 3.7 Inclinometer measurements

In all inclinometer measurements, an overall movement toward the excavation is observed. For some measurements, erratic changes with multiple “kinks” were observed. These kinks may coincide with the spacing of casing joints for the inclinometers or may have been caused by drilling and grouting of the tiebacks. The overall magnitude of deformation during the excavation is significantly lower than the deformations measured in the SAAs. This is expected to some degree since the inclinometers are installed at distances further from the wall. Noticeable and consistent incremental movements are observed in Inclinometers 1, 2 and 8 (indicated by the light cross-hatching in Figure 3.7) between Stages 3 and 5 due to the excavation reaching into the soft to medium stiff clay during Stage 5, similar to that observed in the SAA data as will later be discussed.

Although the deformation magnitudes at various distances from the wall may be assessed from Figure 3.7, the readings do not properly correspond to the construction activities in a consistent manner as the SAAs do. In addition, various activities at distances from the excavated wall, such as void filling under the northern tunnel slab may have induced deformations that are not related to the excavation process. Installation of tieback anchors passing close to the inclinometers likely also induced deformations that would be quite localized as in the kinks observed in I-8. Because of these reasons, these direct measurements from the inclinometers were not considered as reliable and were disregarded in the performance assessment of the excavation. These data point out the difficulties in obtaining good quality inclinometer data within the zone where tiebacks are installed.

3.5 Observed Performance

Figure 3.8 shows an overview of the lateral wall deformations measured with SAAs throughout construction at the eventual elevation of the maximum lateral deformation, about elev. -6 m CCD, which is close to the second level of tiebacks at the walls. Figures 3.8(a) and 3.8(b) show construction activities and responses at the north wall, respectively. Both SAA-1 and SAA-2 show similar trends. Gradual lateral movements toward the excavation are observed. Small movements occur until the excavation extends into the soft to medium stiff clay layer during Stage 5, at which time the rate of movement temporarily accelerates.

At both SAA locations, installing and stressing the second level of tiebacks at elev. -6.1 m CCD caused the wall at that elevation to temporarily move toward the street (away from the excavation). This was a localized effect and is apparent in this figure because the second level tiebacks were installed within 0.1 m of the elevation of the point being plotted. Smaller incremental movements developed until the end of excavation at Stage 9. Thereafter, the north walls moved gradually toward the excavation until the bracing was removed and the walls for the permanent structure were cast against the sheet pile wall.

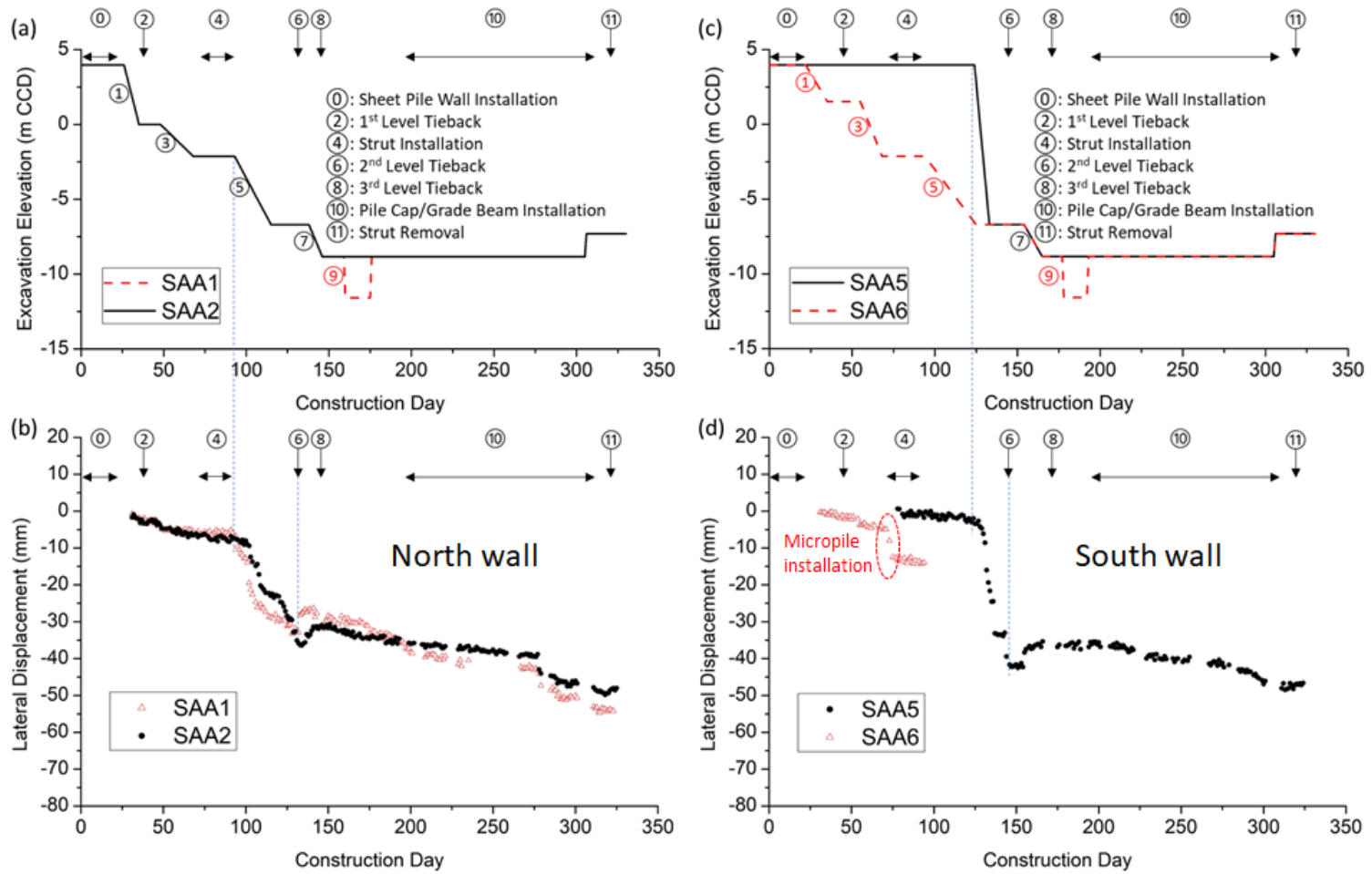


Figure 3.8 Overview of lateral movements

Figure 3.8(c) and 3.8(d) show construction activities and responses along the south wall, respectively. The wall movements were affected by the presence of the access ramp and the installation of the micropiles for the slab adjacent to portions of the south wall. SAA-5 was initialized at a later date than the other SAAs; hence the absence of data before Stage 4. At this time, about 5 mm of wall movement had occurred in the other three SAAs. One can surmise that with the exception of this small amount of movement, the SAA-5 data presented herein essentially represents the wall movements at that location. Large lateral deformations developed at SAA-5 when the ramp was removed during Stage 5 and excavation proceeded below the second level of tiebacks. As the second level of tiebacks were installed and stressed, the SAA-5 data indicated that the wall moved back towards the street. Again, this was a localized effect as was noted for the responses at the north wall. Thereafter, gradual lateral movements toward the excavation were observed as the excavation remained at grade until the flowable fill was placed between the sheet pile and permanent walls for the structure at the south wall.

The SAA-6 data were reliable only until the micropiles were installed during Stage 4. The jump in the lateral wall movement noted around day 65 was caused by installing a micropile within 1.1 m of SAA-6. Figure 3.9 shows the resulting lateral movements with depth. The largest movements occurred in the soft clay with a maximum value of 8 mm. In general, the effects of micropile installation were localized. However at SAA-6, the grouting operations in the bonded zone, which extended below the bottom of SAA-6, caused the bottom of the SAA to move as noted by the slope of the data at that point. This lack of a stable bottom makes the subsequent data from SAA-6 unreliable, and thus those data are not hereafter used in the analyses of this chapter.

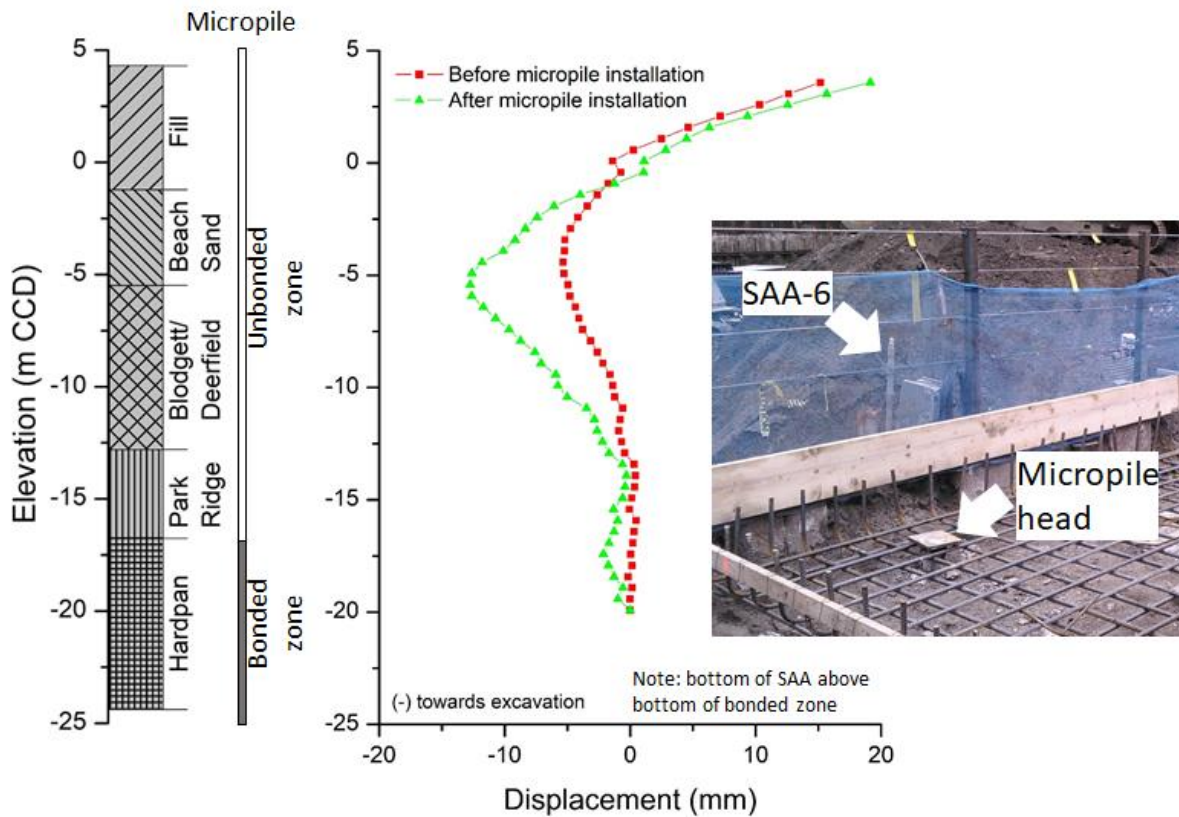


Figure 3.9 Localized effects of micropile installation

3.5.1 Settlements during Sheet Pile Installation

Optically surveyed settlement points (P.K. nails) were used to assess the settlements adjacent to the walls. Although settlement points were installed along the north and south walls, the data along the south wall collected after Stage 4 indicated no further settlement; this likely was a result of poor surveying rather than the actual responses. Therefore, only the settlements of the north wall will be considered and correlated with the excavation. Three rows of P.K. nails were installed at distances of 6.1, 9.0 and 11.9 m from the north wall.

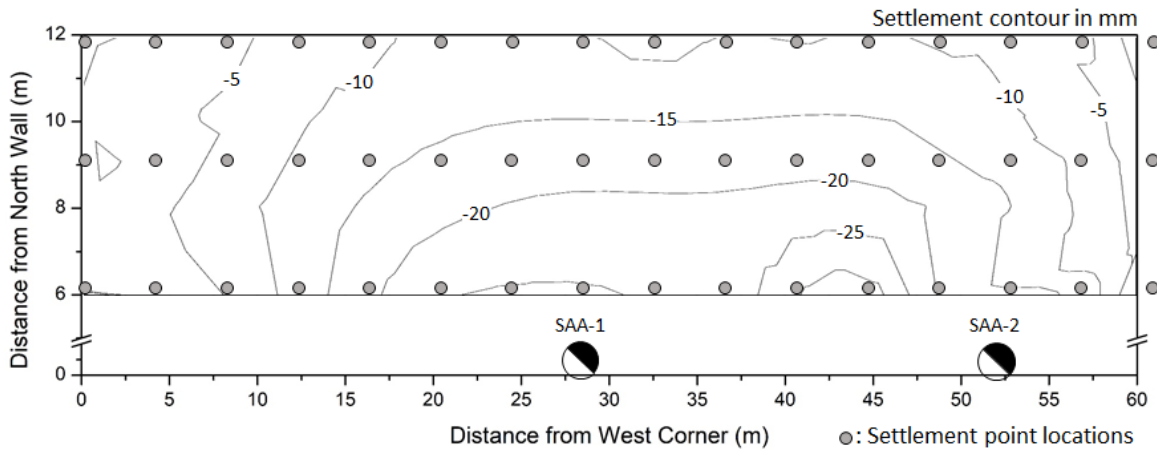


Figure 3.10 Total settlement after sheet pile installation (at Stage 3)

Figure 3.10 shows contours of settlements adjacent to the north wall at day 49, after the sheet piles were installed. Contours were determined by Delaunay triangulation (Delaunay 1934) as coded in the Origin software. At this time, the excavation had been lowered to elev. 0 m CCD. SAA-1 and SAA-2 indicated 8 mm and 2 mm of maximum cantilever wall movements, respectively, suggesting the vast majority of settlement shown in Figure 3.10 developed prior to excavation as a result of site preparation activities and the sheeting installation. These activities induced as much as 26 mm of settlement within 6 m of the wall. No additional settlements were observed during Stage 3 while the excavation was made to elev. -2.1 m CCD. Therefore, the settlement contour at day 49 can also be considered as the settlement at the end of Stage 3.

Settlements decreased with distance from the wall and from the center of the wall. This pattern of settlement likely arose because the sheets generally were installed from the edges

towards the center of the north wall. The maximum values located about 45 m from the west corner were a result of the difficulties installing the sheeting around existing drilled shaft foundations.

3.5.2 Movements during Excavation

The settlements measured by the optical settlement points and the lateral displacements measured by SAAs will be presented in relation to the excavation and support installation activities.

3.5.2.1 Settlements Adjacent to North Wall

Figures 3.11 through 3.13 show the total settlement contours at Stages 5, 7 and 9 as a result of the excavation. By Stage 3, settlements of approximately 26 mm had already occurred near the center of the north wall. As excavations were carried out, more settlements were observed. By the end of excavation at Stage 9, the maximum settlement was approximately 81 mm around the center of site (near SAA-1). A larger settlement was still observed about 45 m from the west corner as a result of sheet pile installation difficulties.

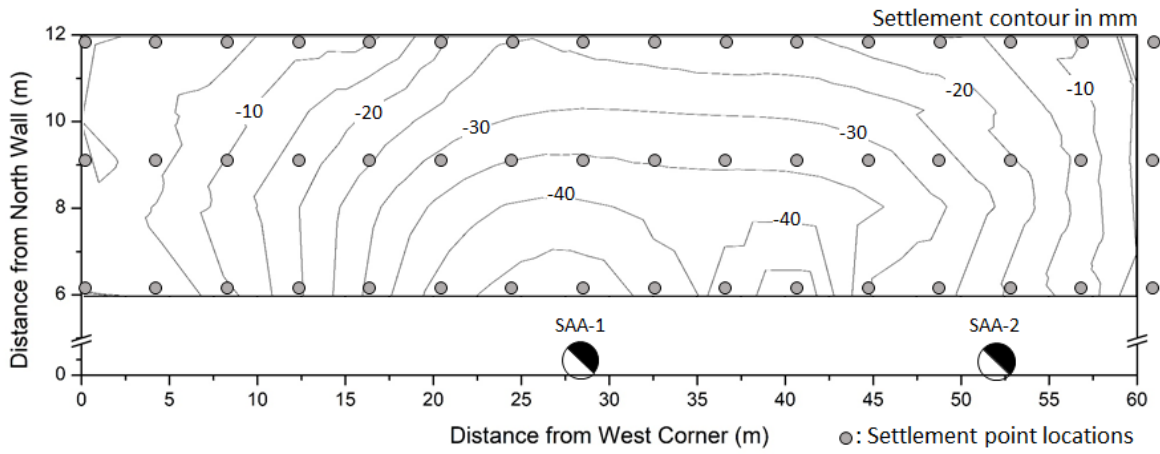


Figure 3.11 Total settlement at Stage 5

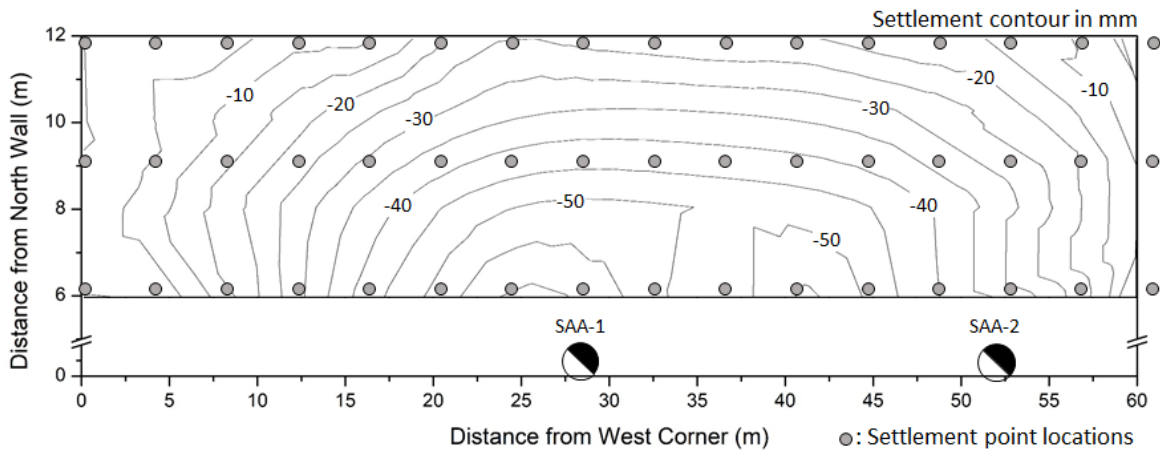


Figure 3.12 Total settlement at Stage 7

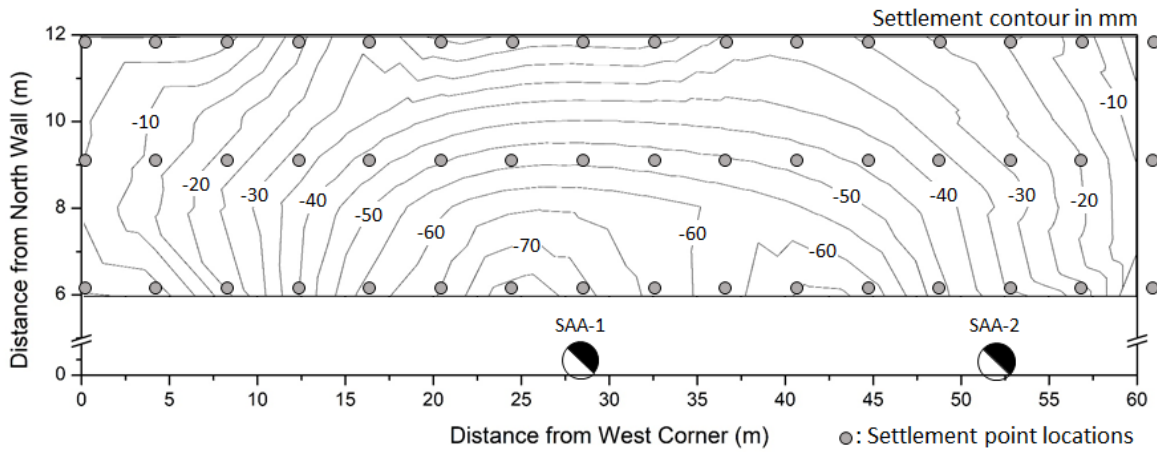


Figure 3.13 Total settlement at Stage 9

Figures 3.14 to 3.16 show the *incremental* settlements that occurred during excavation. These values represent the measured values at Stages 5, 7 and 9 minus those that occurred with site preparation and sheeting installation (Stage 3 as presented in Figure 3.10). The maximum settlement of 55 mm at Stage 9 was close to the center of the north wall, and may have been influenced by the locally deeper excavation (to elev. -11.3 m CCD as noted in Figure 3.6) for the tower crane at that location. The settlement contours showed more movements near the center of the excavation, arising from the stiffening effects of the corners of the excavation.

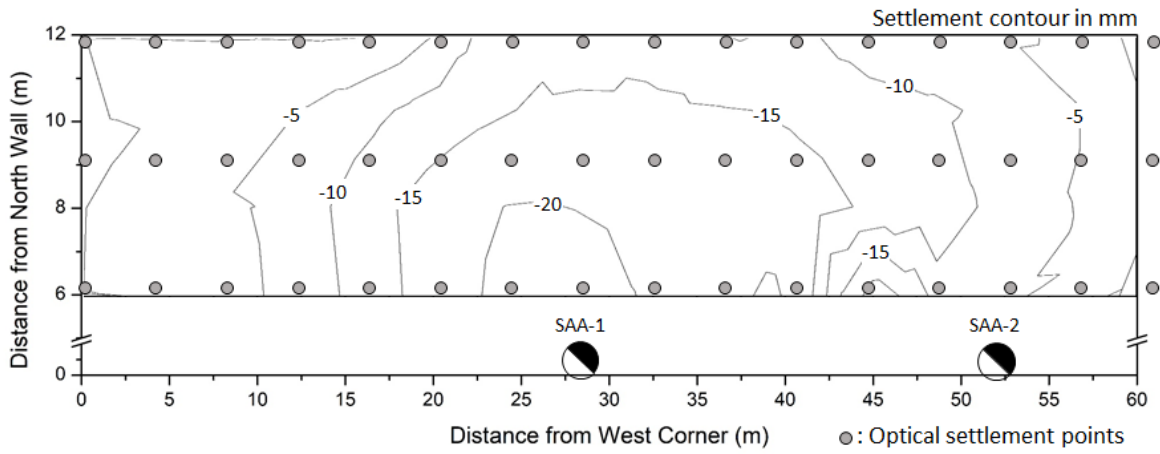


Figure 3.14 Incremental settlement from Stage 3 to Stage 5

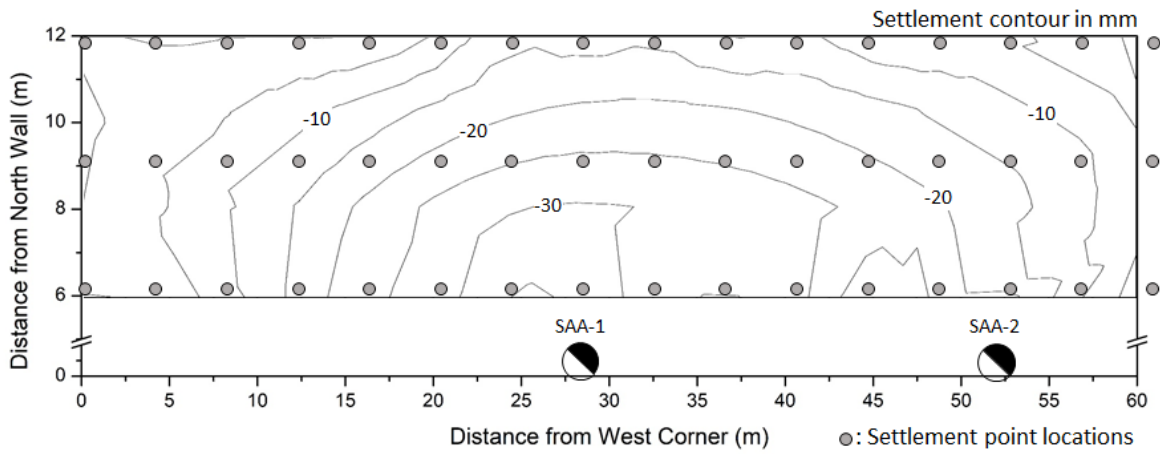


Figure 3.15 Incremental settlement from Stage 3 to Stage 7

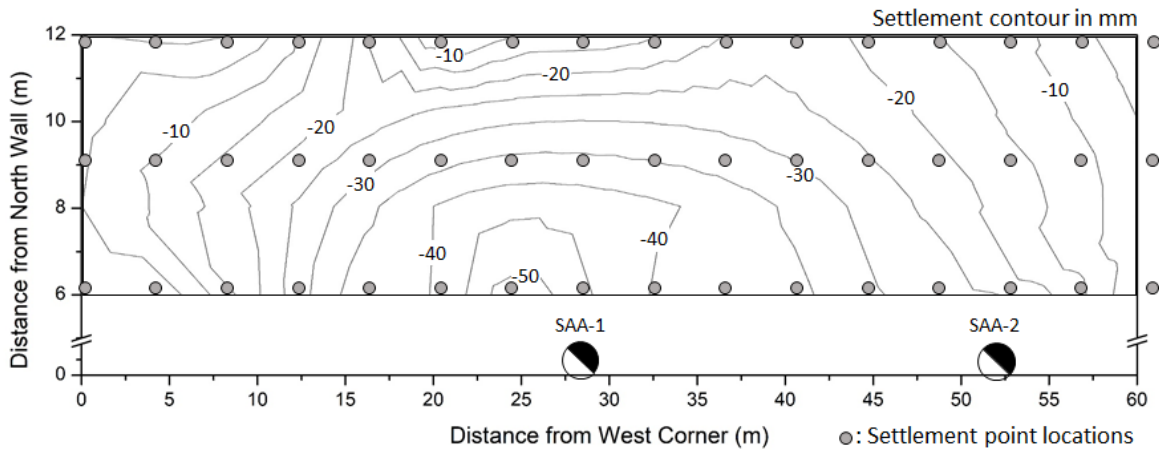


Figure 3.16 Incremental settlement from Stage 3 to Stage 9

3.5.2.2 Lateral Wall Movements

Figure 3.17 shows the lateral wall movements versus depth at the north wall during construction. Excavated grades at Stages 1, 3, 5, 7 and 9 are noted in the figure. The general responses in both SAA-1 and SAA-2 are similar. No more than 8 mm of lateral wall movements were noted until the excavation had reached the underlying soft to medium stiff clay during Stage 5. At that stage, the movements increased as the softer clays behind the wall and below the excavation were stressed in response to the excavation unloading, resulting in the largest incremental movements during excavation. At the end of excavation (Stage 9), the SAAs indicated maximum lateral movements of about 35 mm. The time-dependent movements are clearly seen in both SAAs as noted in Stage 10. About 4 mm of lateral movement occurred above the second level tieback level after the diagonal braces were removed during Stage 11.

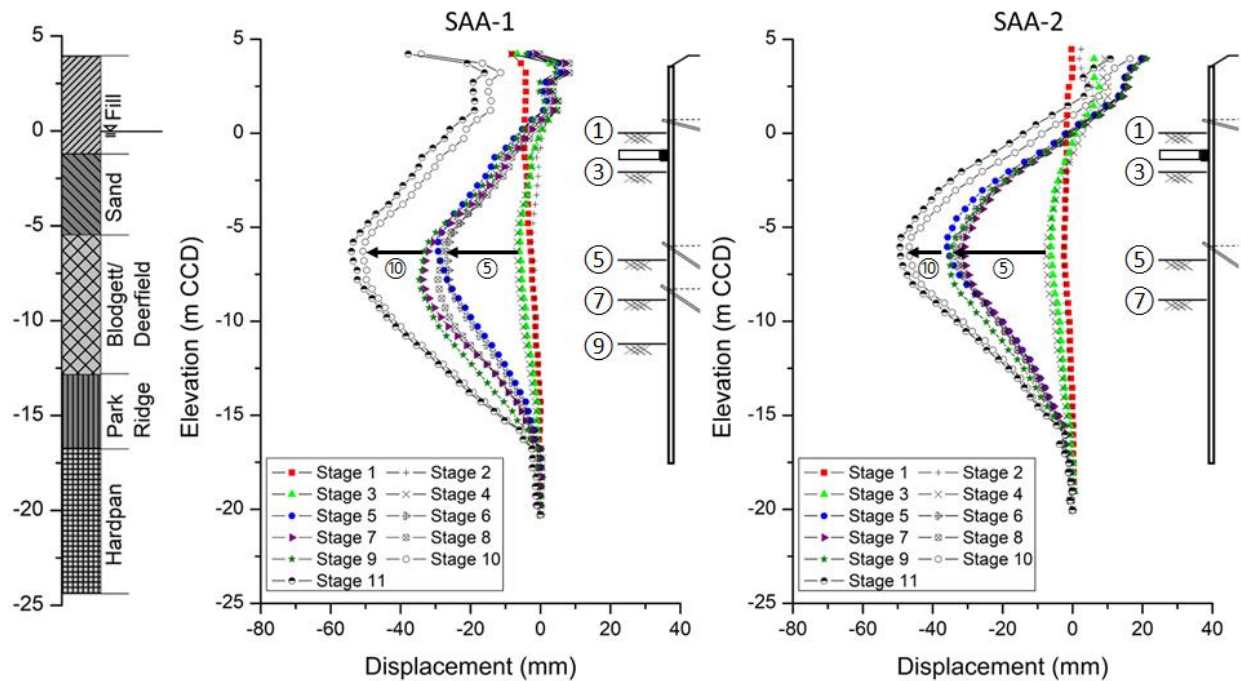


Figure 3.17 Lateral deformation of north wall with excavation stage

While apparent in the settlement data, the corner effects were not readily seen in the SAA data along the north wall. Little difference was observed in the lateral wall movements for SAA-1 at the center of the wall and SAA-2 8 m from the corner. The out-of-plane bending stiffness of the sheet pile walls depends on the rotational stiffness of the joints of the sheet pile sections, the double channel sections at the tieback levels, the WF sections at the diagonal brace level and also is affected by the horizontal spacing of the lateral supports. Apparently, the net effect of these factors results in lower out-of-plane stiffness than that perpendicular to the wall and reduced the impacts of the stiffening effects provided by the corners of the excavation such that similar lateral wall deformations occurred at the center at SAA-1 and 8 m from the northeast corner at SAA-2. This

trend also was observed in the Lurie Center as presented by Finno and Roboski (2005), where inclinometers at the center and near the corner did not show significant differences in lateral deformations. The stiffening effect of the corners were manifested in the ground surface settlements both at Lurie and SQBRC, as previously presented.

Figure 3.18 shows the lateral wall movements versus depth at the south wall during construction. Both SAA-5 and SAA-6 are shown, but the data represent responses to different construction activities. The data in SAA-5 show wall movements from Stage 4 due to the re-initialization at later dates compared to the other three SAAs. SAA-6 readings after Stage 4 are not shown due to their poor reliability caused by the grouting operations inducing the bottom of the SAA to move.

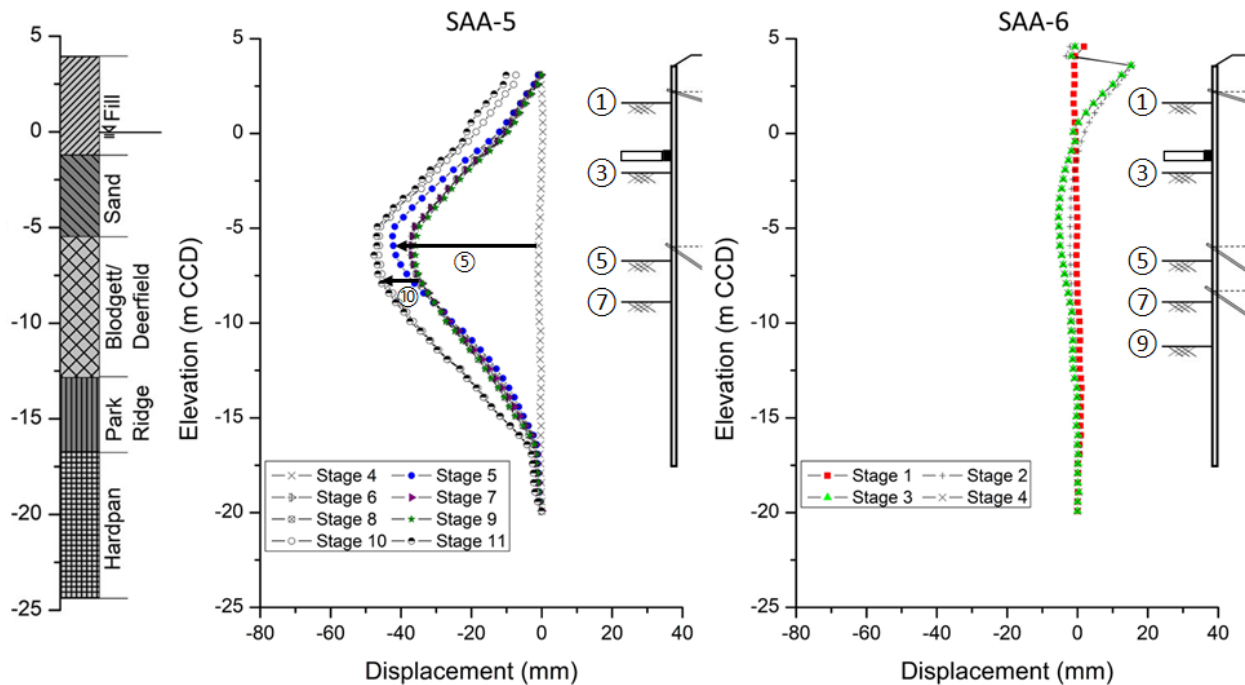


Figure 3.18 Lateral deformation of south wall with excavation stage

Note that the ramp was in place in front of SAA-5 when it was initialized, so likely no significant wall movements would have occurred prior to that time because the maximum excavated depth temporarily was 2.8 m to allow installation of the first tieback level at elev. +1.5 during Stage 2. The data from SAA-6 covers up to Stage 4 when a micropile was installed within 1.1 m causing the bottom of the SAA to move (Figure 3.9). SAA-6 indicates that very small movements occurred during the cantilever stage (Stage 1) of excavation as well as after the excavation was lowered to elev. -2.1 m CCD.

All SAAs show cantilever deformations during Stage 1. The top part of the sheet pile wall gets pulled back away from the excavation when the first level of tiebacks are installed at Stage 2. The largest incremental movement occurs during Stage 5 when the excavation reaches into the soft to medium stiff clay. Little movement was observed from Stage 5 to the end of excavation (Stage 9). After Stage 9, time-dependent movement was observed until flowable fill was placed between the sheet pile and permanent walls for the structure.

The general responses at the south are similar to those at the north wall, except that the presence of the ramp restrained movement until it was removed. Large incremental wall movements occurred at SAA-5 during Stage 5 when the ramp was removed and the grade was lowered to elev. -6.7 m CCD, reaching into the soft to medium stiff clay. Thereafter gradual inward movements were observed below elev. -8 m CCD. The maximum observed wall movement after reaching final excavation grade was 36 mm at SAA-5; however, as much as 5 mm of movement may have occurred prior to initialization, based on the response of SAA-6 at Stage 4. Therefore the maximum wall movement at SAA-5 during excavation can be estimated to be 41 mm.

Removing the cross-lot braces during Stage 11 resulted in small movements of 2 mm above the level of the diagonal braces.

The largest incremental movements at all SAA locations occurred when the soft to medium stiff clay was first excavated in Stage 5. The amount of movement that will occur as an excavation is lowered into a soft clay will depend the constitutive responses of the clay and on how deep the cut extends before the next level of support is placed (e.g., Finno and Roboski 2005). These two factors are keys to the ability to be able to predict ground responses in these conditions. If possible within the constraints of a project, the support levels in these soil conditions should be placed as soon as possible once the softer clay is exposed.

3.5.3 Movements after Final Grade Attained

Lateral wall movements continued to develop after final grade was reached in Stage 9. These movements arise from time-dependent responses and partly from diagonal brace removal. Note that the tieback levels below the diagonal brace were not de-tensioned. Lateral movements caused by the removal of struts were very small, as can be seen by comparing wall movements in Figure 3.17 and Figure 3.18 between Stages 10 and 11. Removal of the diagonal bracing had negligible impact on the wall movements, and thus movements that occurred after the end of excavation are due to material rate-dependent responses, pore water pressure dissipation, primarily in the soft to medium stiff clay, or due to removing the soil in the center of the excavation that is lower than the general excavated grade (Figure 3.6).

3.6 Evaluation of Measured Responses

The SQBRC site showed final lateral displacements slightly exceeding 50 mm, which according to the City of Chicago regulations, should have had contingency plans carried out for the supports of the excavation. However, these deformation levels occurred in the final stages of the excavation project with no observed damage to nearby utilities. Therefore, the lateral deformations exceeding 50 mm were not considered critical in the performance assessment.

Measured responses of the SQBRC excavation will be compared with other excavation projects in Chicago. Expected deformations for the support system stiffness will be calculated using semi-empirical methods proposed by Clough et al. (1989), and compared with the observed lateral wall movements.

3.6.1 Comparison with Other Excavation Performances

Ground and lateral wall deformations that developed during excavation at the adjacent Lurie Center have been presented by Finno and Roboski (2005) and Roboski and Finno (2006). Because of its proximity to SQBRC and the similarities of subsurface conditions, a comparison of the responses at the two sites is useful.

3.6.1.1 Settlement

The magnitude and extent of the sheet-pile induced movements shown in Figure 3.10 were greater than those measured at the adjacent Lurie Center (Glatt et al. 2004). At Lurie, the survey data collected after the completion of wall installation showed no settlements occurred beyond a distance of 12 m from the sheet pile wall. Within this distance, 25 % of the 198 monitoring points settled, with the magnitude varying between 2 mm and 15 mm. The larger movements at SQBRC likely were a combination of the site preparation and wall installation effects. The obstructions along the sheet pile wall alignment that resulted in hard driving conditions at the SQBRC were not present at Lurie.

3.6.1.2 Lateral Deformation

To provide insight to the degree of accuracy that one can expect at best when predicting lateral wall movements, Figure 3.19 shows the observed excavation-induced lateral wall movements at the end of mass excavation for both Lurie and SQBRC along with the excavated grades for each site. The excavated depth was 12.8 m at Lurie and 13.1 m at SQBRC. For this condition, the maximum lateral deformations showed a range of 19 mm at Lurie and 11 mm at SQBRC. To provide a common basis for comparison, the Lurie data shown in Figure 3.19 reflect conditions around the excavation that were not affected by the presence of timber piles or adjacent buildings (Finno and Roboski 2005) and only the data from the typical excavated grade (elev. -8.8 m CCD) at SQBRC is presented.

Deformations are larger at Lurie because it has a more flexible support system as will be later discussed in Section 3.6.2. Variations of the measured movements as percentage ranges from the average maximum deformations are $\pm 15.4\%$ for SQBRC and $\pm 15.2\%$ for Lurie. Given the similarity in soil conditions and bracing systems between the two cases and the good quality of the construction process at both sites (i.e., no over-excavation, good tieback installation techniques as noted by proof test acceptance, preloading and shimming of the cross-lot bracing at SQBRC), the range of movement shown in the figure provides an indication of the best accuracy one may expect when predicting lateral wall movements when good workmanship and careful data collection are employed in a project.

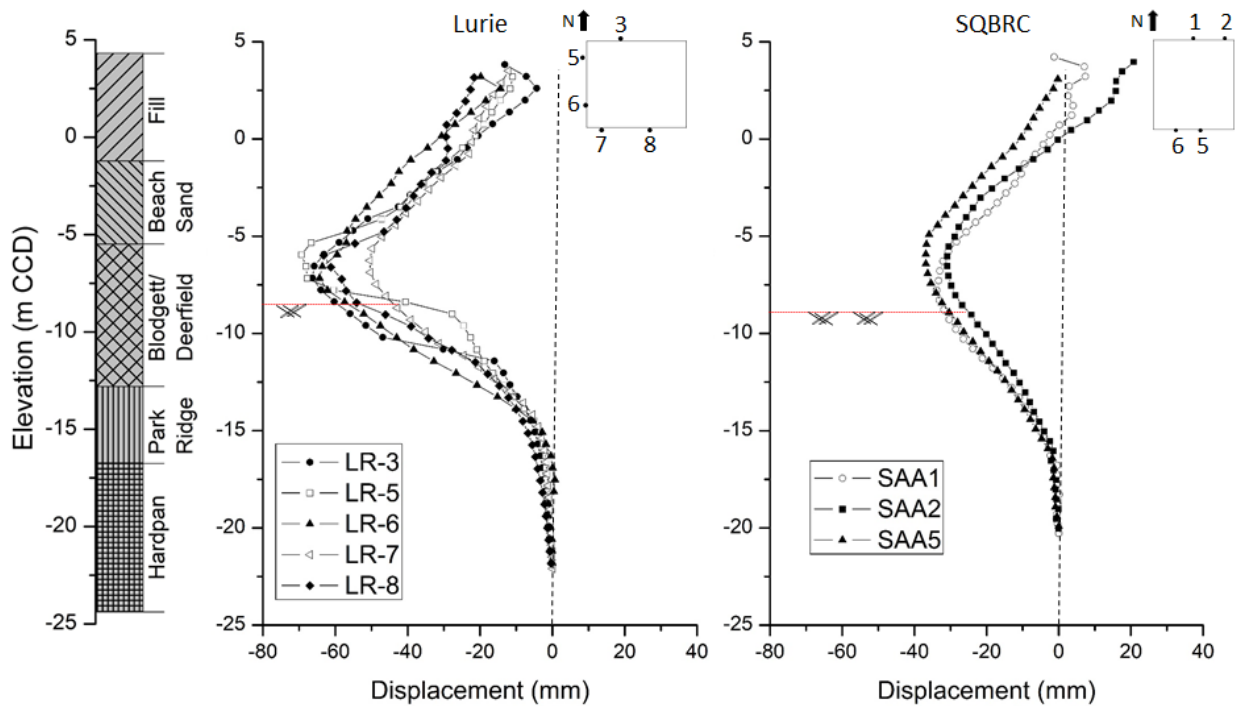


Figure 3.19 Lateral wall movements at end of mass excavation

These data suggest that predictions of lateral wall movements within $\pm 15\%$ of the maximum deformations are as good as can be obtained, given the natural variability of the relatively 'uniform' and well-characterized Chicago clays encountered at these two sites. Movements caused by other sources, such as micropile installation, sheet pile installation, long-term effects, will increase the error if one does not explicitly consider them.

3.6.1.3 Comparison of Maximum Lateral and Vertical Deformations

The ratio of maximum ground surface settlement to maximum lateral wall movement is of interest when making estimates of movements associated with supported excavations. Semi-empirical methods such as Clough et al. (1989) yield a maximum lateral wall movement, from which a maximum settlement must be estimated. Ratios of maximum settlement to maximum lateral wall movement typically range from 0.6 to 1, and with this maximum settlement, the settlement variation with distance from a wall can be estimated by empirical methods, such as Hsieh and Ou (1998).

Figure 3.20 shows a plot of the maximum lateral deformation and incremental ground surface settlements during excavation for SQBRC and Lurie for the later stages of excavation when the excavations had reached the softer clays. Lines depicting ratios of vertical and horizontal movement of 100 and 80 % ratios are shown for reference. The SQBRC data indicated that there is approximate 1:1 relation between settlement and maximum wall movement at the later stages of excavation. However, no such clear trend is noticed when one considers the Lurie data which show that the ratio at the end of excavation varies approximately between 0.8 and 1. Ratios smaller than

1.0 indicate that constant volume conditions were not maintained. One would expect that to be the case when about 10 m of granular soils were present at the ground surface. In any case, a conservative estimate for preliminary design can be based on the 1:1 ratio. However additional sources of settlements must be explicitly considered when estimating total ground surface settlements.

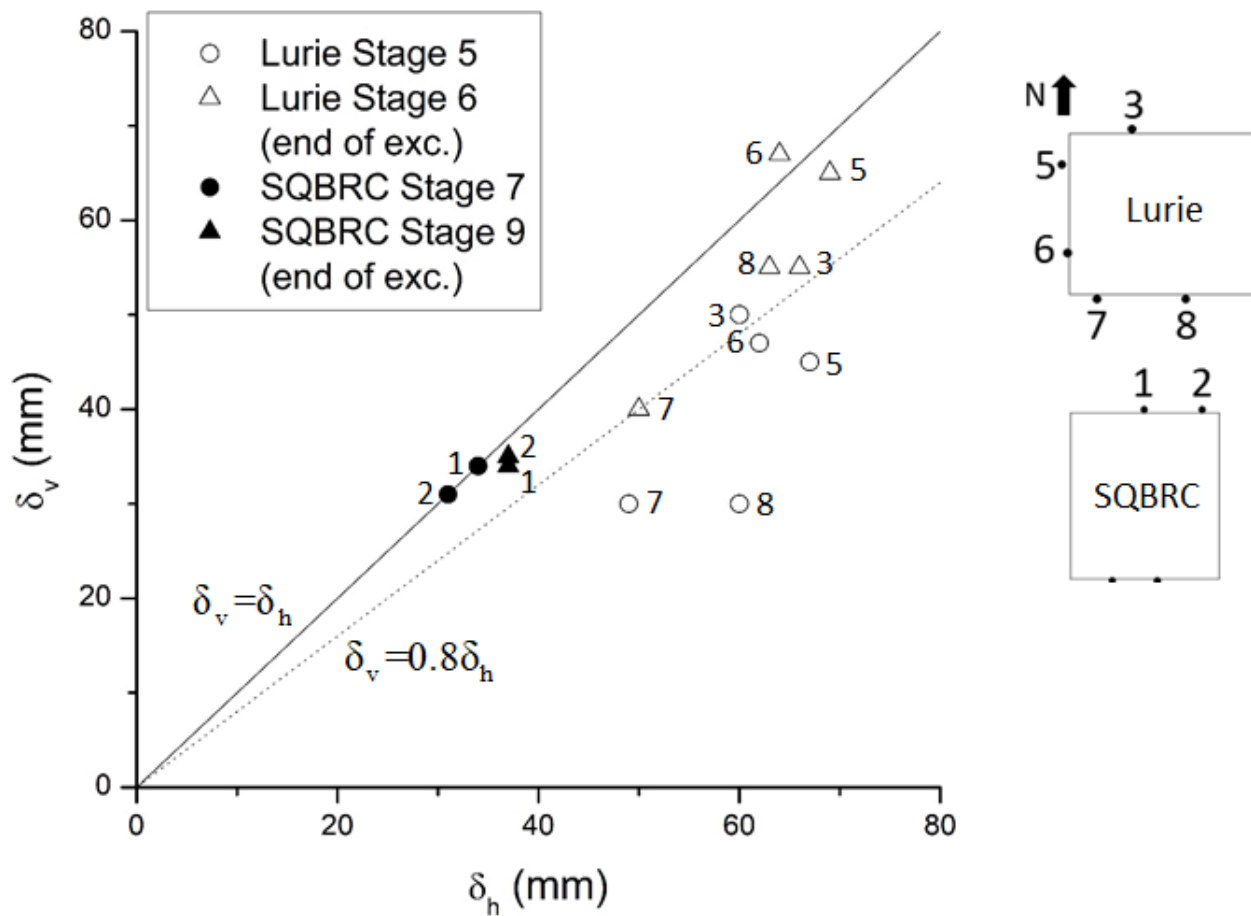


Figure 3.20 Maximum lateral wall movements and maximum settlement

3.6.1.4 Movements after Final Grade Attained

Rate-dependent responses have also been observed in other excavations in Chicago, for example at the Chicago-State (Finno et al. 2002) and Lurie Center excavations (Finno and Roboski 2005). The rates of movements are shown in Table 3.2. The values are small, with an average value for all sites of about 3 mm/month (excluding SAA-6). In cases where the allowable movements are small for a project, if the excavation remains open and the space between the temporary and permanent wall is not filled or otherwise braced for a long period of time after the final excavated grade is attained, then this small additional movement may become significant.

Table 3.2 Observed time-dependent response in excavations in Chicago

	SQBRC	Lurie	Chicago-State
Time-dependent response (mm/month)	4.8 (SAA-1) 3.0 (SAA-2) 2.2 (SAA-5) 0.3 (SAA-6)	1.7	2.8

3.6.2 Evaluation of Performance through Semi-Empirical Method

The observed maximum lateral wall movements that developed during excavation at both sites are compared to those expected based on system stiffness and factor of safety against basal heave in Figure 3.21. The system stiffness and the factor of safety (FS) against basal heave were calculated for Stages 5, 7 and 9 (end of excavation) at SQBRC and for Stages 5 and 6 (end of excavation) at the Lurie Center. The average vertical spacing of support (h) used for the system

stiffness calculations were assessed by the excavation depth and number of supports installed for each stage. At the stages considered, the excavations had reached the soft to medium stiff clays. The final excavated depth was 12.8 m at Lurie and 13.1 m at SQBRC. The system stiffness values ranged from a flexible system at Lurie to a stiffer system at SQBRC with values at each site varying at each stage, as a function of depth of excavation and average vertical spacing of support. The FS was computed using Terzaghi's method (1943) (see Appendix). In each case, the depth of the failure surface below the excavation D was limited by the stiffer Park Ridge or Hardpan layers.

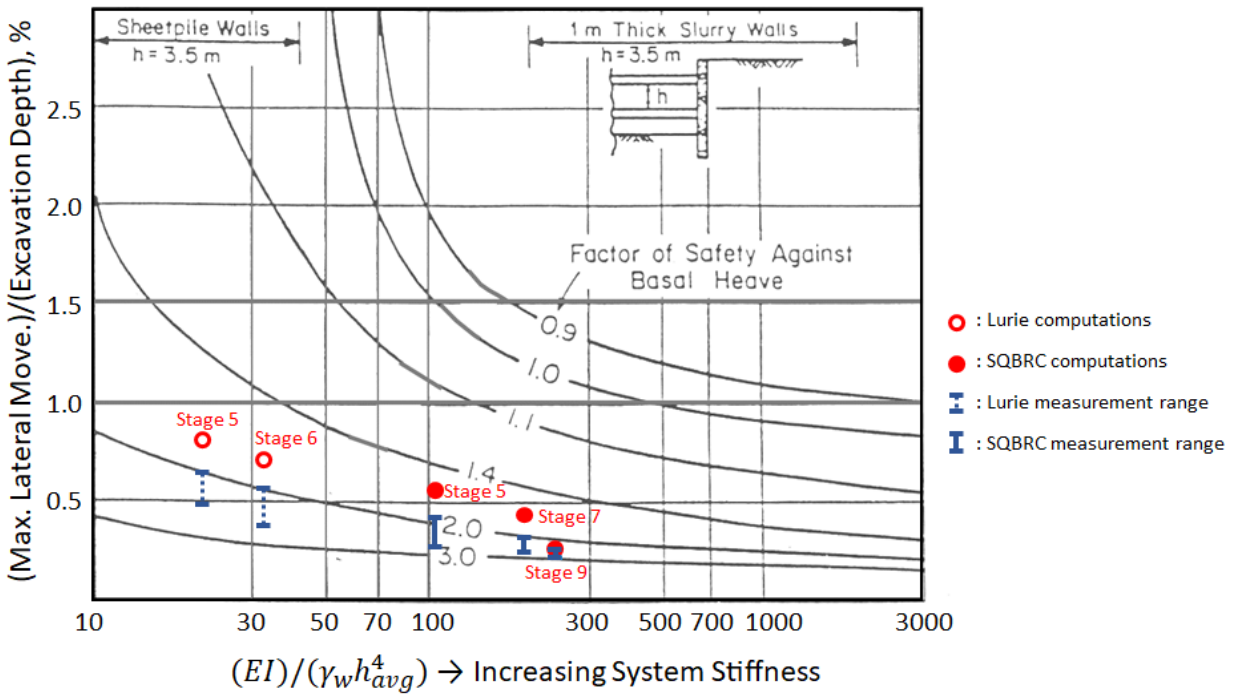


Figure 3.21 Computed and measured normalized wall movements
(adopted from Clough et al. 1989)

Based on the system stiffness and the FS against basal heave, the expected normalized wall movements at Lurie and SQBRC are shown as open and closed red circles, respectively, in Figure 3.21. The range of normalized wall movements based on the three SAA locations (SAA-1, SAA-2, and SAA-5) at SQBRC and the five inclinometer locations (LR-3, LR-5, LR-6, LR-7, and LR-8) at the Lurie Center are shown in brackets at the corresponding system stiffness. These observed values are consistently lower than the expected values, except for the last stage of the SQBRC excavation. However, the trends in the normalized movements follow the expectation that smaller normalized movements will occur with increasing system stiffness, and that as the FS is larger and the bottom of the excavation more stable, the increased system stiffness has a smaller effect on reducing the magnitudes of the normalized lateral movements.

The fact that the observed normalized lateral wall movements follow the expected trends, but with lower magnitudes, emphasizes the need to conduct site specific analyses when employing a stiffness-based design. The magnitudes will depend on the actual stress-strain-strength responses of the soils. Estimates based on semi-empirical methods such as Clough et al. (1989) are means to quickly obtain expected magnitudes of wall movements, and should be a first step in design. In the data shown in Figure 3.21, the observations were about one-half the expected values for all but one set of data. Note that the finite element simulations that partially formed the basis of the Clough et al. (1989) chart are based on an elastic-perfectly plastic constitutive model (Mana and Clough 1981) for which a linearly elastic response is assumed until failure is reached. Given this model will represent a first order approximation of soil response, one should conduct site specific finite element analyses with more realistic soil models if limiting deformations is a key design issue.

3.7 Summary and Conclusions

Ground surface settlements and lateral wall deformations that developed during excavation for the SQBRC were presented and shown to be correlated with the construction process. The performance of the excavation support system was assessed by comparison with those expected based on semi-empirical methods. The movements at the SQBRC site also were compared to those measured previously as excavation occurred at the adjacent Lurie Center to evaluate the highest degree of accuracy with which one may make such predictions.

Less than 8 mm of lateral wall movements were noted until the excavation reached the underlying soft to medium stiff clay. Large incremental movements occurred when the excavation was lowered into the soft to medium stiff clay. Time-dependent lateral wall movements developed at a rate of about 3 mm/month and persisted until a structural connection was made between the temporary and permanent support walls. Maximum lateral movements thus also depend on the amount of time before a temporary wall is structurally constrained.

The intermittent presence of an access ramp at the south wall influenced the development of lateral wall movements at that location as observed by SAA-5. No significant lateral movement was observed until the access ramp was removed. Comparing the wall movements at the end of excavation for the north and south walls, the presence of the access ramp apparently had little impact on the ultimate values. However, if one desires to use observations to track design estimates or update performance predictions, then the effects of the ramp must be accounted for in the process.

Given the similarity in soil conditions, bracing systems and the range of lateral wall movements observed at the SQBRC and Lurie sites, one can expect at best to be able to predict lateral wall deformations at various locations around a site in similar cases with an accuracy of no more than $\pm 15\%$. The ratio of excavation-induced maximum settlement to maximum lateral wall movement varies with excavation depth. At later stages near the end of excavation, the ratios based on measurements were approximately 0.8 to 1.0 for both SQBRC and Lurie Center cases.

The normalized wall movements at SQBRC caused by cycles of excavation and bracing varied between 0.22 and 0.32 % at the last two stages of excavation. These measured values are smaller than estimates based on the Clough et al. (1989) chart using system stiffness and factor of safety against basal heave. Estimates based on semi-empirical methods are means to quickly obtain expected magnitudes of wall movements. For a more precise assessment of wall movements, one should conduct site specific finite element analyses with more realistic soil models.

Chapter 4 Optimizing Soil Parameters based on Lateral Wall Movements at SQBRC

4.1 Introduction

This chapter presents the optimizations of soil parameters based on the lateral wall movements at SQBRC. These optimizations follow the sequence that one would use if making these optimizations during the course of the excavation.

A plane strain model of the excavation was developed using PLAXIS 2D so updated performance predictions can be made at key stages, for example when the excavation is made below a support (i.e., tieback or diagonal internal strut) elevation and the excavated surface is uniform so that a plane strain condition is applicable to the field situation. While it would have been ideal to use data collected at several locations to optimize parameters, this was not possible because of the complexity of the excavation sequence. To consider plane strain conditions, measurements located at the center of both the north and south wall would have been used for the optimization process. But because of the intermittent presence of the access ramp at the center of the south wall, the movements were negligible, and thus not useful for optimization at that location until the later stages of construction. Consequently, only data collected at the north wall were used in the optimization process during excavations, although as will be seen, the FEM simulation included both walls and the entire excavation for realistic representations.

To obtain the most benefit from the adaptive management approach, soil parameters need to be optimized during earlier stages of an excavation project and applied to later stages of the project to predict future performance. While this was done for this project in near real time using the HC model (Finno et al. 2017), this chapter includes only analyses conducted after the end of excavation, and thus represent “Class C” predictions. Herein, three soil models were used to represent the soft to medium stiff (Blodgett/Deerfield) and stiff (Park Ridge) clay layers: the Hardening Soil Model (HS model), the Hardening Soil Model with Small-Strain Stiffness (HSS model) and the Hypoplastic Constitutive Model (HC model). Initial parameters for each of the soil models were based on previous inverse analysis studies that have been carried out for Chicago soils. Correlation and sensitivity analyses were carried out for the HC model to choose the most appropriate soil parameters to be optimized. Optimization was then conducted with inverse analysis based on a gradient method, as presented by Finno and Calvello (2005).

Soil parameters optimized based on the SQBRC excavation performance are compared to past inverse analysis studies to assess whether the parameters were reasonable. Soil parameters optimized in early stages of the project were used to compute the soil deformation of later stages.

4.2 Problem Definition: 2D Finite Element Model

The modeling details of the support system and excavation stages used in the 2D finite element mesh are presented in this section. The initial soil parameters for the three constitutive soil models also are summarized and the basis of their selection is discussed.

4.2.1 2D Mesh

The finite element code PLAXIS was used to make the 2D computations. Figure 4.1 shows the finite element mesh and the idealized soil stratigraphy for the SQBRC excavation. Five soil layers were used as presented in Section 3.2.1.

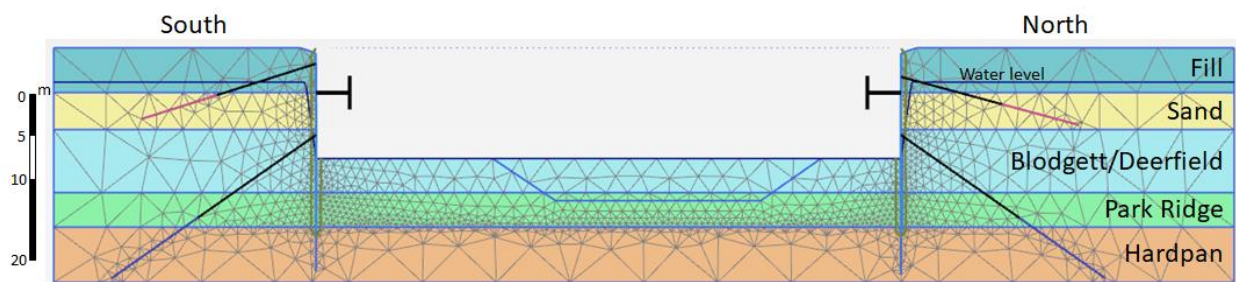


Figure 4.1 Finite element mesh of north-south cross section of SQBRC

Note that the mesh is a north-south section through the center of site. The east-west section was not used for the optimization due to the existence of the Lurie Center to the west and the RIC Building to the east. The existence of basement levels for these caisson-supported buildings limited the lateral deformations, and therefore is of limited interest to this work. The existence of the access ramp on the south wall restricted the lateral wall movements until the ramp was completely removed in later stages of the excavation. Therefore, the optimization was only carried out for the north wall, and the existence of the access ramp was neglected in the finite element model.

Because the model represents a cross-section along the center of site, the mesh represents plane strain conditions and allows comparisons using SAA-1 positioned at the center of the north

wall. The width of the excavation was 67 m. The right (north) boundary is located 40 m from the north wall to ensure it is far enough from the zone of influence of movements. The left (south) boundary is located at 35 m from the south wall for the same reason. The bottom boundary of Hardpan extends to elev. -23.2 m CCD so that it reaches beyond the bottom of the bonded zone for the lower tieback level. Simulations using the boundary conditions results in settlements at the end of excavation of approximately 1 and 3 mm at the right and left boundaries, respectively, small enough to consider that the boundaries are sufficiently far from the walls so as not to influence the results.

The “medium” element distribution in PLAXIS was used for the mesh generation. The initial groundwater level was at elev. 0 m CCD. Fifteen-node triangular elements were used to define the mesh. Zero horizontal displacements were imposed on the lateral boundaries of the mesh. On the bottom boundary, zero horizontal and vertical displacements were imposed.

4.2.2 Support System

The structural elements comprising the north and south walls are described, because these walls were considered in the optimization process. Structural properties of the supports used in the analyses are summarized in Table 4.1.

Table 4.1 Structural properties of supports

	Sheet pile wall	1 st level tieback		2 nd level tieback		Strut
	H3707	Unbonded zone	Bonded zone	Unbonded zone	Bonded zone	Pile ^(a)
Type of element	Plate	Anchor	Embedded beam row	Anchor	Embedded beam row	Anchor
Bending stiffness, EI (kN·m ² /m)	4,426,000	-	-	-	-	-
Axial stiffness, EA (kN/m)	1,848,000	-	-	-	-	-
Element thickness (m)	0.71	-	-	-	-	-
Poisson's ratio, ν	0.2	-	-	-	-	-
Young's modulus, E (kN/m ²)	-	-	7,995,000	-	6,675,000	-
Axial stiffness, EA (kN)	-	146,000	-	219,000	-	6,985,000
Max. skin friction, $T_{skin,max}$ (kN/m)	-	-	120.6	-	131.1	-

^(a) 915 mm outside diameter with 16 mm thickness

The retaining system consisted of H3707 sheet pile walls with typically two tieback levels and a single level of diagonal internal bracing. The sheet pile wall was modeled by isotropic elastic plate elements with its material properties defined by the axial stiffness, EA and flexural rigidity (bending stiffness), EI.

Tieback ground anchors were installed to provide lateral restraints for the wall. Tiebacks have a three-dimensional geometry, and their representation in plane strain involves significant approximations. The first level of tiebacks was installed at elev. +2 m CCD on the north wall, and elev. +7 m CCD on the south wall. The unbonded 4-strand part of the anchors, which was used for the first level of tiebacks, was represented by anchor elements spaced at 1.4 m. The bonded zones of the anchors were represented with elastic embedded beam row elements predefined as massive circular piles with diameters of 0.15 m, and horizontal spacings of 1.4 m. For the friction parameters of the bonded zone, the following values of load transfer (termed “skin friction (T_{skin})” in PLAXIS) were used:

$$T_{\text{skin,start,max}} = T_{\text{skin,end,max}} = \frac{2 \cdot DL}{\text{bonded length}} = \frac{2 \cdot 551 \text{kN}}{9.1 \text{m}} = 120.6 \text{kN/m} \quad (4.1)$$

where DL is the design load.

The second level of tiebacks consists of 6-strand unbonded zones represented by anchor elements spaced at 1.4 m. The bonded zones of the second level tiebacks are similar to the first level tiebacks, but are defined as circular piles with diameters of 0.2 m. The friction parameters were:

$$T_{\text{skin,start,max}} = T_{\text{skin,end,max}} = \frac{2 \cdot DL}{\text{bonded length}} = \frac{2 \cdot 800 \text{kN}}{12.2 \text{m}} = 131.1 \text{kN/m} \quad (4.2)$$

As typically done, the wales supporting the diagonal internal braces were not represented in the 2D model because they had a very little impact on the lateral deformation perpendicular to the wall. The struts were represented as fixed-end anchors spaced at 6.1 m. Because the internal struts were installed diagonally, perfect representation of this in the plane strain model contained

many assumptions. The diagonal struts were modeled as cross-lots with equivalent lengths of 32.0 m, which represented the innermost diagonal strut length. In addition, the axial stiffness of the diagonal strut was set so it represented the component perpendicular to the sheet pile wall.

Areas with additional tieback levels and deeper excavations were not represented in the model since the conditions were not representative of the entire site, only present at a few locations, and thus are three-dimensional rather than plane strain. All supports were wished-in-place, and installation effects such as vibrations were not considered.

4.2.3 Modeling Stages

The excavation sequence to the nominal full excavation depth (elev. -8.8 m CCD) can be organized into 11 modeling phases as in Table 4.2. The entire simulation was assumed to be undrained; no time effects from pore water pressure changes were considered. The construction stages of interest for the optimization are ones that are representative of plane strain conditions where excavations were made to 0.6 or 0.9 m below each level of support before they were installed. Construction stages (see Section 3.3) that correspond to when the excavation was completed to each level before support installation are Stages 1, 3, 5 and 7, which correspond to modeling phases 4, 6, 8 and 10, respectively, in the finite element model. Additional levels of excavations at the center of the north wall and at center of the entire site were not represented in the finite element model because optimizations were to be made only at excavation levels that strictly represent plane strain conditions. For consistency with the performance analysis, the construction stages will be used throughout this thesis instead of the modeling phases. The second

column of Table 4.2 indicates the calculation type in which the “plastic” calculation represents an elasto-plastic deformation analysis carried out in either fully drained (for granular materials) or undrained (for clays) conditions, depending on the soil type.

Table 4.2 Modeling phases in relation to construction stages of Chapter 3

Modeling phases	Calculation type	Activity	Construction stages
Initial	K_0 consolidation	Initial soil condition	-
1	Plastic	Sheet pile wall installation	0
2	Plastic	Excavation to elev. +1.5 m CCD	1 (south)
3	Plastic	First level tieback on south wall at elev. +2.1 m CCD (Prestress: 330 kN)	2 (south)
4	Plastic	Excavation to elev. 0 m CCD	1 (north)
5	Plastic	First level tieback on north wall at elev. +0.6 m CCD (Prestress: 330 kN)	2 (north)
6	Plastic	Excavation to elev. -2.1 m CCD	3
7	Plastic	Strut installation at elev. -1.2 m CCD	4
8	Plastic	Excavation to elev. -6.7 m CCD	5
9	Plastic	Second level tieback at elev. -6.1 m CCD (Prestress: 490 kN)	6
10	Plastic	Excavation to elev. -8.8 m CCD	7

Stage 1 represents the cantilever deformation stage where the top section of the wall moves toward the excavation before the first level tiebacks are wished-in-place and pre-loaded. Stage 1 was not used for the optimization because deformation levels were negligible.

Stage 3 (Phase 6) represents the stage where the excavation was made below the first tieback level into the beach sand. Small deformations were observed at this stage (maximum wall movements of 6 mm). It was at Stage 5 (Phase 8) that the excavation reached into the soft to medium stiff clay layer below the internal strut level, and relatively large incremental deformations were observed and computed. Stage 7 (Phase 10) indicates when the excavation is made to elev. - 8.8 m CCD, which was the final excavation depth that was uniformly made on the entire site. Stages after that indicate excavations that were carried out nonuniformly around site, and thus are 3D conditions. As a result, optimizations were carried out for Stages 3, 5 and 7, which represented plane strain conditions of uniform excavation depths around the entire site.

4.2.4 Selection of Field Measurements

To optimize the lateral deformations at various distances behind the wall, the use of both SAAs and inclinometers were considered. Due to the presence of the adjacent structures on the east and west walls, finite element models included a north-south section through the site. The presence of the access ramp made conditions on the south wall three-dimensional for most of the excavation. As such, the optimization procedure was applied to conditions at the north wall during the excavation because the conditions there could be represented as plane strain at the times when the excavated level was uniform across the entire north wall.

SAA-1 was chosen because it properly represented the plane strain conditions at the center of the north wall. Note that similar responses were observed in SAA-1 and SAA-2, as discussed in Section 3.5.2.2. Inclinometer measurements were erratic and could not be properly related to the construction activities in a consistent manner, as presented in Section 3.4. Therefore, inclinometer measurements were not used in the inverse analysis. Figure 4.2 shows the lateral deformation with depth at stages that represented plane strain conditions for SAA-1.

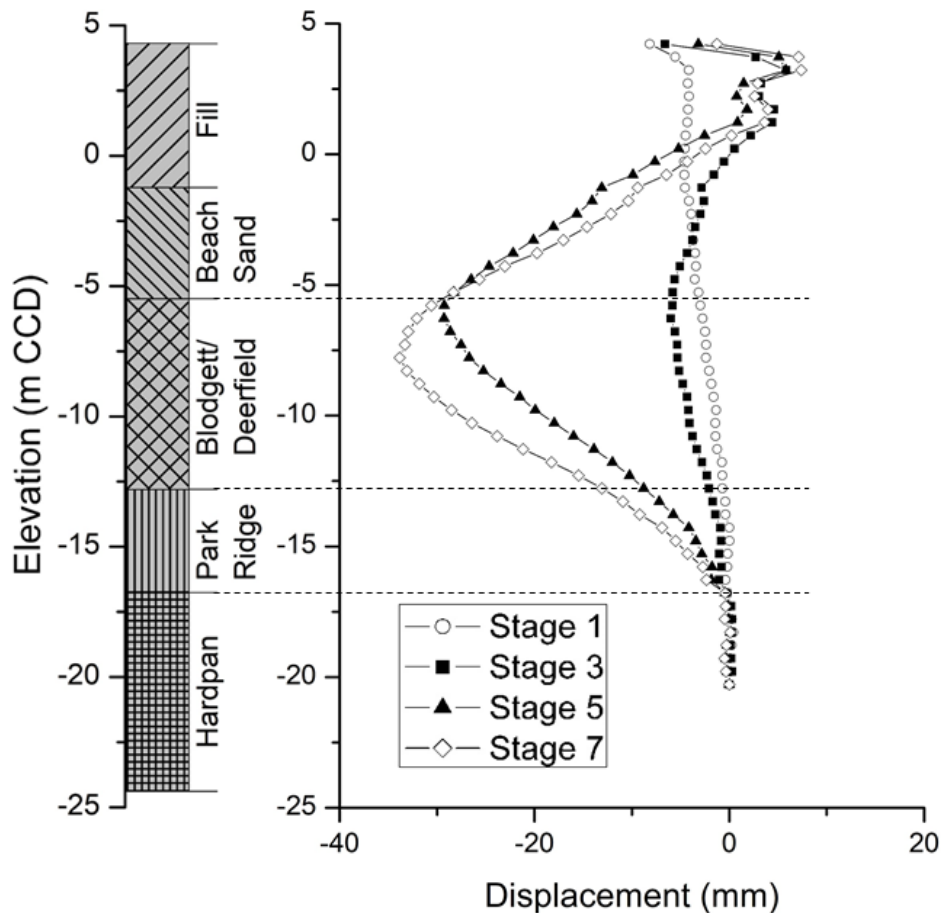


Figure 4.2 Deformations for SAA-1 used in inverse analysis

Deformations measured in the Blodgett/Deerfield and Park Ridge layers were used for optimization purposes. The response of the Blodgett/Deerfield stratum had the largest effect on the performance of SQBRC, as discussed in Section 3.5. The lateral deformations in the deeper hard clays (Hardpan) were usually very small and their parameters are usually selected so as to minimize deformations rather than match field or lab test data.

4.2.5 Estimates of Soil Parameters for Constitutive Models

The first step in an optimization process is to select soil parameters to provide the initial estimate of response. For this purpose, the soil parameters were selected based on previous studies of soil parameter optimizations in the Chicago area, as discussed in the subsequent section.

4.2.5.1 Hardening Soil Model

The HS model successfully reproduced the profile of lateral displacements in magnitude and shape at the Chicago-State excavation (Finno and Calvello 2005). Therefore, the model was used to represent the stress-strain responses of all soil strata, with parameters shown in Table 4.3.

Initial E_{50}^{ref} parameters of the clay layers shown in Table 4.3 were based upon the parameters optimized from excavations at Chicago-State (Calvello 2002, Calvello and Finno 2004, Finno and Calvello 2005), Lurie Center and Ford Center (Rechea 2006), and Block 37 sites (Mu et al. 2015; Mu and Huang 2016) (Table 4.4). Note that all p^{ref} values correspond to 100 kPa.

Table 4.3 Initial HS model parameters used for optimization

Soil parameters	Soil strata				
	Fill	Sand	Blodgett/ Deerfield	Park Ridge	Hardpan
Type	Drained	Drained	Undrained	Undrained	Undrained
E_{50}^{ref} (kPa)	13,500	48,000	12,500	150,000	200,000
$E_{\text{oed}}^{\text{ref}}$ (kPa)	13,500	48,000	8,750	105,000	140,000
$E_{\text{ur}}^{\text{ref}}$ (kPa)	40,500	144,000	37,500	450,000	600,000
P^{ref} (kPa)	100	100	100	100	100
m	0.5	0.5	0.8	0.85	0.6
c^{ref} (kPa)	19	0.2	0.2	0.2	0.2
ϕ (°)	30	35	26	32	35
ψ (°)	2	5	0	0	0
v_{ur}	0.2	0.2	0.2	0.2	0.2
OCR	1	1.1	1.4	1.5	2.5

Table 4.4 E_{50}^{ref} (kPa) values optimized for various excavations in Chicago

	Chicago- State	Lurie				Ford	Block 37	SQBRC
		Stage 4		Stage 6				
		LR-6	LR-8	LR-6	LR-8			
Blodgett	4,100	11,300	13,000	5,060	6,000	6,090	10,000	12,500
Deerfield	9,900					14,200	14,000	
Park Ridge	34,000	78,900	93,900	129,000	52,200	21,300	32,000	150,000
Hardpan	300,000 (fixed)	118,400	140,900	193,500	78,300	300,000 (fixed)	-	200,000 (fixed)

While the Blodgett layer of the Chicago-State excavation site was observed to be very soft, the Deerfield stratum of Chicago-State was more similar to the Blodgett/Deerfield layer of SQBRC. Therefore, more weight was given to the optimized parameter of the Deerfield stratum than the

Blodgett layer for the Chicago-State. Parameters for the Lurie Center were optimized with deformations measured for two stages at two inclinometer locations. The optimized parameter of Blodgett/Deerfield from Lurie Center were given more weight than other sites due to the proximity with the SQBRC site. Optimized parameters from the Ford Center and Block 37 sites represented optimized parameter values of the same magnitude range as the Chicago-State and Lurie Center cases. All optimized parameters from the four case studies were considered for the initial parameters of the SQBRC site with weights based on the proximity with the SQBRC site.

The Hardpan layer was assigned a large value with more weight given to the values optimized in the Lurie excavation. The E_{50}^{ref} value for Hardpan was fixed throughout the optimization process, as was for the Chicago-State and Ford Center excavations because it was found that changes in stiffness of the hard clays made negligible differences in the soil response. The initial E_{50}^{ref} parameter for Park Ridge was chosen through the relationship with the Hardpan that was employed for the Lurie Center optimization:

$$(E_{50}^{ref})_{\text{Hardpan}} = 1.5 \cdot (E_{50}^{ref})_{\text{Park Ridge}} \quad (4.3)$$

Soil parameters other than the E^{ref} values for the clays and all parameters for the Fill and Sand were taken directly from Rechea (2006) as were used for the representation of the lateral displacement response of the adjacent Lurie Center.

These parameters were used to compute wall deformations using PLAXIS 2D. Results of computations made using the soil parameters in Table 4.3 are compared with observations in Figure 4.3. The figure shows that the lateral deformations near the wall (SAA-1) at Stages 5 and 7 were quite close to the field measurements in the clays. This agreement indicates that the use of

optimized parameters from other excavation sites can provide reasonable estimates of deformations at excavations in similar geologic conditions. However, the computed deformations in the Blodgett/Deerfield at Stage 3 were slightly larger than observed while the smaller deformation levels in the Park Ridge layer were properly captured at Stage 3.

To assess the soil parameters which provided the best fit between the measurements made from SAA-1 and computations made from PLAXIS for all stages of excavation, soil parameter optimization was carried out. Following the recommendations of Finno and Calvello (2005), the parameters chosen for optimization of the HS model were the reference values of the primary loading stiffness, E_{50}^{ref} , in the Blodgett/Deerfield and Park Ridge layers. The other two reference stiffness values, E_{oed}^{ref} (tangent stiffness for primary oedometer loading), and E_{ur}^{ref} (unloading/reloading stiffness) were also indirectly optimized with $E_{oed}^{ref} = 0.7 \cdot E_{50}^{ref}$ and $E_{ur}^{ref} = 3.0 \cdot E_{50}^{ref}$. Results of the optimization will be presented in Section 4.3.2.1.

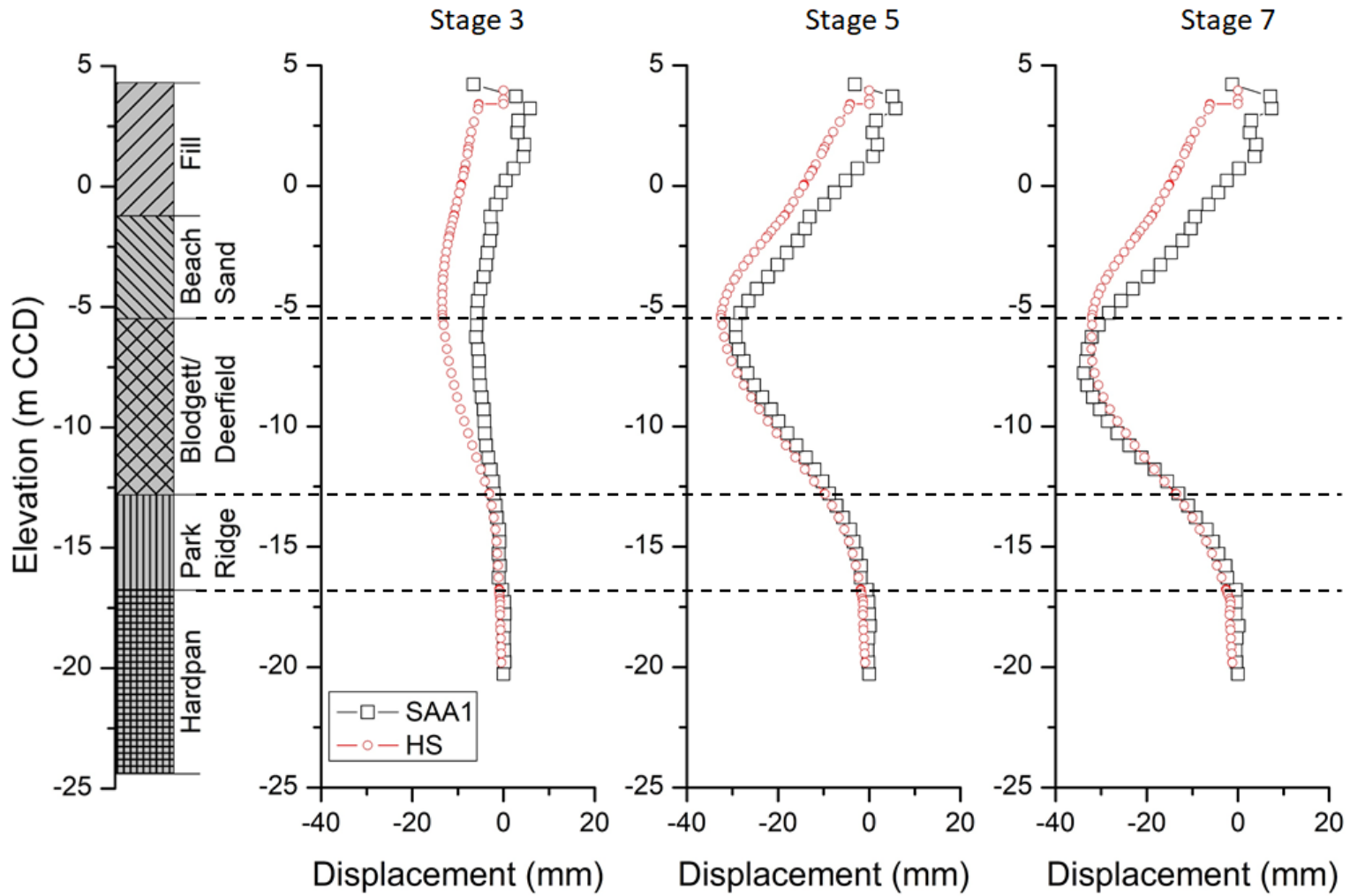


Figure 4.3 Computations of lateral deformation using initial HS parameters

4.2.5.2 Hardening Soil Model with Small-Strain Stiffness

The HSS model uses the same parameters as the HS model plus two parameters that incorporate small-strain stiffness behavior: the initial shear modulus, G_0 , and the shear strain level at which the secant shear modulus is reduced to 70% of its initial value, $\gamma_{0.7}$. Initial parameters used for the HSS model in this thesis are shown in Table 4.5. Note that only the Blodgett/Deerfield and Park Ridge layers were represented by the HSS model; the remaining strata were modeled with the HS model.

Table 4.5 Initial HSS model parameters used for optimization

Soil parameters	Soil strata				
	Fill	Sand	Blodgett/Deerfield	Park Ridge	Hardpan
Type	Drained	Drained	Undrained	Undrained	Undrained
E_{50}^{ref} (kPa)	13,500	48,000	12,500	35,000	200,000
$E_{\text{oed}}^{\text{ref}}$ (kPa)	13,500	48,000	8,750	24,500	140,000
$E_{\text{ur}}^{\text{ref}}$ (kPa)	40,500	144,000	37,500	105,000	600,000
P^{ref} (kPa)	100	100	100	100	100
m	0.5	0.5	0.8	0.85	0.6
c^{ref} (kPa)	19	0.2	0.2	0.2	0.2
ϕ (°)	30	35	26	32	35
ψ (°)	2	5	0	0	0
ν_{ur}	0.2	0.2	0.2	0.2	0.2
OCR	1	1.1	1.4	1.5	2.5
G_0^{ref} (kPa)	-	-	93,300	138,500	-
$\gamma_{0.7}$	-	-	1.00×10^{-04}	1.00×10^{-04}	-

Initial E_{50}^{ref} parameters of the Blodgett/Deerfield and Park Ridge layers were based upon the optimizations carried out for the Block 37 excavation (Table 4.6). As was presented in Chapter 2, optimized E_{50}^{ref} parameters of the HSS model were slightly lower than the E_{50}^{ref} values of the HS model in the Block 37 excavation. The initial E_{50}^{ref} parameter used in the HS model was again employed in the HSS model for the Blodgett/Deerfield layer to check whether the E_{50}^{ref} value of the HSS model reaches lower values than the HS model when optimized with the SQBRC case.

To select the initial values for the E_{50}^{ref} values for the Park Ridge layer, the following optimization results from the Block 37 excavation were considered: (a) the optimized E_{50}^{ref} value for the HSS model was approximately 60 % higher in the Park Ridge layer than the Blodgett and Deerfield layers; (b) the E_{50}^{ref} value for the HSS model in the Park Ridge was approximately one-third of the value for the HS model. Using the same trends, an initial value of 35,000 kPa was selected as the E_{50}^{ref} value for the Park Ridge HSS model at SQBRC.

Table 4.6 Comparison of optimized Block 37 and initial SQBRC parameters

	Optimized Block 37 parameters			Initial SQBRC parameters		
	HS model	HSS model		HS model	HSS model	
	E_{50}^{ref} (kPa)	E_{50}^{ref} (kPa)	$\gamma_{0.7}$	E_{50}^{ref} (kPa)	E_{50}^{ref} (kPa)	$\gamma_{0.7}$
Blodgett	10,000	8,200	7.64×10^{-05}	12,500	12,500	1.00×10^{-04}
Deerfield	14,000	7,600	6.56×10^{-05}			
Park Ridge	32,000	12,700	7.21×10^{-05}	150,000	35,000	1.00×10^{-04}

Shear velocity measurements were obtained from cross-hole tests carried out at the Ford Center and One Museum Park West in Chicago (Figure 4.4), as presented by Finno et al. (2012). G_0 values were calculated with the equation $G_0 = \rho V_{hv}^2$ at selected depths in the Blodgett/Deerfield and Park Ridge layers of SQBRC as noted in Figure 4.4. Computed G_0 values with depth are shown as points in Figure 4.5.

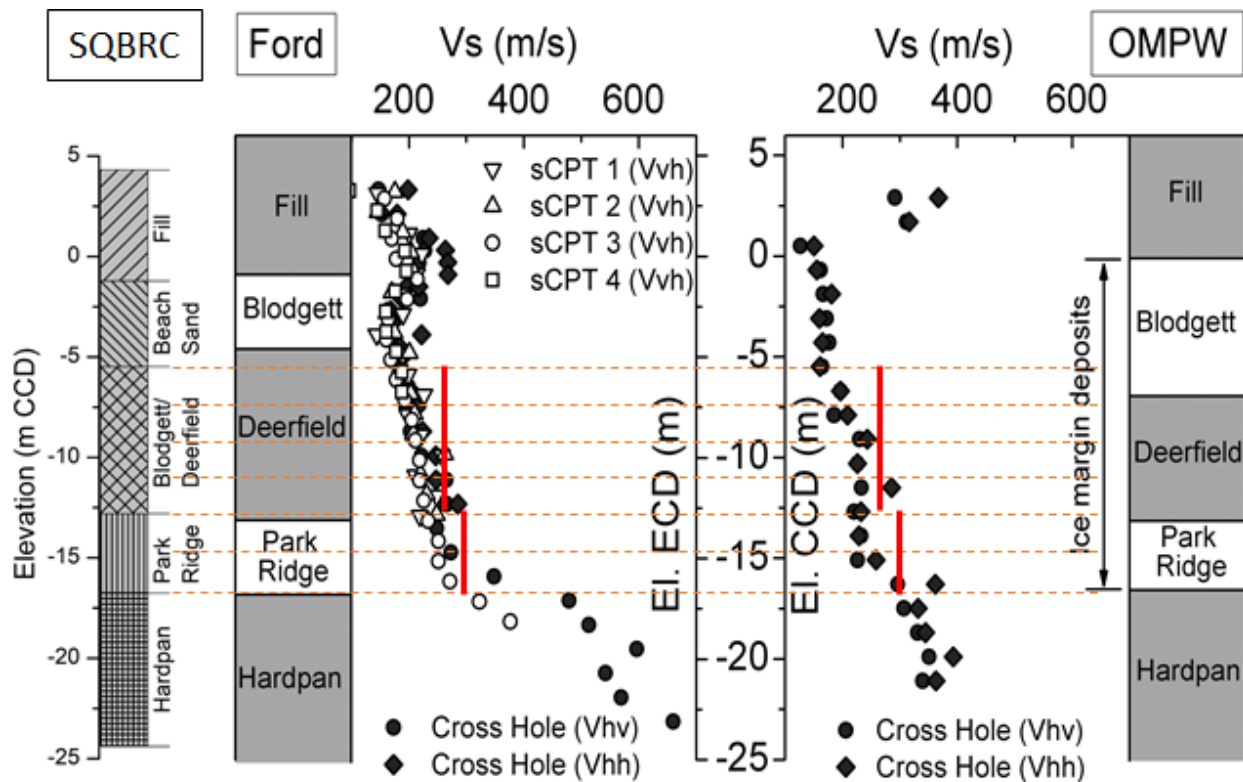


Figure 4.4 Shear velocity data obtained from cross hole tests (taken from Finno et al. 2012)

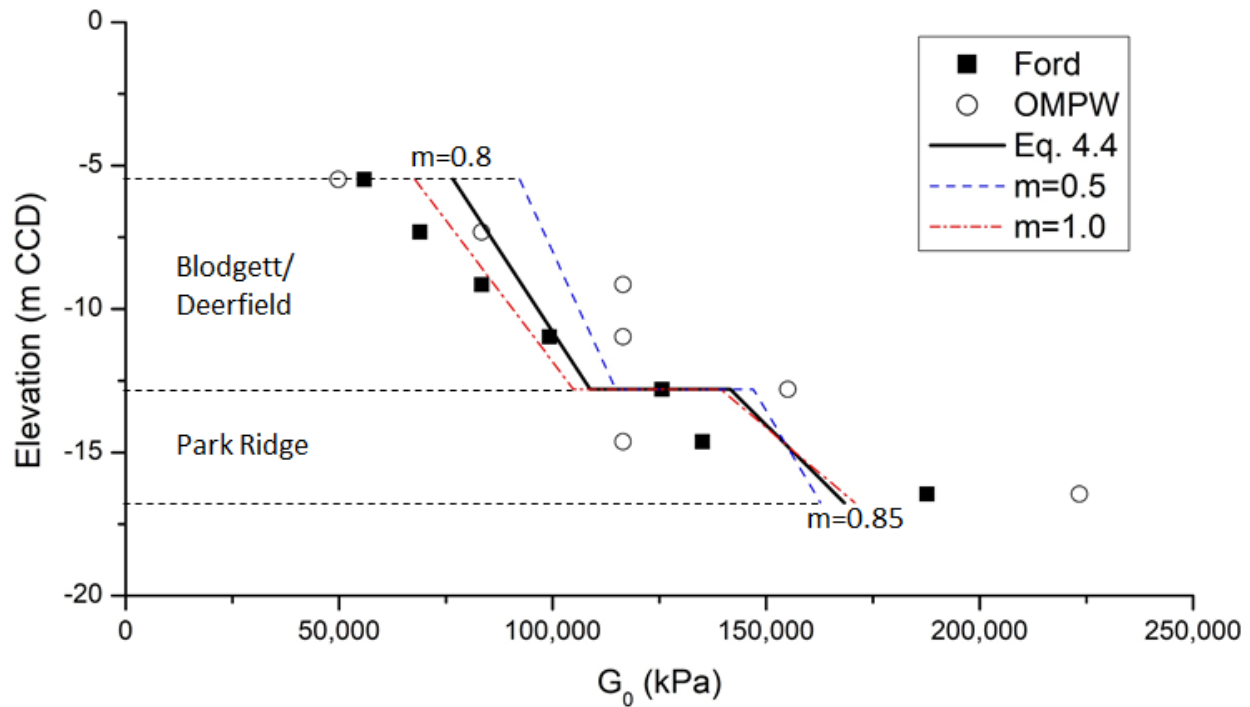


Figure 4.5 G_0 calculated from shear velocity data vs. G_0 with depth calculated from assumed G_0^{ref} values

To determine G_0^{ref} values for the two clay layers, Equation 4.4 was considered:

$$G_0^{ref} = G_0 \left(\frac{c \cdot \cos \varphi - \sigma'_3 \cdot \sin \varphi}{c \cdot \cos \varphi + p^{ref} \cdot \sin \varphi} \right)^{-m} = \rho V_{hv}^2 \left(\frac{c \cdot \cos \varphi - \sigma'_3 \cdot \sin \varphi}{c \cdot \cos \varphi + p^{ref} \cdot \sin \varphi} \right)^{-m} \quad (4.4)$$

Representative shear velocities of 270 and 300 m/s were used for the Blodgett/Deerfield and Park Ridge layers, respectively, as illustrated in red lines of Figure 4.4. Figure 4.5 shows that the calculated G_0 results from assumed G_0^{ref} values, plotted as straight lines, agree reasonably well with the G_0 values calculated from the measured shear velocities (plotted as points). Changes in the m value within the range of 0.5 and 1.0 made slight differences in the shear stiffness with depth, but were fixed with the initial values given in Table 4.5 due to the large variance in the shear

velocity measurements. As a result, the G_0^{ref} values were selected to be 93,300 kPa and 138,500 kPa for the Blodgett/Deerfield and Park Ridge, respectively.

The small-strain stiffness parameter $\gamma_{0.7}$ was optimized using field measurements of the Block 37 excavation (Mu et al. 2015; Mu and Huang 2016). Because the optimized $\gamma_{0.7}$ values from the Block 37 case did not show a clear trend ranging from 6×10^{-05} to 8×10^{-05} , the initial value of $\gamma_{0.7}$ for the SQBRC study was taken as 1.0×10^{-04} as was assumed for the initial parameter estimates of the Block 37 optimization.

Estimates of the initial parameters summarized in Table 4.5 were used in the results of the computations shown in Figure 4.6 and show that the computed lateral deformations near the wall (SAA-1) at Stage 3 agree well with the field observation. The computed deformations at Stages 5 and 7 are slightly underpredicted in the Blodgett/Deerfield and larger than observed in the Park Ridge layer. Although the computations did not show perfect fits with the measurements, reasonable agreement is observed between computed and measured results. These results again show the utility of defining soil parameters based on past performance data when evaluating excavation-induced deformations in similar geologic conditions.

For a better fit with the field measurement, E_{50}^{ref} and $\gamma_{0.7}$ parameters of the Blodgett/Deerfield and Park Ridge were optimized as recommended by Mu et al. (2015). As was the case for the HS model, $E_{\text{oed}}^{\text{ref}}$ and $E_{\text{ur}}^{\text{ref}}$ were indirectly optimized with $E_{\text{oed}}^{\text{ref}} = 0.7 \cdot E_{50}^{\text{ref}}$ and $E_{\text{ur}}^{\text{ref}} = 3.0 \cdot E_{50}^{\text{ref}}$. G_0 was relatively well studied through cross-hole tests and did not need to be altered. Results of the optimization will be presented in Section 4.3.2.2.

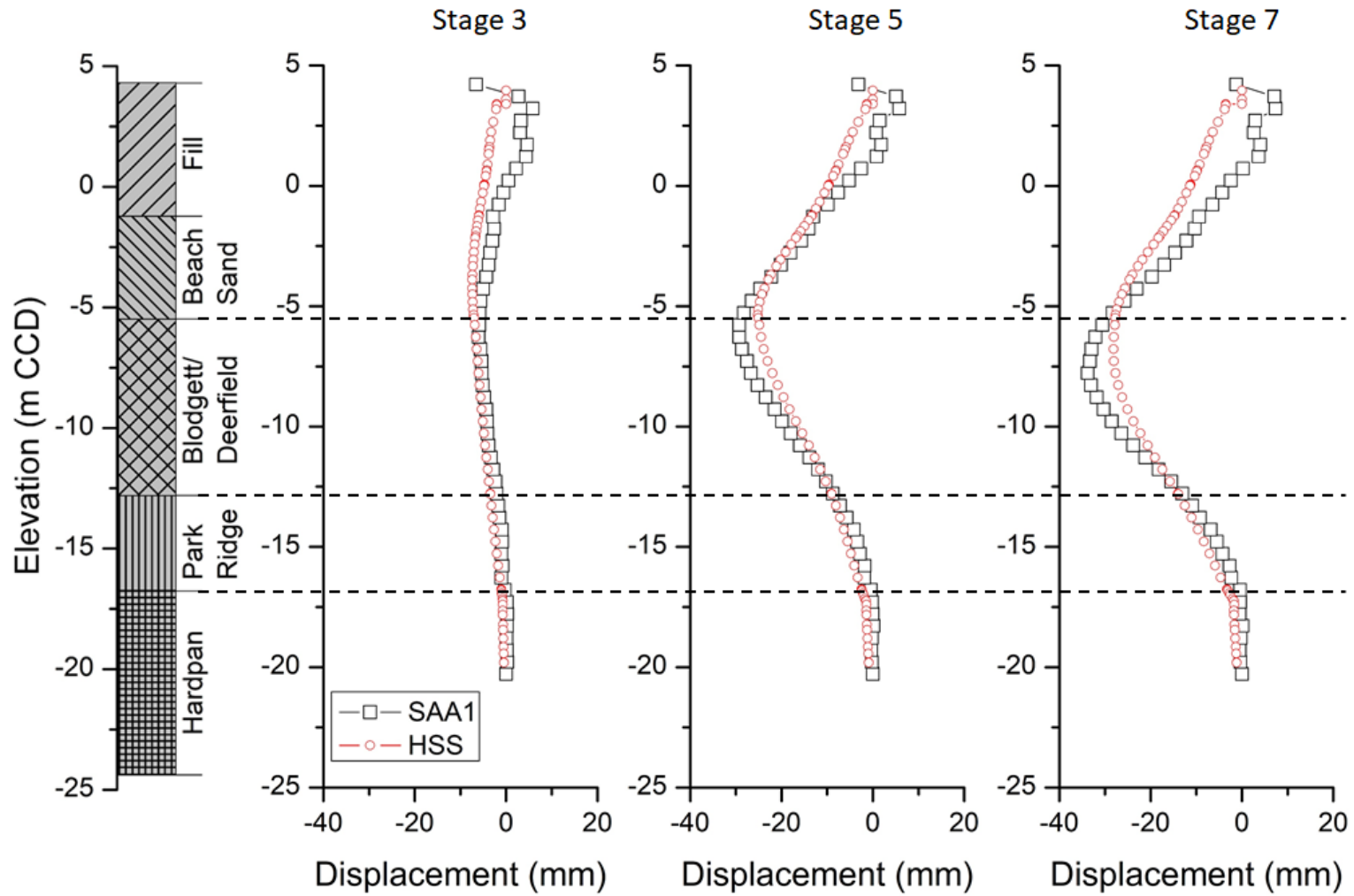


Figure 4.6 Computations of lateral deformation using initial HSS parameters

4.2.5.3 Hypoplastic Constitutive Model

The HC model developed by Masin (2014) was used in the plane strain analyses to represent the responses of the two clay strata (Blodgett/Deerfield and Park Ridge). The HC model was chosen for its ability to represent small-strain behavior through the intergranular strain concept. In this class of models, deformations are not divided into elastic and plastic components with a yield surface as in elasto-plastic models.

Parameters for the HC model have been determined via inverse analysis of laboratory test results (Sarabia 2012, Arboleda-Monsalve 2014). Initial estimates of the parameters for the Blodgett/Deerfield and Park Ridge clay layers were taken from the values reported by Arboleda-Monsalve (2014), which were also employed in the finite element model of the OMPW excavation (Table 4.7).

In Arboleda-Monsalve's work, the Blodgett/Deerfield and Park Ridge layers were modeled as four strata: Blodgett, Deerfield, Upper Park Ridge and Lower Park Ridge. Averaged parameter values from the OMPW case were used for the initial estimates of the Blodgett/Deerfield and Park Ridge layers of SQBRC. The friction angle was estimated with the semi-empirical relationship between the critical state friction angle and the natural water content proposed by Sarabia (2012):

$$\sin(\phi'_{cv}) \approx 0.7385 - 0.9384w_n \quad (4.5)$$

Parameter A_g was calculated using the shear velocities measured at OMPW and Ford Center. The HS model was used for soil layers other than two clay layers of interest. Parameters for these soil layers were kept identical to those used in the HS model.

Table 4.7 Initial HC model parameters used for optimization

Soil parameters	OMPW				SQBRC	
	Blodgett	Deerfield	Upper Park Ridge	Lower Park Ridge	Blodgett/Deerfield	Park Ridge
λ^*	0.062	0.062	0.055	0.050	0.06	0.05
κ^*	0.0113	0.0113	0.014	0.012	0.012	0.012
N	0.76	0.76	0.62	0.55	0.76	0.64
φ_c	25.3	31.7	36.0	37.8	33	35
v_{pp}	0.15	0.15	0.15	0.15	0.15	0.15
A_g	4,100	4,100	4,100	4,100	4,100	11,000
n_g	0.6	0.6	0.6	0.6	0.6	0.6
$\alpha_g, \alpha_E, \alpha_v$	1.1	1.1	1.1	1.1	1.1	1.1
m_{rat}	1	1	1	1	1	1
R_{max}	5.0×10^{-05}	5.0×10^{-05}	2.4×10^{-05}	2.4×10^{-05}	5.0×10^{-05}	2.4×10^{-05}
β_r	0.18	0.18	0.18	0.18	0.18	0.18
χ	1.3	1.3	1.3	1.3	1.3	1.3

Results of computations using the HC model are presented in Figure 4.7. These results show that the computed lateral deformations near the wall (SAA-1) at Stage 3 agree reasonably well with measured values. However, the deformations at Stages 5 and 7 are slightly overpredicted in the Park Ridge, and underpredicted in the Blodgett/Deerfield layer. However, reasonable agreement is observed between computed and measured results, showing the utility of defining soil parameters based on past laboratory test data when evaluating excavation-induced deformations.

There are no previous studies of optimizations carried out using field measurements for the HC model. To perform optimizations with field measurements, sensitivity and correlation analyses were carried out for the HC model parameters to assess which soil parameters should be optimized. Details of the sensitivity and correlation analyses are described in Section 4.3.1.

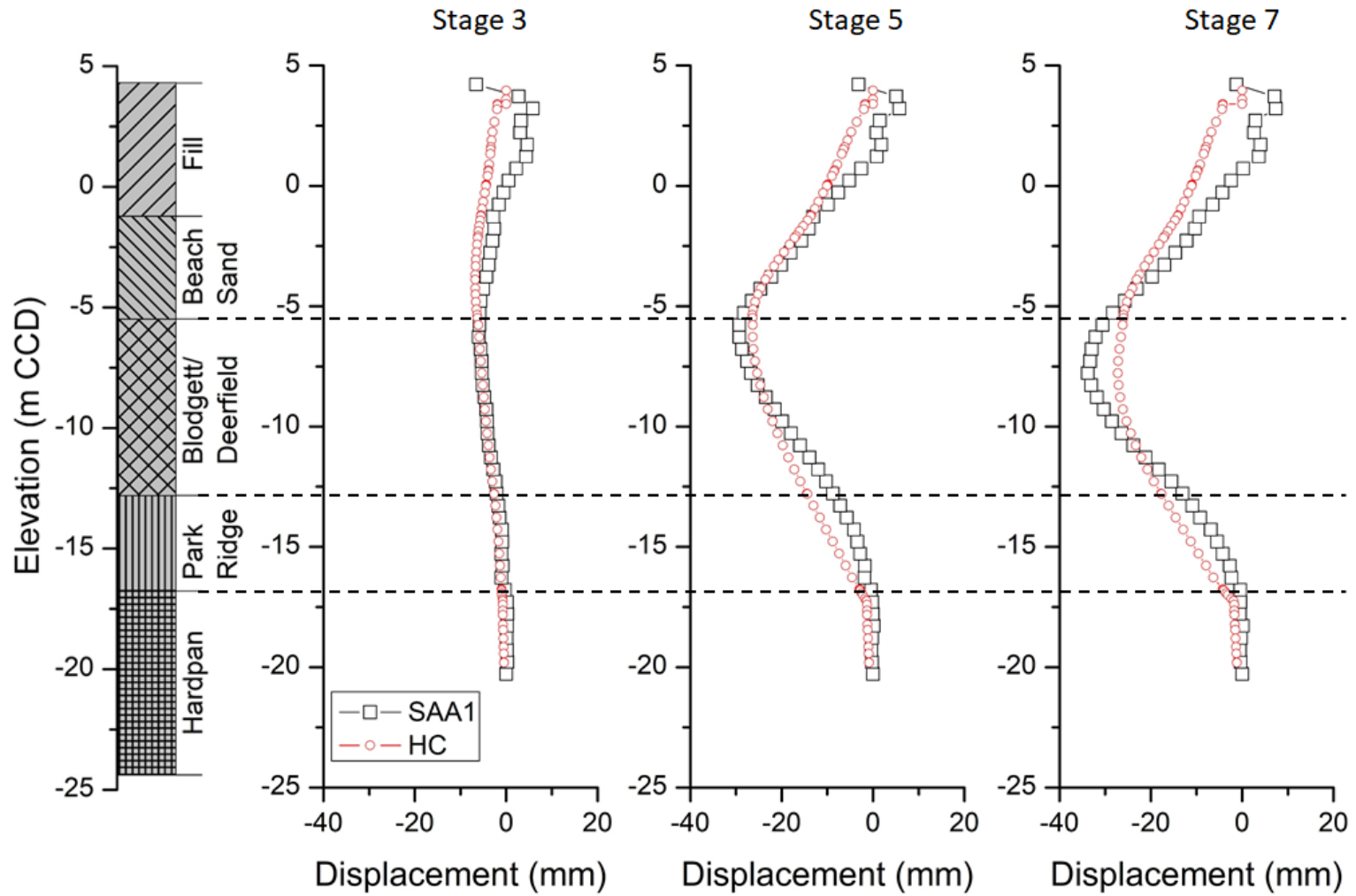


Figure 4.7 Computations of lateral deformation using initial HC parameters

4.3 Inverse Analysis

Optimization is conducted with inverse analysis based on a gradient method. Herein, it is accomplished by coupling the optimization toolbox in MATLAB with the finite element code PLAXIS. A program, written in PYTHON (Appendix), is used to transfer data between PLAXIS and MATLAB. A Gauss-Newton method modified by the addition of damping and Marquardt parameters is used to find a best fit between the computed and measured values (Finno and Calvello 2005, Rechea 2006).

Optimizations were performed in the Blodgett/Deerfield and Park Ridge layers because of the relatively large deformation observed in those layers. Three separate optimizations were carried out using the selected field measurements: (1) SAA-1 at Stage 3; (2) SAA-1 at Stages 3 and 5; (3) SAA-1 at Stages 3, 5 and 7.

4.3.1 Parameter Selection for Optimization

For an optimization to be effectively carried out, the number of parameters optimized for each of the soil models must be constrained. Sensitivity and correlation analyses of the HS model were carried out previously by Finno and Calvello (2005) and Rechea (2006). Following the recommendations of Finno and Calvello (2005), the HS model parameters chosen for optimization are the reference values of the primary loading stiffness, E_{50}^{ref} , in the Blodgett/Deerfield and Park Ridge layers. Other two reference stiffness values, E_{oed}^{ref} (tangent stiffness for primary oedometer loading), and E_{ur}^{ref} (unloading/reloading stiffness) were also indirectly optimized with

$$E_{oed}^{ref} = 0.7 \cdot E_{50}^{ref} \text{ and } E_{ur}^{ref} = 3.0 \cdot E_{50}^{ref} .$$

Mu and Huang (2016) carried out optimizations of the Block 37 field measurements using the HSS model and proposed that E_{50}^{ref} and $\gamma_{0.7}$ be optimized simultaneously. They selected two parameters that impact the small and large strain behavior to represent the soil response at both small and large strain levels.

Field optimizations for the HC model have not been carried out in the past. Therefore, this section will focus on the sensitivity and correlation analyses of the HC model to select the soil parameters that can be best simultaneously optimized.

4.3.1.1 Sensitivity Analysis

Sensitivity analyses were carried out for all three cases: SAA1Stage3; SAA1Stage3,5; SAA1Stage3,5,7. Soil parameters for the HC model were described in Section 2.5.3 and include λ^* , κ^* , N , φ_c and v_{pp} representing large strain behavior, and A_g , n_g , α_G , α_E , α_v , m_{rat} , R_{max} , β_r and χ representing small strain responses. For the sensitivity analysis, λ^* , κ^* and v_{pp} were considered as candidates for optimization for large strain and R_{max} and χ were considered for small strain responses. These selected parameters primarily govern a soil's deformability as opposed to shear strength. Because soil deformations are small in an excavation project, failure in the affected soil mass is expected to be limited, so deformation parameters are the most important in these types of problems. Among the five parameters considered, one parameter governing small strain, and one governing large strain will be chosen for optimization based on the results of subsequent analysis.

Figure 4.8 shows the computed Composite Scaled Sensitivity (CSS) for various combinations of HC model parameters of the two clay layers for all three optimization cases.

Parameters with larger CSS values indicate higher sensitivities with the measurements used in the optimization. The small strain and large strain parameters for the two clay layers with the largest sensitivities for each optimization stages are shown in Table 4.8.

Table 4.8 Parameters with highest values of CSS based on sensitivity analysis

Optimization Stage	Blodgett/Deerfield		Park Ridge	
	Small strain	Large strain	Small strain	Large strain
SAA1Stage3	χ	κ^*	χ	κ^*
SAA1Stage3,5	R_{\max}	κ^*	R_{\max}	κ^*
SAA1Stage3,5,7	R_{\max}	v_{pp}	R_{\max}	κ^*

R_{\max} was the most sensitive small strain parameter for most cases. χ was more sensitive than R_{\max} for cases considering only Stage 3. Among the large strain parameters, κ^* was the most sensitive parameter for all cases except for the Blodgett/Deerfield layer at SAA1Stage3,5,7. v_{pp} was the second sensitive parameter, indicating slightly larger sensitivities than the λ^* parameter. It makes sense that κ^* was the most sensitive large strain parameter in these results because excavations are primarily unloading phenomena and κ^* represents the unloading/recompression response.

It is also important to note that the small strain parameters have a much larger CSS than the large strain parameters for all cases in Figure 4.8. This is another reason why the soil model used for predicting excavation-induced movements should include small strain stiffness capabilities.

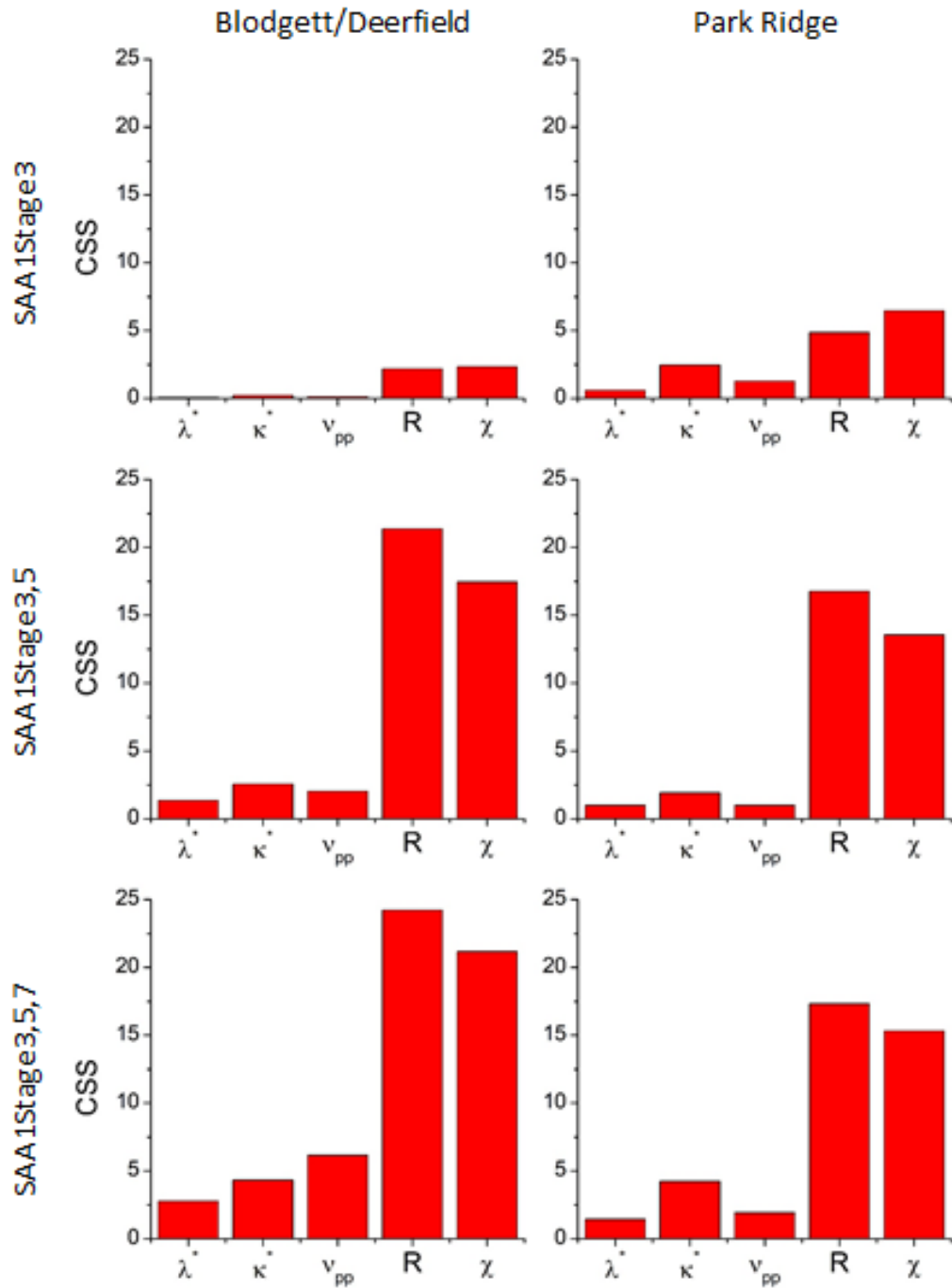


Figure 4.8 CSS for Blodgett/Deerfield and Park Ridge for all optimization stages

4.3.1.2 Correlation Analysis

In inverse analysis, parameters cannot be simultaneously optimized when they are closely related to each other. To assess the correlations between the considered HC model parameters, correlation analyses were carried out for the two clay layers for all optimization stages as shown in Figures 4.9 to 4.14. Each figure describes the correlation between two parameters for a given optimization case. Note that the correlation between a parameter and itself is 1.0. As previously discussed in Chapter 2, absolute values of the Parameter Correlation Coefficient (PCC) above 0.9 may indicate problems when trying to optimize the two parameters.

Large correlation coefficient values over 0.9 are observed for a number of cases. For example, the correlation analysis of Blodgett/Deerfield at SAA1Stage3,5,7 indicates that the two large strain parameters λ^* and v_{pp} are highly correlated to each other. The two small strain parameters, R_{max} and χ , also show high correlations. Correlations between a large strain parameter and a small strain parameter (e.g. R_{max} and λ^* , R_{max} and κ^* , R_{max} and v_{pp}) are lower than 0.9, indicating that the two considered parameters have low correlations and thus can be simultaneously optimized.

The majority of sensitivity analyses indicated R_{max} and κ^* to be the optimized parameters in Section 4.3.1.1. However, values of κ^* can be reasonably evaluated by results of conventional oedometer tests and did not need to be additionally altered with an optimization process. Furthermore, v_{pp} had the second largest CSS of the large strain parameters, therefore was considered as the large strain parameter to be optimized. Correlation coefficients, PCC, for the two parameters, R_{max} and v_{pp} , were lower than 0.9 in all cases except for the Blodgett/Deerfield at SAA1Stage3,5, allowing the two parameters to generally be simultaneously optimized.

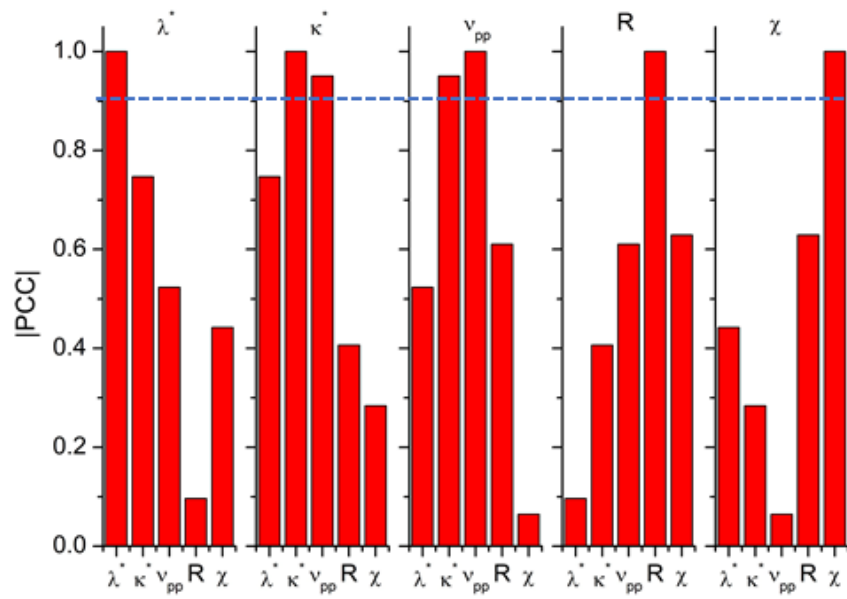


Figure 4.9 PCC for Blodgett/Deerfield at SAA1Stage3

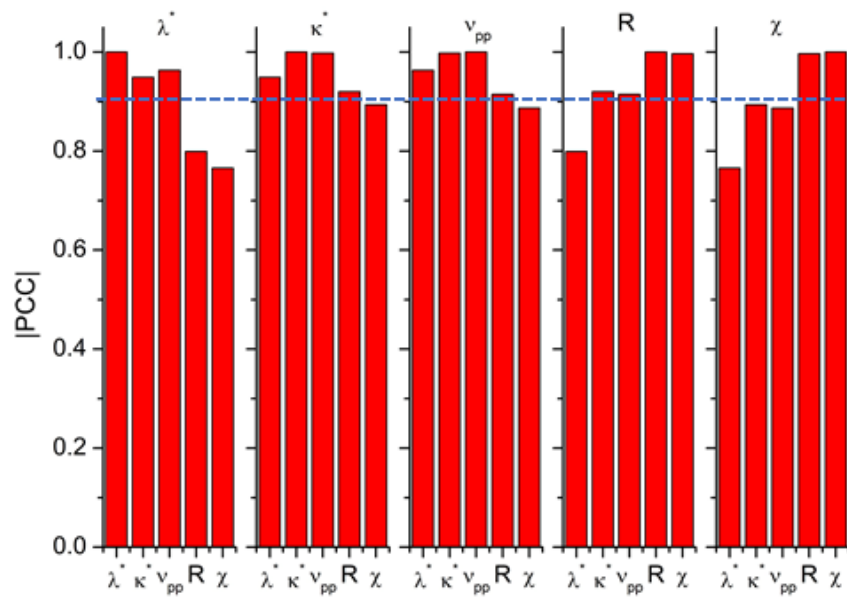


Figure 4.10 PCC for Blodgett/Deerfield at SAA1Stage3,5

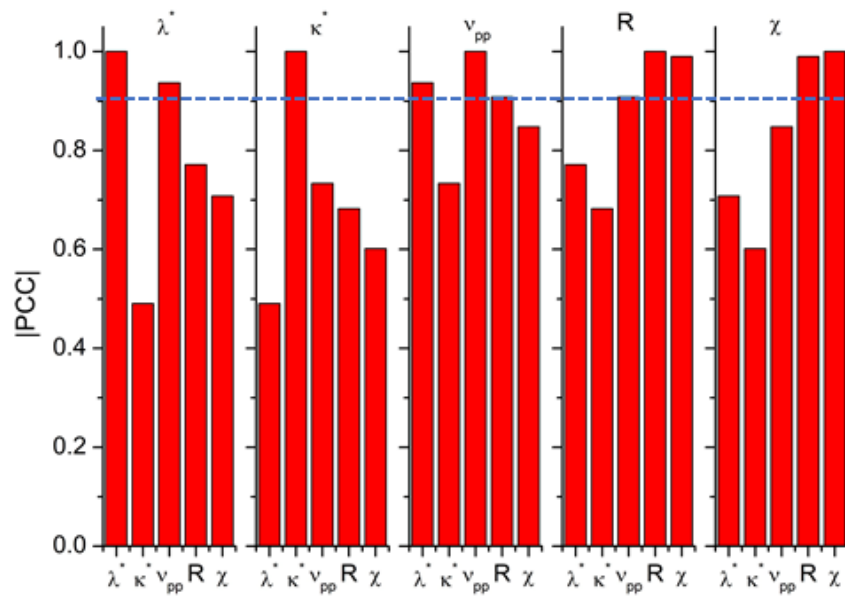


Figure 4.11 PCC for Blodgett/Deerfield at SAA1Stage3,5,7

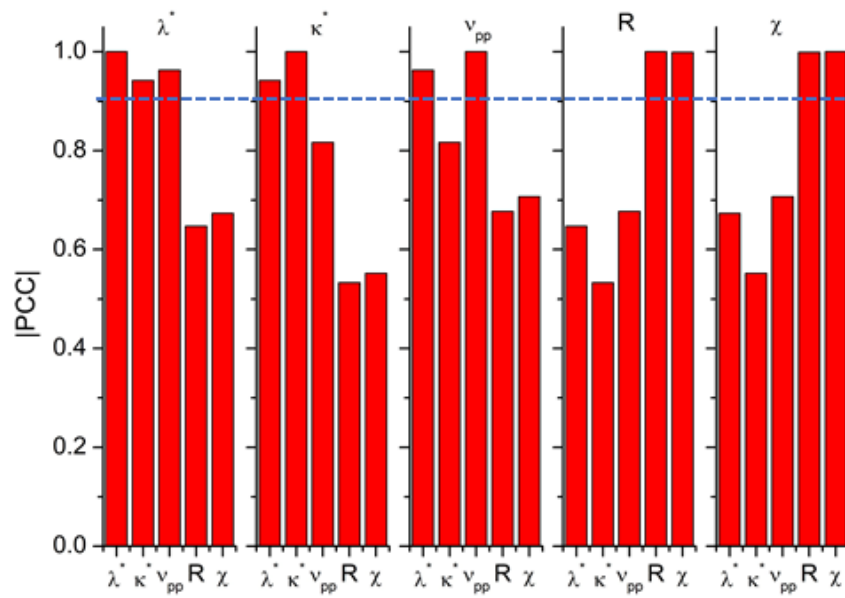


Figure 4.12 PCC for Park Ridge at SAA1Stage3

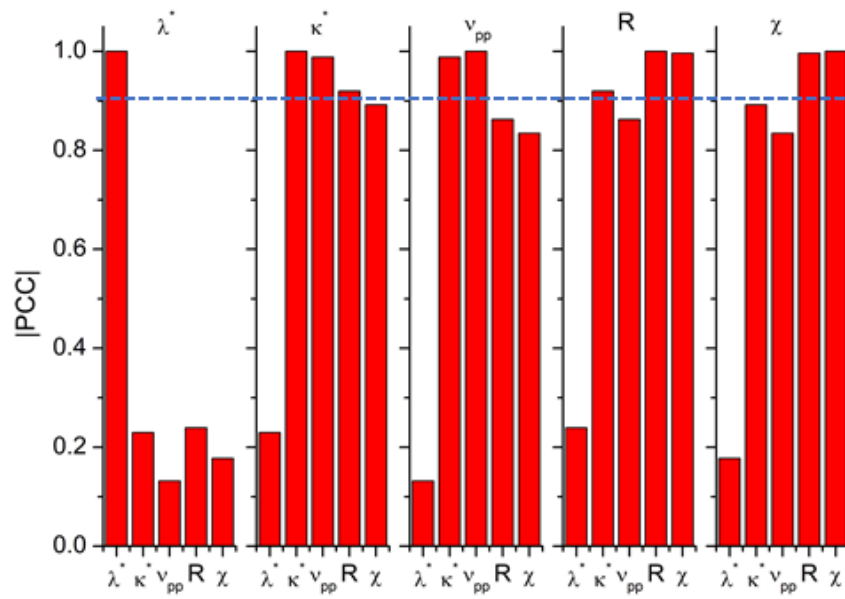


Figure 4.13 PCC for Park Ridge at SAA1Stage3,5

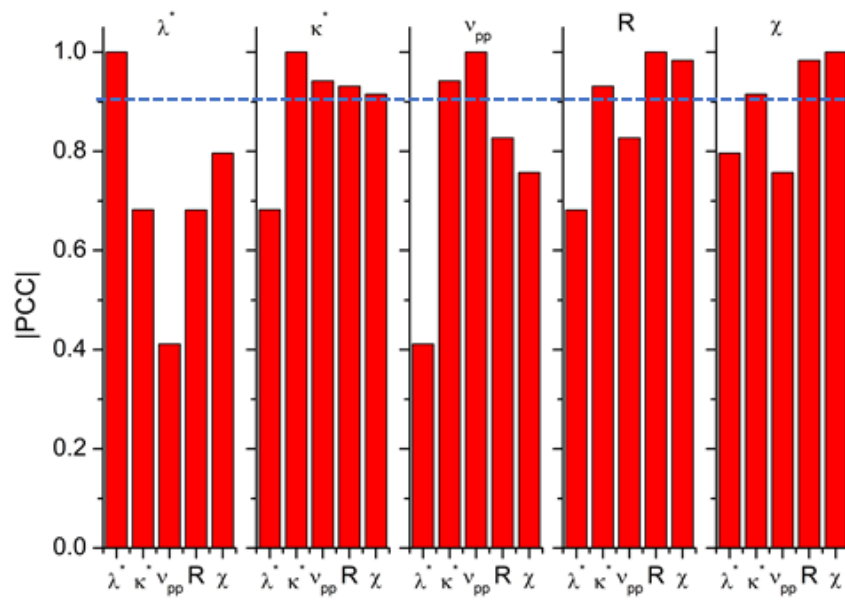


Figure 4.14 PCC for Park Ridge at SAA1Stage3,5,7

4.3.2 Optimized Soil Parameters

The question arises whether it is possible to reasonably optimize the soil parameters at early stages of excavations so latter stages can be accurately predicted. If this is the case, the value of the optimized parameters will not change in the latter stages of excavation. The optimized soil parameters for all three considered soil models will be analyzed in this section. The computed deformations using the optimized parameters will be later discussed in Section 4.3.3.

4.3.2.1 HS Model

Optimized values of E_{50}^{ref} for the HS model for all three cases are shown in Table 4.9.

Table 4.9 Optimized E_{50}^{ref} values for HS model

	Blodgett/Deerfield		Park Ridge	
	Shear strain (%)	E_{50}^{ref} (kPa)	Shear strain (%)	E_{50}^{ref} (kPa)
Initial	-	12,500	-	150,000
SAA1Stage3	0.07	33,300	0.05	211,600
SAA1Stage3,5	0.26	15,100	0.12	227,900
SAA1Stage3,5,7	0.30	12,800	0.20	195,400

Because the HS model does not include small strain capabilities, the ranges of shear strains behind the wall at the optimized stages were computed to correlate the E_{50}^{ref} values with shear strain level. The shear strains corresponding to Stages 3, 5 and 7 of the SQBRC excavation were obtained from results of the PLAXIS simulations for each of the stages as in Figures 4.15 to 4.17.

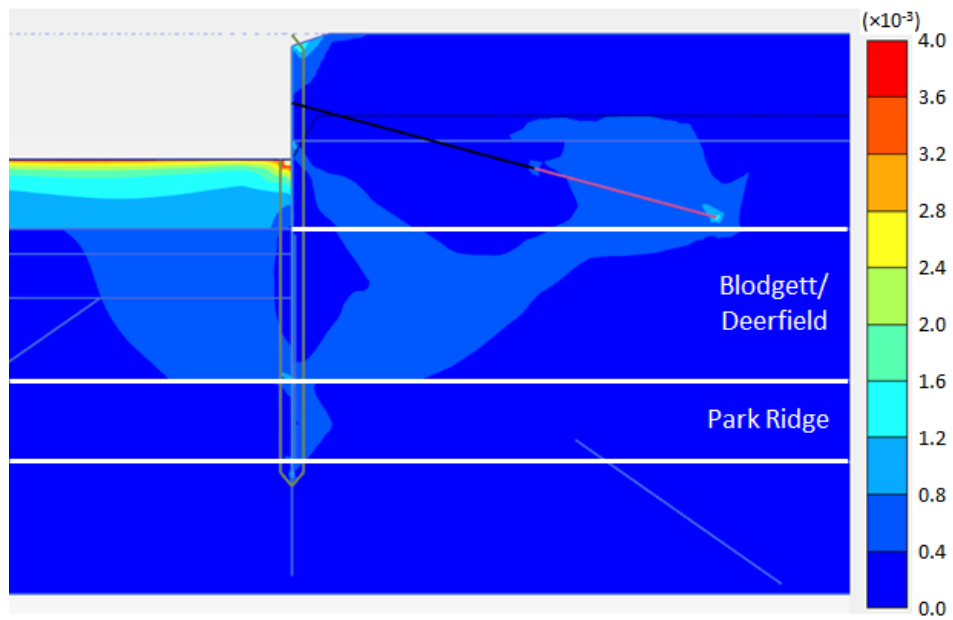


Figure 4.15 Shear strains corresponding to Stage 3

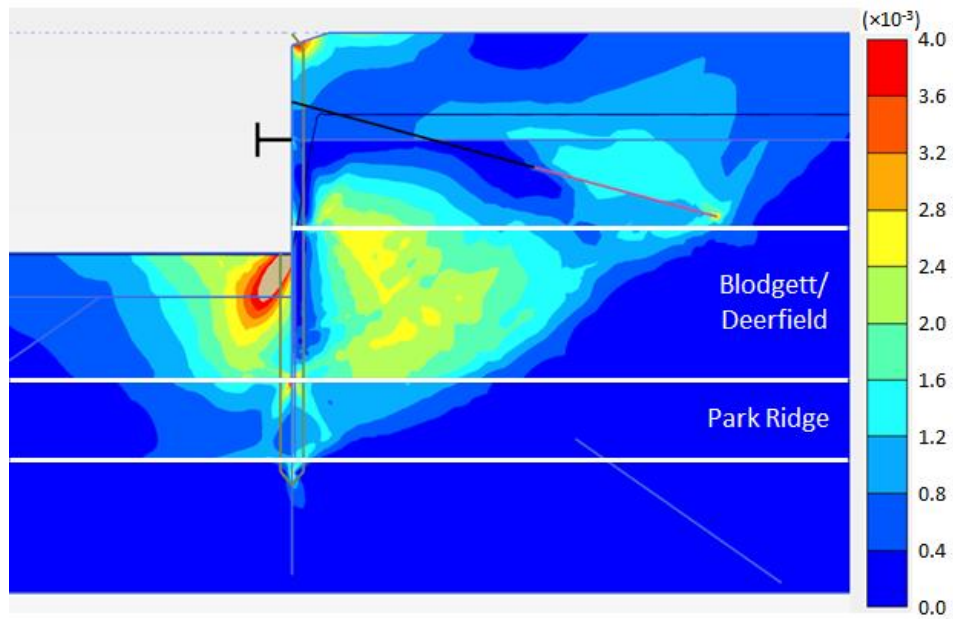


Figure 4.16 Shear strains corresponding to Stage 5

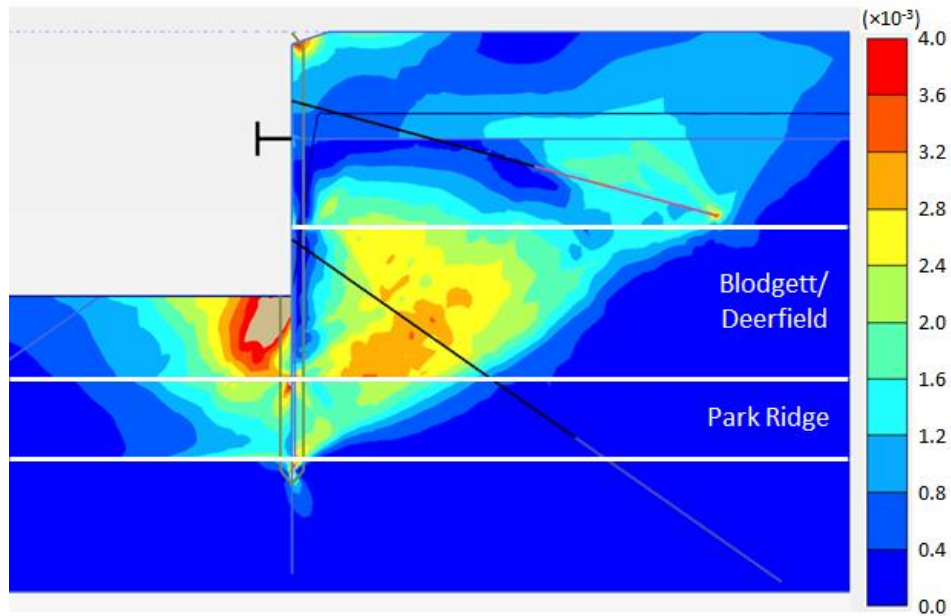


Figure 4.17 Shear strains corresponding to Stage 7

The shear strain plotted in these figures refers to the deviatoric strain invariant ε_q defined as:

$$\varepsilon_q = \sqrt{\frac{2}{3} \left[\left(\varepsilon_{xx} - \frac{\varepsilon_v}{3} \right)^2 + \left(\varepsilon_{yy} - \frac{\varepsilon_v}{3} \right)^2 + \left(\varepsilon_{zz} - \frac{\varepsilon_v}{3} \right)^2 + \frac{1}{2} (\gamma_{xy}^2 + \gamma_{yz}^2 + \gamma_{zx}^2) \right]} \quad (4.6)$$

Shear strains are concentrated in the Blodgett/Deerfield layer at all three stages considered. The predominant maximum shear strain levels behind the wall ranged to 0.07, 0.26, 0.30 % for Stages 3, 5 and 7, respectively. Predominant maximum strain levels in the Park Ridge were slightly lower.

The optimized E_{50}^{ref} from SAA1Stage3 has a large value due to its very low shear strain at Stage 3. This optimized parameter decreased sharply when the lateral movements from Stage 5 were included in the analysis. Stage 5 is when the excavation was made into the soft to medium

stiff clay layer (Blodgett/Deerfield), and large incremental deformations were observed with a correspondingly larger range of strains. The value of E_{50}^{ref} from SAA1Stage3,5,7 was slightly smaller when all three stages were considered in the analysis, a consequence of the larger strain level within the layer.

Optimized E_{50}^{ref} parameters from SQBRC are compared with other optimized parameters from excavations in Chicago as shown in Figure 4.18. As was shown by Rechea (2006), the overall trend optimized E_{50}^{ref} parameters from case studies in Chicago shows a decrease in value with increasing shear strain, and the SQBRC data fit this trend as well. Figure 4.19 shows the decrease in E_{50}^{ref} with maximum lateral deformation at the wall. An increase in the maximum lateral deformations also show a trend of decrease in E_{50}^{ref} .

Optimized E_{50}^{ref} for Park Ridge did not show a trend with increasing shear strain but consistently indicated large stiffness values due to the small deformation levels (maximum deformation of 13 mm) observed in the stiff layer.

Because E_{50}^{ref} changes at all excavation stages, these results suggest that the HS model will not be able to make accurate predictions of lateral wall deformation based on observations of early stages of excavation where shear strains are relatively small. To accurately estimate the deformation at the end of excavation, one must have a reasonable estimation of the expected shear strain level when selecting parameters. To make proper predictions of later excavation stages with different shear strain levels, a soil model that represents both small and large strain levels through the use of a single set of model parameters must be employed.

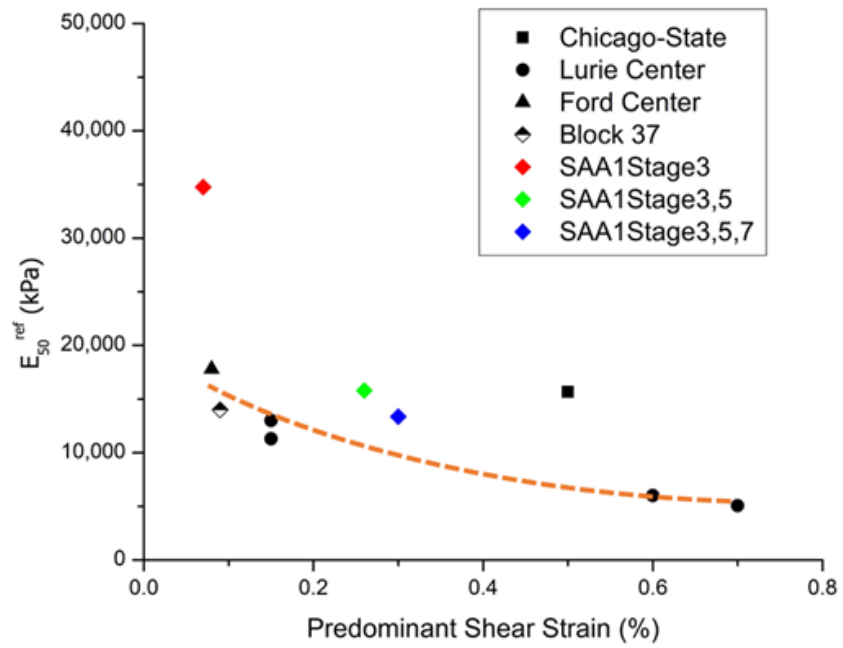


Figure 4.18 Optimized E_{50}^{ref} values of Blodgett/Deerfield with predominant shear strain

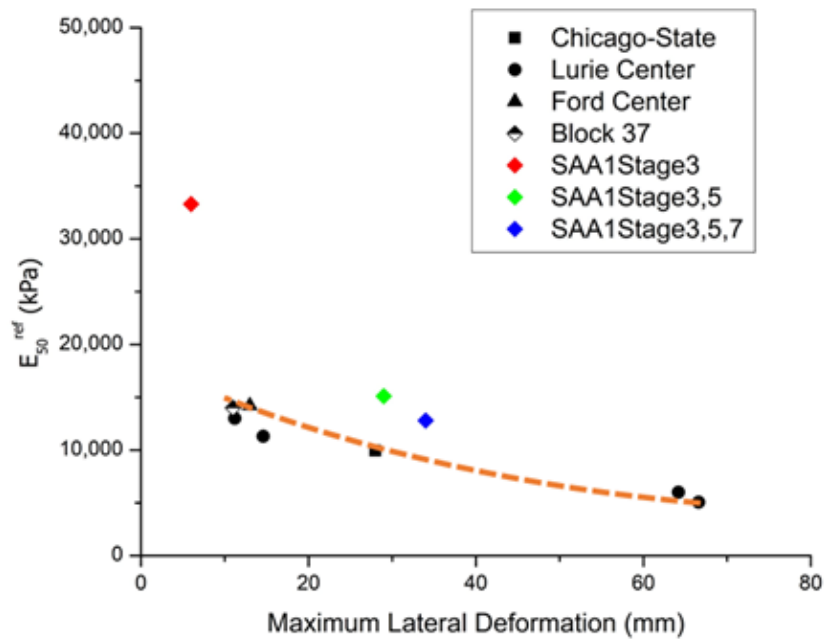


Figure 4.19 Optimized E_{50}^{ref} values of Blodgett/Deerfield with maximum lateral deformation

4.3.2.2 HSS Model

Optimized values of E_{50}^{ref} and $\gamma_{0.7}$ for the HSS model for all three optimization cases are shown in Table 4.10. The change in optimized parameters between optimizations at SAA1Stage3 and SAA1Stage3,5 are significant, whereas the changes are not that significant when comparing the parameters between optimizations at SAA1Stage3,5 and SAA1Stage3,5,7. Like the HS model, the HSS model parameters indicated similar optimized parameter values once the large incremental deformations of Stage 5 were considered in the optimization. It can be concluded that the HSS model parameters were reasonably estimated at SAA1Stage3,5 where the considered shear strain is a range of up to 0.26 %. Optimized parameters for Park Ridge showed a similar trend, reasonably estimated when a shear strain range of 0.12 % was considered at SAA1Stage3,5.

Table 4.10 Optimized E_{50}^{ref} and $\gamma_{0.7}$ values for HSS model

	Blodgett/ Deerfield			Park Ridge		
	Shear strain (%)	E_{50}^{ref} (kPa)	$\gamma_{0.7}$	Shear strain (%)	E_{50}^{ref} (kPa)	$\gamma_{0.7}$
Initial	-	12,500	1.00×10^{-04}	-	35,000	1.00×10^{-04}
SAA1Stage3	0.07	28,000	9.62×10^{-05}	0.05	11,000	6.36×10^{-02}
SAA1Stage3,5	0.26	7,700	7.97×10^{-05}	0.12	40,300	4.00×10^{-04}
SAA1Stage3,5,7	0.30	8,900	7.20×10^{-05}	0.20	50,800	2.26×10^{-04}

Figures 4.20 and 4.21 show the decrease in reference shear stiffness with shear strain for Blodgett/Deerfield and Park Ridge, respectively, using the optimized HSS model parameters.

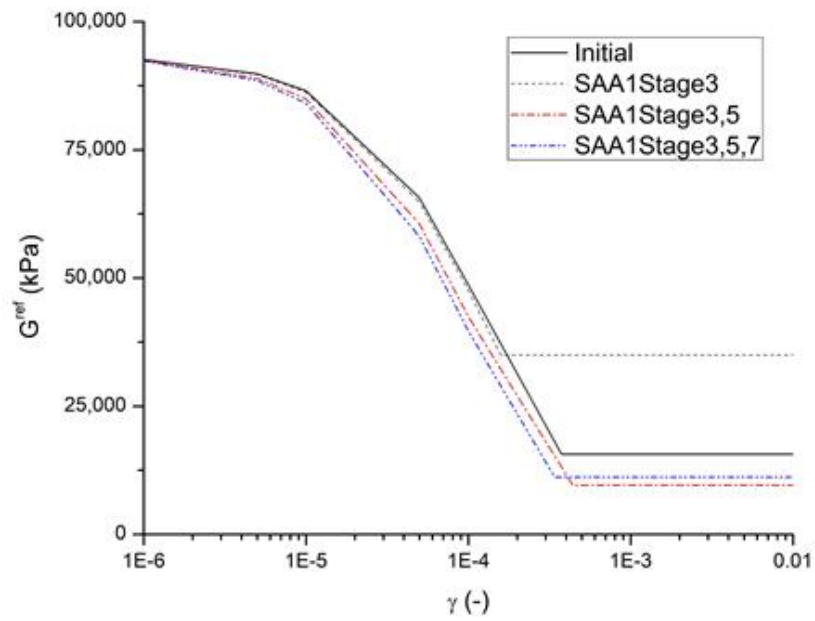


Figure 4.20 G^{ref} with shear strain using Blodgett/Deerfield optimized parameters

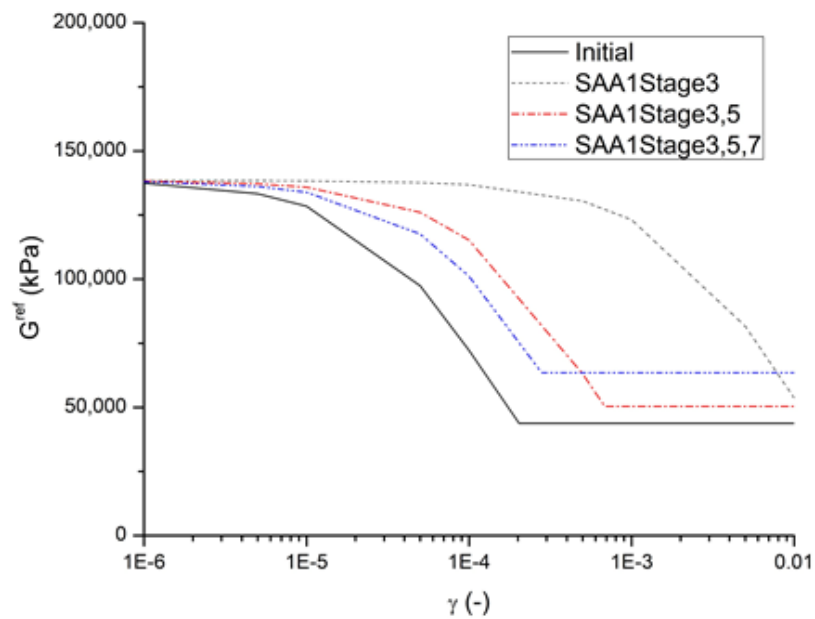


Figure 4.21 G^{ref} with shear strain using Park Ridge optimized parameters

Optimized parameters using SAA1Stage3 dramatically differ from the initial parameters. SAA1Stage3,5 and SAA1Stage3,5,7 optimizations moved the soil parameters back relatively closer to the initial parameters. Because the deformation level was used in the optimization for SAA1Stage3 was too small, this led to a very stiff response. This resulted in an E_{50}^{ref} value that is too large (for Blodgett/Deerfield), or $\gamma_{0.7}$ value that is too large (for Park Ridge). These soil parameters were unreasonable for predictions of later stages with larger deformation levels. Considering that reasonable estimates of optimized parameters for the two clay layers were both made at SAA1Stage3,5, it is concluded that the HSS model needs observations made at shear strains larger than approximately 0.10 % for proper optimizations. Because the parameters optimized from SAA1Stage3 were not considered reasonable, only the optimizations from SAA1Stage3,5 and SAA1Stage3,5,7 will be used in the following section.

Table 4.11 compares the optimized HS and HSS parameters for the SQBRC excavation.

Table 4.11 Optimized HS and HSS model parameters

		HS model	HSS model	
		E_{50}^{ref} (kPa)	E_{50}^{ref} (kPa)	$\gamma_{0.7}$
Blodgett/Deerfield	SAA1Stage3,5	15,100	7,700	8.0×10^{-05}
	SAA1Stage3,5,7	12,800	8,900	7.2×10^{-05}
Park Ridge	SAA1Stage3,5	227,900	40,300	4.0×10^{-04}
	SAA1Stage3,5,7	195,400	50,800	2.3×10^{-04}

The table shows that E_{50}^{ref} for the HSS model is lower than E_{50}^{ref} for the HS model. This is expected because the variance of E_{50}^{ref} with shear strain level is not considered in the HS model, and a higher E_{50}^{ref} value is required in the HS model to account for the small-strain stiffness.

- **Comparison with optimizations of Block 37 excavation**

Mu et al. (2015) carried out the optimization of HSS model parameters for the Block 37 field measurements. Optimized parameters are shown and compared with the SQBRC optimization in Table 4.12.

Table 4.12 Comparison of optimized HSS model parameters from SQBRC and Block 37

	SQBRC			Block 37		
	E_{50}^{ref} (kPa)	$\gamma_{0.7}$	G_0 (kPa)	E_{50}^{ref} (kPa)	$\gamma_{0.7}$	G_0 (kPa)
Blodgett	7,700 (SAA1Stage3,5)	8.0×10^{-05} (SAA1Stage3,5)	93,300	8,200	7.6×10^{-05}	78,000
Deerfield	8,900 (SAA1Stage3,5,7)	7.2×10^{-05} (SAA1Stage3,5,7)		7,600	6.6×10^{-05}	95,000
Park Ridge	40,300 (SAA1Stage3,5)	4.0×10^{-04} (SAA1Stage3,5)	138,500	12,700	7.2×10^{-05}	83,400
	50,800 (SAA1Stage3,5,7)	2.3×10^{-04} (SAA1Stage3,5,7)				

G_0 values were similar for the Blodgett/Deerfield layer in the SQBRC and Block 37 cases. Therefore, a straightforward comparison could be made for the optimized parameters in the soft to medium stiff clay layer. HSS model parameters for the Blodgett/Deerfield obtained from SQBRC were within the parameter range of optimized parameters carried out from Block 37 field measurements, lending credence to the parameters as being representative of this stratum at the two sites located about 1 mile apart in the downtown area of Chicago.

The Park Ridge layer for both sites showed G_0 values and optimized HSS model parameters that indicate a significantly larger stiffness compared to the Blodgett/Deerfield, resulting in a smaller lateral deformation computation.

4.3.2.3 HC Model

Optimized parameters of the HC model for all three optimization cases are shown in Table 4.13.

Table 4.13 Optimized parameters for HC model

	Blodgett/Deerfield			Park Ridge		
	Shear strain (%)	v_{pp}	R_{max}	Shear strain (%)	v_{pp}	R_{max}
Initial	-	0.15	5.0×10^{-05}	-	0.15	2.4×10^{-05}
SAA1Stage3	0.07	0.51	5.5×10^{-05}	0.05	0.12	7.0×10^{-05}
SAA1Stage3,5	0.26	0.15	3.9×10^{-05}	0.12	0.09	4.5×10^{-05}
SAA1Stage3,5,7	0.30	0.18	3.9×10^{-05}	0.20	0.19	3.9×10^{-05}

Optimization using SAA1Stage3 results in the Blodgett/Deerfield soil parameters to dramatically differ from the initial parameters. SAA1Stage3,5 and SAA1Stage3,5,7 optimizations moved the Blodgett/Deerfield soil parameters back relatively closer to the initial parameters. Optimized parameters for the Park Ridge stratum did not show such a trend with optimization stage due to the small deformation levels used in the optimization.

To assess whether the optimized parameters were reasonable, ranges of v_{pp} values for different clays reported by Masin (2011) were used as reference (Table 4.14): 0.08 to 0.38. The

range of R_{\max} values for various clays were also reported by Masin (2011) as 2×10^{-05} to 1×10^{-04} (Table 4.15).

Table 4.14 Estimates of HC model large-strain parameters for various clays

	φ_c (°)	λ^*	κ^*	N	v_{pp}
Brno clay	22.0	0.128	0.015	1.51	0.33
London clay	21.9	0.095	0.015	1.19	0.10
Kaolin	27.5	0.065	0.010	0.92	0.35
Dortmund clay	27.9	0.057	0.008	0.75	0.38
Weald clay	24.0	0.059	0.018	0.80	0.30
Koper silt	33.0	0.103	0.015	1.31	0.28
Fujinomori clay	34.0	0.045	0.011	0.89	0.36
Pisa clay	21.9	0.140	0.010	1.56	0.31
Beaucaire clay	33.0	0.060	0.010	0.85	0.21
Trmice clay	18.7	0.090	0.010	1.09	0.09
min.	18.7	0.045	0.010	0.75	0.09
Max.	34.0	0.140	0.020	1.51	0.38
Blodgett/Deerfield	33.0	0.06	0.012	0.76	0.15 (SAA1Stage3,5)
					0.18 (SAA1Stage3,5,7)
Park Ridge	35.0	0.05	0.012	0.64	0.09 (SAA1Stage3,5)
					0.19 (SAA1Stage3,5,7)

Table 4.15 Estimates of HC model intergranular strain parameters for various clays

	β	χ	R_{\max}
London clay (reconstituted)	0.20	6.0	1.0×10^{-04}
London clay (natural)	0.10	1.0	5.0×10^{-05}
Brno clay	0.20	0.8	1.0×10^{-04}
Koper silty clay	0.09	0.7	2.0×10^{-05}
min.	0.09	0.7	2.0×10^{-05}
Max.	0.20	6.0	1.0×10^{-04}
Blodgett/Deerfield	0.18	1.3	3.9×10^{-05} (SAA1Stage3,5)
			3.9×10^{-05} (SAA1Stage3,5,7)
Park Ridge	0.18	1.3	4.5×10^{-05} (SAA1Stage3,5)
			3.9×10^{-05} (SAA1Stage3,5,7)

Optimizations using data from SAA1Stage3 did not provide v_{pp} parameter values for Blodgett/Deerfield within the reported range of various clays. This is due to the measurements of SAA1Stage3 used in the optimizations being too small. R_{max} values were within the expected range for all optimization stages. Because the optimization using SAA1Stage3 did not present reasonable parameter values within the range of various clays, only the optimizations carried out for SAA1Stage3,5 and SAA1Stage3,5,7 will be used for comparison purposes.

It can be observed in Table 4.13 that the parameters for Blodgett/Deerfield do not change significantly after the optimization was made for SAA1Stage3,5. The optimized parameters at SAA1Stage3,5,7 are not significantly different from the parameters from SAA1Stage3,5, as was the case with the HS and HSS models. The R_{max} value did not change between the optimizations of SAA1Stage3,5 and SAA1Stage3,5,7. The v_{pp} value had a slight increase between the optimizations of the two stages. An increase in the v_{pp} value generally indicates a decrease in the shear modulus at large strain (Masin 2015).

Differences in the parameters were observed for the Park Ridge layer between optimizations for SAA1Stage3,5 and SAA1Stage3,5,7. The v_{pp} value increased by a factor larger than 2, and the R_{max} value decreased slightly between the two optimization stages. Changes in the two parameter values indicated a lower stiffness at both small and large strains for SAA1Stage3,5,7 compared to SAA1Stage3,5.

Effects of the parameter changes between the two optimization stages can be observed from Figure 4.22. The figure shows larger computed deformations at both Stages 5 and 7 using the optimized parameters from SAA1Stage3,5,7 compared to the using optimized parameters of SAA1Stage 3,5. This is because the change in optimized parameters from SAA1Stage3,5 to

SAA1Stage3,5,7 indicated decreases in stiffness values for both clay layers. However, the difference in lateral deformation level using the two sets of optimized parameters are insignificant (1 mm for Stage 5 and 3 mm for Stage 7). Although optimized parameters for Park Ridge showed significant changes in the v_{pp} parameter between the two optimization stages, this had an insignificant effect on the lateral deformation computations in the Park Ridge stratum.

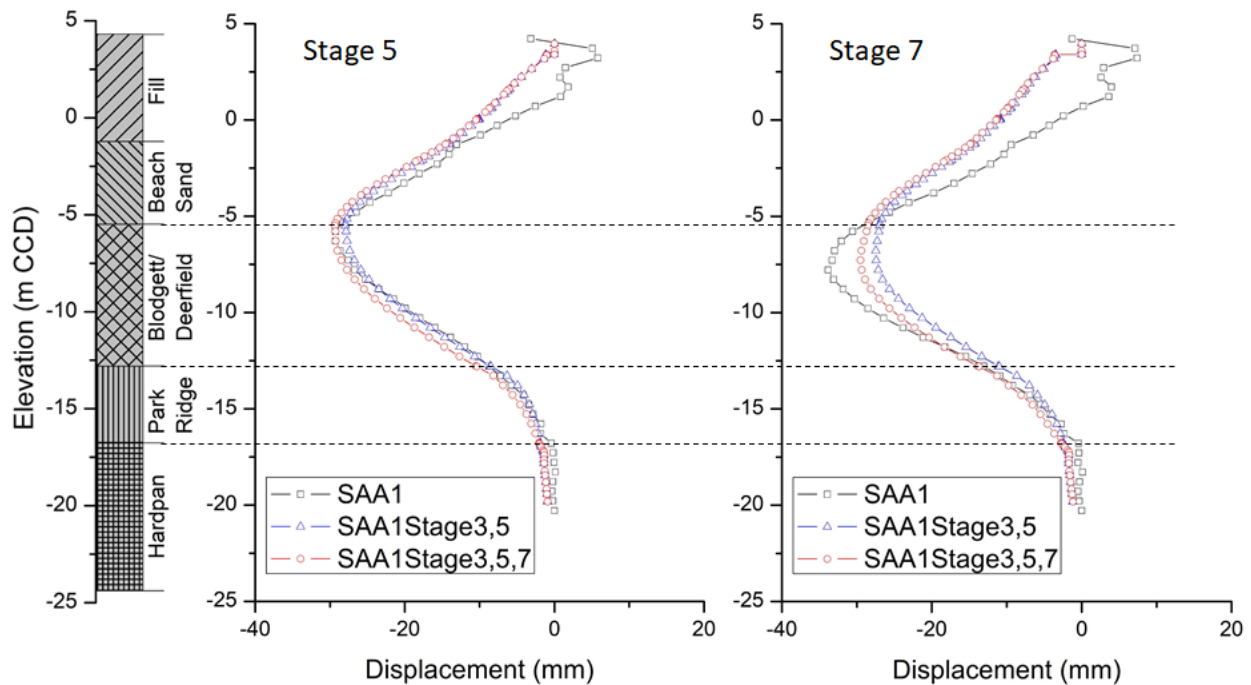


Figure 4.22 Measured and computed deformations using different optimized parameters

The response of lateral deformation in the Park Ridge layer is mainly affected by the R_{max} parameter due to the small deformation levels observed in the stratum. This was also shown in Figure 4.8 where the sensitivities of the small strain parameters were significantly larger than those

for the large strain parameters. When more weight is given to the R_{\max} parameter than the v_{pp} parameter, it is concluded that the most influential parameter of the Park Ridge layer, R_{\max} , is reasonably estimated at SAA1Stage3,5. Considering that reasonable estimates of Blodgett/Deerfield and Park Ridge parameters were made using the measurements at SAA1Stage3,5, it is concluded that HC model needs observations made at shear strains larger than approximately 0.10 % for proper optimizations, as was for HSS model.

4.3.3 Comparison of Computed Lateral Deformations

Computed lateral deformations based on the optimized parameters based on data from Stages 3, 5 and 7 are presented in this section. The “fit” between computations and measurements are quantified with the Root Mean Squared Error (RMSE). The lateral deformation characteristics for all three considered soil models are visually shown, along with an analysis of the soil models’ prediction capabilities.

4.3.3.1 Evaluation of Fit

Fits for the three soil models can be visually observed in Figures 4.23 to 4.25. Lateral deformations of the wall computed based on the optimized parameters for all three soil models are shown. Red boxes on the figure indicate which stages were optimized to produce the results. Plots outside the red boxes indicate the “predictions” made by the optimized parameters.

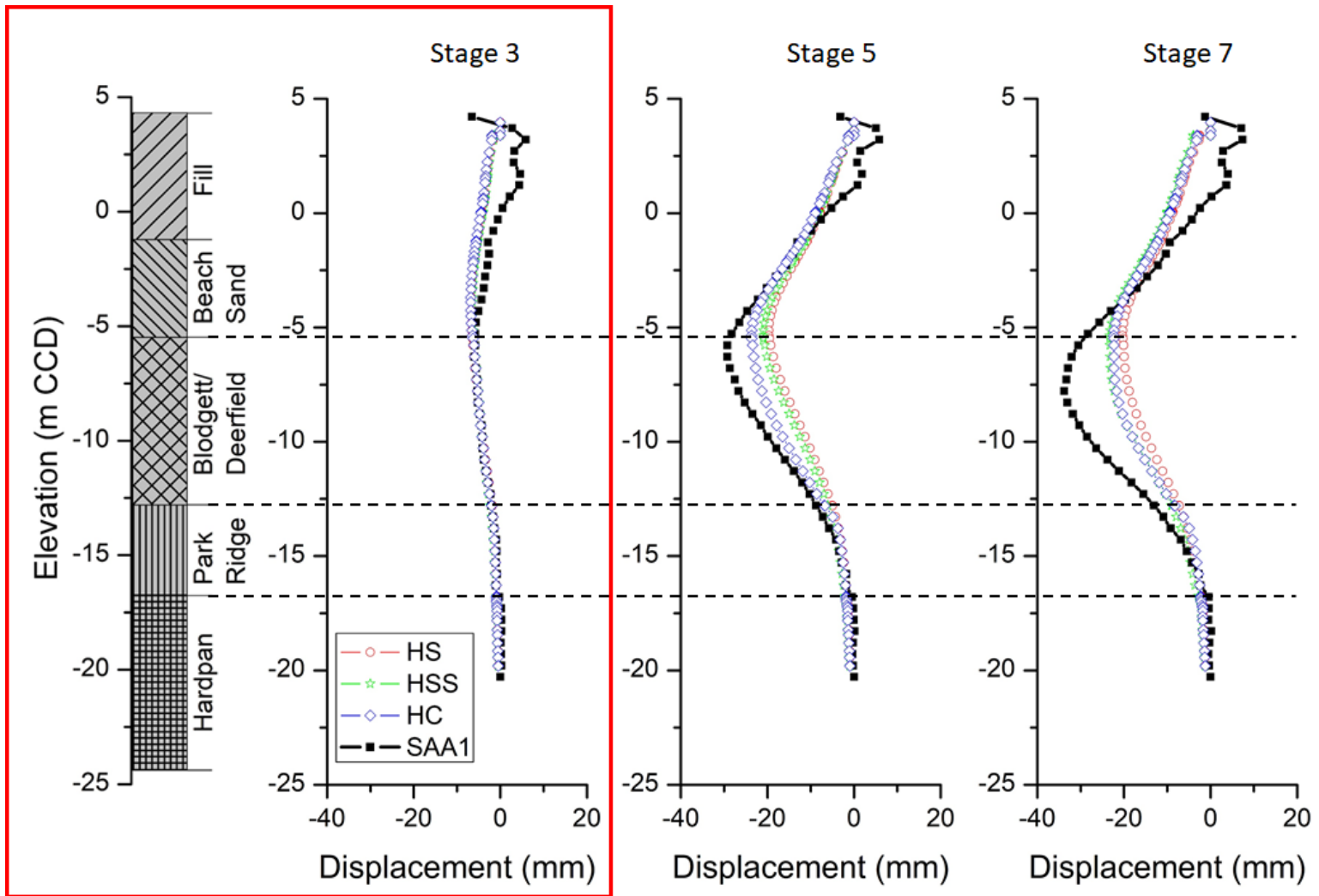


Figure 4.23 Deformations based on SAA1Stage3 optimization

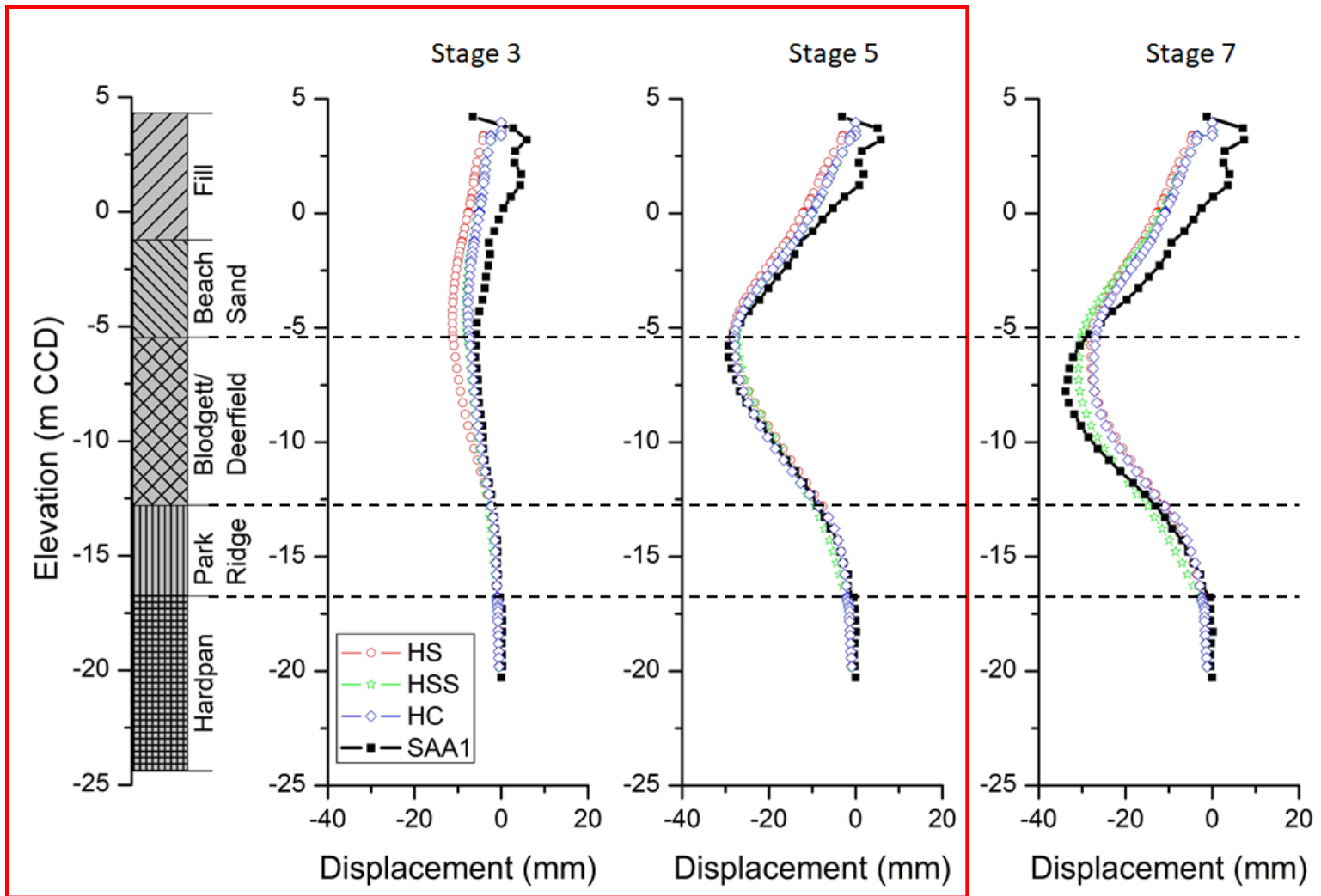


Figure 4.24 Deformations based on SAA1Stage3,5 optimization

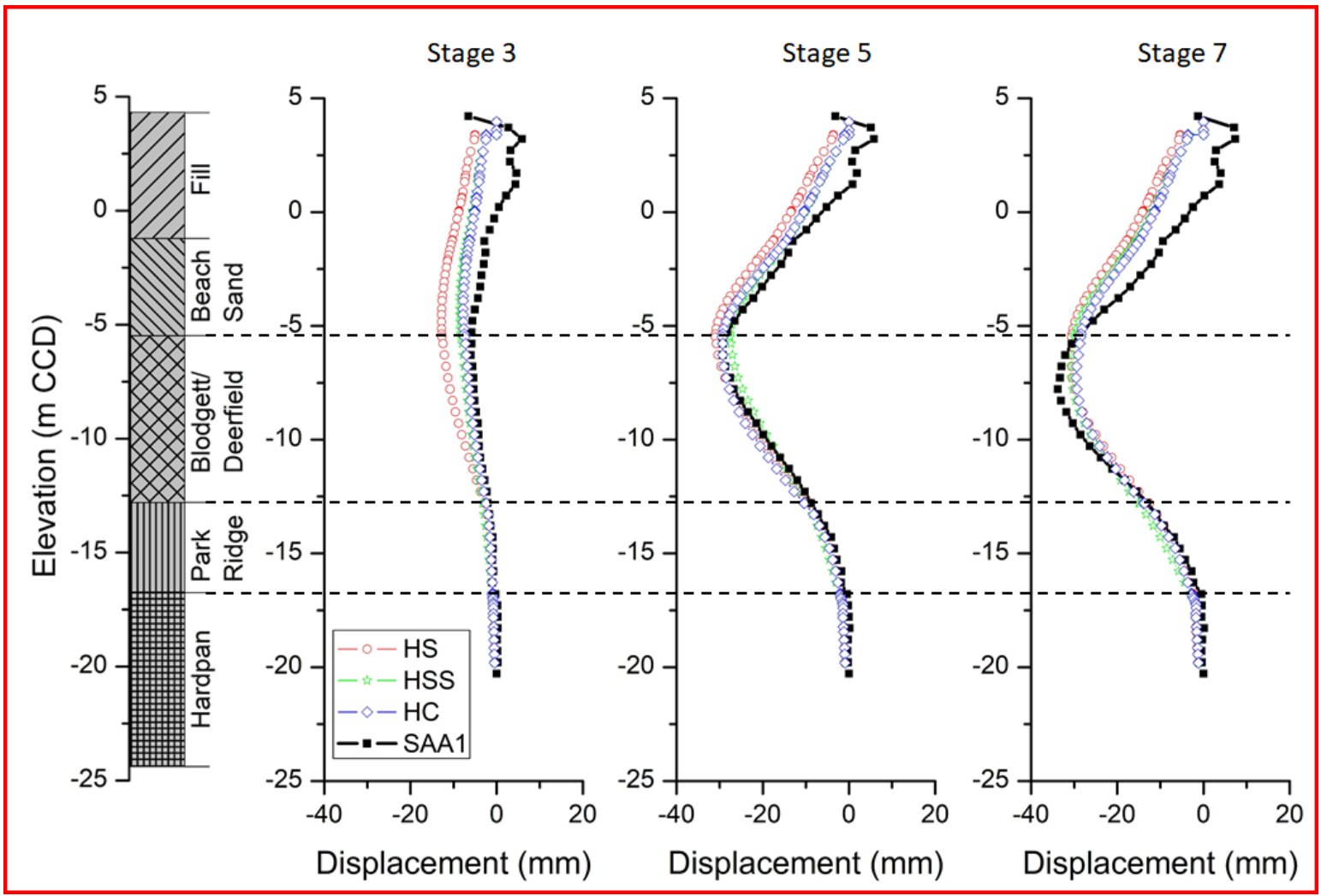


Figure 4.25 Deformations based on SAA1Stage3,5,7 optimization

To quantify the quality of fit between the measured and computed lateral wall movements, the Root Mean Squared Error (RMSE) was calculated using the following equation:

$$\text{RMSE} = \sqrt{\frac{1}{n} \sum_{j=1}^n (y_j - \hat{y}_j)^2} \quad (4.7)$$

where y_j refers to the observed value for Stage j ; \hat{y}_j indicates the predicted value. The RMSE values for all optimization cases were calculated as in Table 4.16. The RMSE of SAA1Stage3 for all three models indicate computations that are very close to the measurements after the optimization (Figure 4.23).

Table 4.16 RMSE values for computations using optimized parameters

Optimization stage	HS Model	HSS Model	HC Model
SAA1Stage3	0.22	0.28	0.19
SAA1Stage3,5	2.10	1.31	0.72
SAA1Stage3,5,7	2.56	1.84	1.79

Comparing the RMSE values for SAA1Stage3,5, the HSS model has a lower RMSE value than the HS model, indicating that the HSS model computations provide better fits with the measurements. The HC model also shows a value that is lower than both the HS and HSS models, quantitatively indicating that the HC model provides a better fit compared to the other two models. This can also be observed in Figure 4.24. RMSE values for SAA1Stage3,5 indicated that the HC model provided the best fit with the measurements of Stages 3 and 5, but this does not necessarily mean that the HC model generates the closest predictions of later stages (Stage 7) using the optimized parameters.

RMSE values of optimizations carried out with SAA1Stage3,5,7 showed the same trends as the SAA1Stage3,5 case. The HC model indicated the closest fit between the computations and measurements, followed by the HSS model. This trend is also shown in Figure 4.25.

4.3.3.2 Prediction Capabilities

To evaluate the prediction capabilities of the three soil models, predictions of Stage 5 based on optimized parameters of SAA1Stage3 and predictions of Stage 7 based on optimized parameters of SAA1Stage3,5 are compared. The predictions of the three soil models will be quantitatively compared with calculations of RMSE.

- HS Model

Computations based on optimizations of SAA1Stage3 and SAA1Stage3,5 are compared as in Figure 4.26. Computations of lateral wall movements based on optimization of Stage 3 wall movements yields poor “predictions” of measured lateral deformations at Stage 5 (Figure 4.26 (a)) because the deformation at Stage 3 which was used in the optimization was too small.

Predictions are made for Stage 7 based on the optimized parameters from SAA1Stage3,5. Measurements are larger than the computed predictions for Stage 7 (Figure 4.26 (b)). For the HS model to properly represent the soil response of Stage 7, a lower E_{50}^{ref} value than optimized from SAA1Stage3,5 should be incorporated as was shown in Figure 4.18.

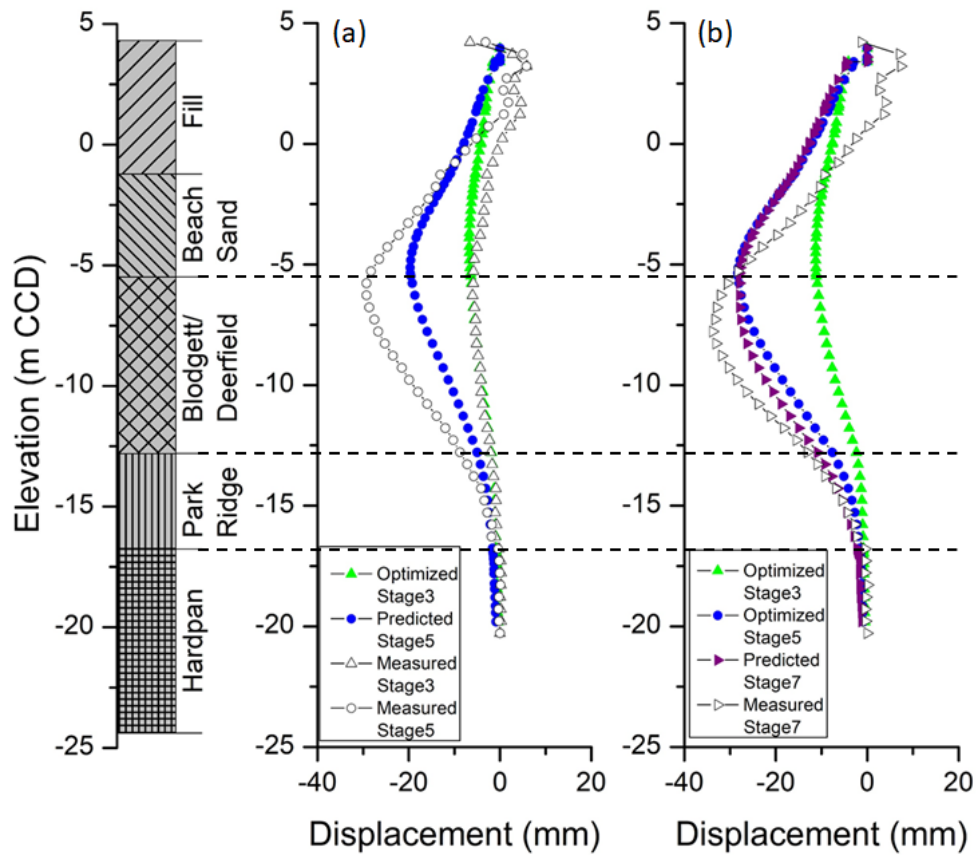


Figure 4.26 Prediction capabilities of HS model

Because a single set of HS model parameters cannot produce an E_{50}^{ref} value that decreases with increasing strain levels, one must have a reasonable estimation of the expected shear strain level when selecting parameters to accurately estimate the deformation at the end of excavation. To make proper predictions of later excavation stages with different shear strain levels, a soil model that represents both small and large strain levels through the use of a single set of model parameters must be employed.

- **HSS Model**

Computations based on optimizations of SAA1Stage3 and SAA1Stage3,5 are compared as in Figure 4.27. Computations of lateral wall movements based on optimization of Stage 3 wall movements yields poor “predictions” of measured lateral deformations at Stage 5 (Figure 4.27 (a)) because the deformation at Stage 3 which was used in the optimization was too small. Computation of lateral wall movements at Stage 7 based on the optimized parameters from SAA1Stage3,5 (Figure 4.27 (b)) yield good agreement to the observed values.

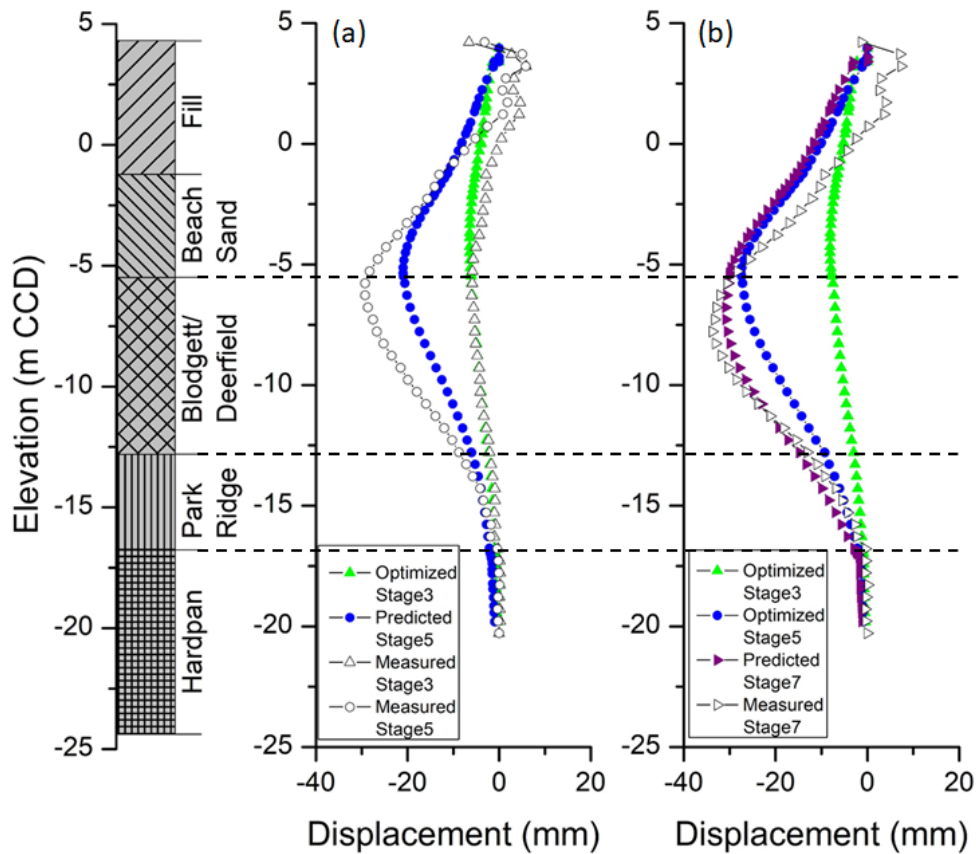


Figure 4.27 Prediction capabilities of HSS model

The HSS model incorporates small-strain stiffness responses, thus enabling representation of different strain levels with a single set of model parameters. In this case, the decrease of soil stiffness with shear strain is incorporated and thus allows better “prediction” of performance throughout the excavation sequence, at least when the strains reach levels that occurred at Stage 5, or about 0.10 %.

- **HC Model**

Computations based on optimizations of SAA1Stage3 and SAA1Stage3,5 are compared as in Figure 4.28. Computations of lateral wall movements based on optimization of Stage 3 wall movements yields close “predictions” of measured lateral deformations at Stage 5 (Figure 4.28 (a)). However, the optimized parameters were not within the range of reasonable soil parameters, therefore were not further considered.

Predictions are made for Stage 7 based on the optimized parameters from SAA1Stage3,5. Measurements are larger than the computed predictions for Stage 7 (Figure 4.28 (b)), visually indicating a worse fit compared to the HSS model.

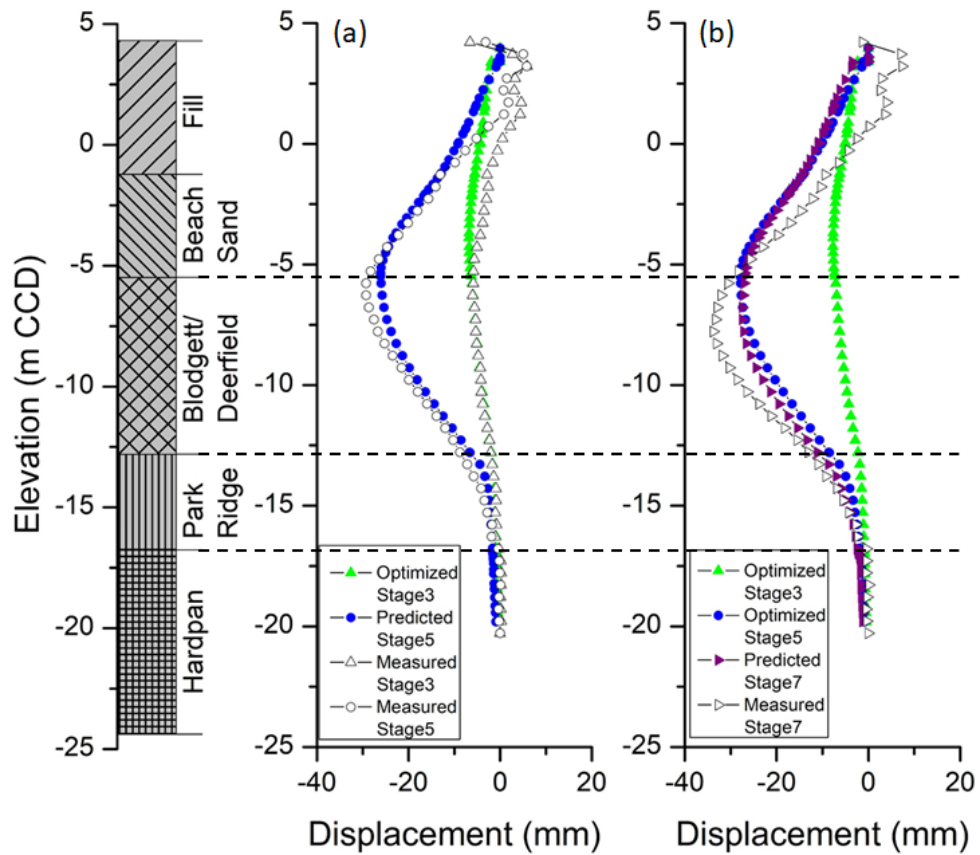


Figure 4.28 Prediction capabilities of HC model

- Overall Assessment

To assess the prediction capabilities of the three soil models, the computed lateral deformation at Stage 7 based on parameters optimized at SAA1Stage3,5 are shown in Figure 4.29. Comparisons show how close the “predictions” are with measurements.

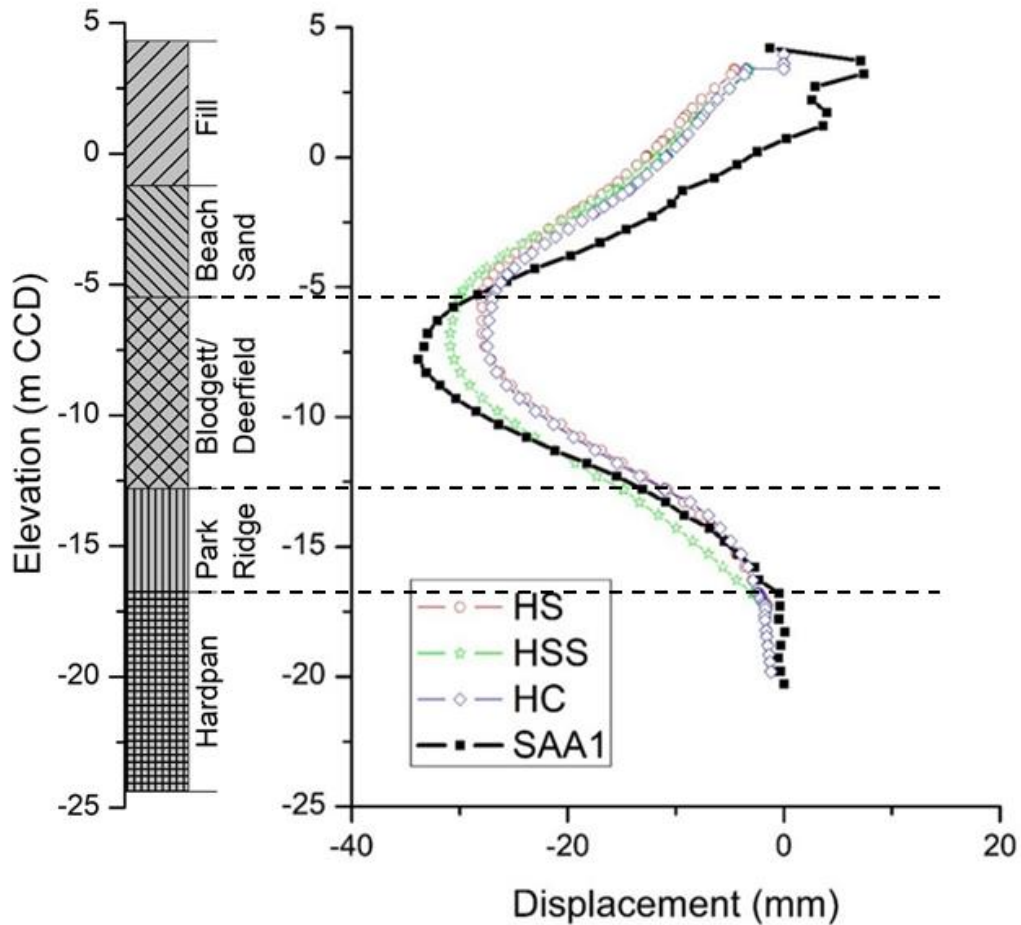


Figure 4.29 Measurements and predictions of Stage 7 based on SAA1Stage3,5 optimization

It is visually observed that the HSS model gives the closest predictions of the maximum lateral deformations measured at Stage 7. To quantify the quality of fit between the measured and “predicted” lateral wall movements at Stage 7, the RMSE values for the computed lateral deformations of Stage 7 based on optimized parameters of SAA1Stage3,5 were calculated as shown in Table 4.17.

Table 4.17 RMSE calculations of Stage 7 prediction using optimized parameters of SAA1Stage3,5

	Stage 7 “prediction”
HSS model	2.24
HC model	4.15

When the RMSE values for Stage 7 “predictions” are considered, the HSS model indicates a lower RMSE value that represents the better predictions compared to the HC model. This can also be observed in Figure 4.29. Therefore, it can be concluded that the HSS model was the most appropriate of the three under consideration in this thesis when computing lateral wall movements during excavation, at least for the strain levels at the SQBRC site.

4.3.4 Time-Dependent Deformations

All simulations for the inverse analyses carried out in the previous sections were strictly undrained models without any consideration on the effect of time-dependent deformations arising from pore water pressure responses. However, as shown in Section 3.6.1.4, time-dependent movements impact the final deformation levels for an excavation project if an excavation is open for sufficient periods of time. To consider this effect, additional FE simulations were conducted that included consolidation stages between and at the end of excavation stages as noted in Table 4.18. Four consolidation phases were added to the simulation.

Table 4.18 Modeling phases including consolidation

Modeling phases	Calculation type	Activity	Construction stages
Initial	K_0 consolidation	Initial soil condition	-
1	Plastic	Sheet pile wall installation	0
2	Plastic	Excavation to elev. +1.5 m CCD	1 (south)
3	Plastic	First level tieback on south wall at elev. +2.1 m CCD (Prestress: 330 kN)	2 (south)
4	Plastic	Excavation to elev. 0 m CCD	1 (north)
5	Plastic	First level tieback on north wall at elev. +0.6 m CCD (Prestress: 330 kN)	2 (north)
C1	Consolidation	Consolidation for 33 days	-
6	Plastic	Excavation to elev. -2.1 m CCD	3
7	Plastic	Strut installation at elev. -1.2 m CCD	4
C2	Consolidation	Consolidation for 65 days	-
8	Plastic	Excavation to elev. -6.7 m CCD	5
9	Plastic	Second level tieback at elev. -6.1 m CCD (Prestress: 490 kN)	6
C3	Consolidation	Consolidation for 32 days	-
10	Plastic	Excavation to elev. -8.8 m CCD	7
11	Plastic	Additional excavation at center of site (to elev. -13.7 m CCD)	-
C4	Consolidation	Consolidation for 130 days	10

The large incremental lateral deformation after Stage 7 to Stage 10 likely was a result of both time-dependent deformations and the additional level of excavation to elev. -13.7 m CCD at the center of the site. For a more realistic representation of the final construction stages, the additional level of excavation at the center of site (Figure 3.6) was included in the finite element simulation although the excavation did not represent strict plane strain conditions. The excavation for the tower crane near SAA-1 was not considered in the model because it was a localized excavation of limited extent.

Because the HSS model was considered most appropriate for use in excavations, the HSS model was employed in these finite element simulations. For calculations of the consolidation, permeabilities for the clays are needed. Permeabilities for the Blodgett/Deerfield, Park Ridge and Hardpan were taken from Sarabia (2012), which were back-calculated from relations between the downward flow and piezometer data observed during the Soldier Field and 14th and State projects in Chicago (Table 4.19).

Table 4.19 Permeabilities of clay layers

	Permeability (cm/s)
Blodgett/Deerfield	3.0×10^{-07}
Park Ridge	4.0×10^{-08}
Hardpan	3.0×10^{-08}

Finite element simulations of the modeling phases in Table 4.18 were first carried out with the optimized HSS model parameters based on all stages of excavation. Because of the uncertainty of permeability values at the SQBRC site, a range of permeability values were considered. The

default permeabilities used in the analysis are those presented in Table 4.19. Permeabilities for the Blodgett/Deerfield and Park Ridge layers were multiplied by 2, 3 and 5 for a parametric study. The permeability for Hardpan was not altered because it represented a low permeability value which would not significantly affect the overall performance. Computed lateral wall movements at the latter stages of the excavation project are shown in Table 4.20. The incremental deformations between Stage 7 and Stage 10 are also shown in Table 4.20 and are compared with the observed deformations at SAA-1.

Table 4.20 Lateral wall movements (mm) for computations using various permeability cases

	Stage 7	Additional excavation	Stage 10	Incremental (Stage 7 to 10)
SAA-1 measurement	34	-	51	17
With consolidation (k×1)	32	37	44	12
With consolidation (k×2)	34	39	50	16
With consolidation (k×3)	35	41	55	20
With consolidation (k×5)	36	44	64	28

From Table 4.20, it is seen that the simulation including consolidation with k×2 gives the closest deformation levels with the measurements of SAA-1. Therefore, the permeability of k×2 seemed to be the most reasonable for the SQBRC site, assuming the optimized HSS parameters are “correct.” To assess the impacts of including consolidation on the optimized parameters, optimization was carried out using modeling phases of Table 4.18 (consolidation included). For the initial values, HSS model parameters of Table 4.5 were used. Parameters based on optimization of data from Stage 3, 5 and 7 for both undrained and consolidation phases are shown in Table 4.21.

Table 4.21 Parameters optimized from undrained and consolidation-considered models

	Blodgett/ Deerfield		Park Ridge	
	E_{50}^{ref} (kPa)	$\gamma_{0.7}$	E_{50}^{ref} (kPa)	$\gamma_{0.7}$
Initial	12,500	1.00×10^{-05}	35,000	1.00×10^{-05}
Undrained	8,900	7.20×10^{-05}	50,800	2.26×10^{-04}
Consolidation with $k \times 2$	11,000	7.73×10^{-05}	98,400	7.85×10^{-04}

Results shown in Table 4.21 indicate that the Blodgett/Deerfield E_{50}^{ref} parameters based on consolidation are 24 % stiffer than those found in the undrained case. The same trends were observed for the Park Ridge, but the E_{50}^{ref} was almost twice as large for the consolidation case. These trends are reasonable because the dissipation of excess pore water pressure during these stages contribute to the observed deformations, and thus the stiffness of the soil must be larger so that the total movements are the same.

Lateral wall movements at Stage 10 were computed using the parameters optimized with the consolidation-included model and compared with the field observations in Figure 4.30. As expected, computations of Stage 3, 5 and 7 indicated a close fit with the measurements of SAA-1 since these data formed the basis of the optimization. The “predicted” lateral wall movements of Stage 10 were slightly larger near the upper portions of the Blodgett/Deerfield than measured at SAA-1. The lower computed deformation level at Stage 10 may be due to the simplicity of the finite element simulation. The localized excavation and additional level of tieback anchors in front of SAA-1 for the tower cranes, possible creep deformations and secondary construction activities were not considered in the finite element model, resulting in a lower final lateral deformation

compared to the measurements. Alternatively, because the main difference in the computed and observed results occurred near a drainage boundary (i.e., the bottom of the beach sand), perhaps a more refined mesh was required to adequately capture the response of the 130 days of pore pressure changes.

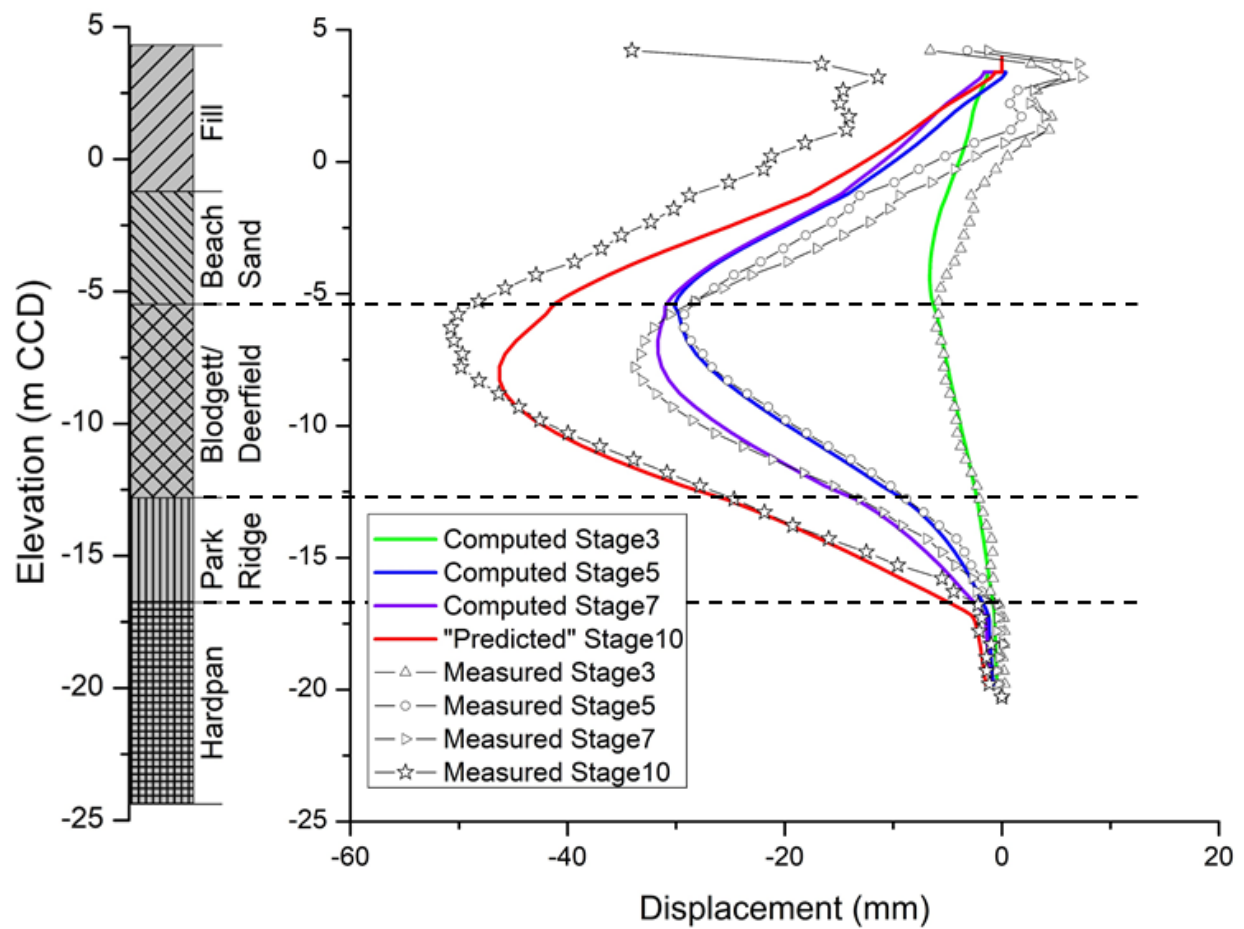


Figure 4.30 Computed deformation using optimized parameters from SAA1Stage3,5,7

Analysis through a more precise and realistic finite element simulation may have resulted in a closer fit between the predictions and measurements, but this not possible due to the complex nature of excavation activities and the size of mesh. However, the prediction of lateral deformations at the wall came within 17 % of the field measurements, similar to the 15 % accuracy one can expect with lateral wall movements as discussed in Chapter 3. In this light, one can still obtain a reasonable representation of the observed displacements even with the simplifications included in the finite element model.

4.5 Summary and Conclusions

Optimization of soil parameters based on lateral wall movements observed at the SQBRC excavation were conducted with inverse analysis based on a gradient method. PLAXIS 2D was used for the finite element simulations. Undrained conditions were assumed for most of the analyses. SAA-1 data were chosen as the lateral measurements to be used in the optimization due to their reliability and proximity to the center of the north wall. Lateral wall movements measured in the Blodgett/Deerfield and Park Ridge clay layers were used for optimization purposes.

The HS model was evaluated herein due to its simplicity and its previous applications to Chicago clays in case studies. Parameters based on optimization of SAA1Stage3 data produced very stiff soil responses at subsequent stages due to the very low deformation levels (6 mm) measured at Stage 3. When optimizing based on data from SAA1Stage3,5 and SAA1Stage3,5,7, lower E_{50}^{ref} values were found that were representative of the larger deformation levels (and thus strains in the retained soil) in the measurements at later stages. The decrease in E_{50}^{ref} with shear

strain, consistent with results of past studies (i.e., Finno and Calvello 2005, Rechea 2006), suggested the use of a soil model which explicitly represents the small strain stiffness behavior of natural soils.

The HSS model is one such small strain model. For simulations with this model, the E_{50}^{ref} and $\gamma_{0.7}$ parameters were optimized in both the Blodgett/Deerfield and Park Ridge layers. These parameters represent the “large” strain and “very small” strain behavior, respectively. The optimization at SAA1Stage3 resulted in parameter values that were not reasonable and did not produce reliable predictions of later stages due to the small deformations that occurred at Stage 3. Optimizations with small deformations resulted in larger stiffness values, characterized by either a large E_{50}^{ref} value or a large $\gamma_{0.7}$ value. To obtain reasonable optimized parameters, a larger range of deformations must be considered. This explains why the optimized parameters are more reasonable for the optimization of SAA1Stage3,5 and SAA1Stage3,5,7. For the Blodgett/Deerfield, the optimized soil parameters only change 16 % between SAA1Stage3,5 and SAA1Stage3,5,7. Small deformation levels in the Park Ridge were also reasonably represented with the optimized soil parameters. It was found that a reasonable soil parameter optimization was completed at SAA1Stage3,5 where the shear strain reached as high as approximately 0.10 %.

The HC model had not been optimized previously using field measurements. Therefore, sensitivity analyses were performed to select the parameters for optimization. Results of the calculations indicate that at most cases κ^* and R_{max} are the best pair of parameters to be optimized, with highest CSS values among the large and small strain parameters, respectively. However, because λ^* and κ^* are measured reliably in laboratory oedometer tests and are well-correlated with index properties for Chicago clays (e.g., Sarabia 2012), v_{pp} was chosen as the parameter to be

optimized instead of κ^* . The small strain parameters indicated larger CSS values than the large strain parameters for all cases. Results of correlation analyses indicated PCC values lower than 0.9, showing that v_{pp} and R_{max} could be optimized reliably at the same time.

Optimizations using the HC model also showed unreasonable parameter values at Stage3 due to the observed small deformation levels. Optimizations using SAA1Stage3,5 and SAA1Stage3,5,7 provided reasonable parameters within the ranges reported for various clays (Masin 2011). Optimized parameters for the Blodgett/Deerfield showed very little changes whereas the Park Ridge parameter v_{pp} differed significantly between the two optimization stages. Although the optimized v_{pp} parameters of Park Ridge were significantly different in the two optimization stages, the most influential parameter for the Park Ridge, R_{max} , was reasonably optimized at SAA1Stage3,5 and changed by only 15 % when optimized at SAA1Stage3,5,7. It was found for the HC model that a reasonable soil parameter optimization was completed at SAA1Stage3,5 where the shear strain reached as high as approximately 0.10 %.

Predictions of Stage 7 deformations were made based on the optimization carried out for SAA1Stage3,5. Calculations of RMSE values showed that the HSS model made better Stage 7 predictions than the HC model. In an excavation project, it is important to make predictions of the deformations at the end of excavation based on data collected at earlier stages of the project. Considering the visual fit and the RMSE calculations, the HSS model was considered to make better predictions of the end of excavation than the HC model. Therefore, it can be concluded that the HSS model is most appropriate soil model of the three considered when computing lateral wall movements during an excavation project, at least for the strain levels at SQBRC.

To assess the effect of including time-dependent deformations due to pore water pressure changes, consolidation stages were modeled between the excavation stages and at the end of excavation. Optimizations were conducted for these simulations as well. The HSS model was used because it was considered the most appropriate soil model for excavation simulations. Optimized E_{50}^{ref} parameters based on Stages 3, 5 and 7 for Blodgett/Deerfield were 24 % stiffer than those for the undrained simulation. “Predictions” of the lateral wall deformations at Stage 10 were made using the optimized parameters with SAA1Stage3,5,7. The computed deformations were slightly lower than the measured deformations at Stage 10. This difference may be due to the additional localized excavation carried out near SAA-1, possible creep deformations or secondary construction activities, all of which were not modeled in the finite element simulation. An additional factor may be the fineness of the mesh near the drainage boundary. However, given these limitations, “predictions” for Stage 10 movements were within 17 % of the observed values, a value consistent with the variability of high quality lateral wall movement data, as noted in Chapter 3.

Chapter 5 Summary and Conclusions

5.1 Summary

Inverse analysis has been widely used along with finite element models in the past to produce realistic and reliable results for performance-based geotechnical problems. Inverse analysis was carried out using data from the sheet pile-supported SQBRC excavation in Chicago. Field measurements and PLAXIS 2D model computations of the lateral deformation at the wall were used for optimization purposes. Three soil models (HS model, HSS model and HC model) were used to assess the effects of soil model when computing lateral wall movements during excavations in typical Chicago clays.

Chapter 2 presented the technical background for the work conducted as part of this thesis. The adaptive management approach was introduced, and a brief summary of past studies on the performance of deep excavations was presented. The inverse analysis method based on the gradient method was described. The three constitutive soil models considered in this thesis were summarized. Previous studies of inverse analysis applied to Chicago soils using the three soil models were summarized.

Chapter 3 analyzed the observed performance of the Louis A. Simpson and Kimberly K. Query Biomedical Research Center (SQBRC) located in downtown Chicago. The measured ground and wall responses were described and correlated with responses of the construction activities. The responses were evaluated in light of subsurface conditions, support system stiffness and other nearby excavations. The expected performance based on semi-empirical correlations

were compared with the measured response. With a detailed analysis of the observed performance, the SQBRC excavation was used as a test bed for the inverse analysis of Chapter 4.

Chapter 4 described the inverse analysis results that were carried out for the SQBRC excavation. PLAXIS 2D was used to simulate the plane strain conditions. The HS model, HSS model and HC model were used to represent the Blodgett/Deerfield and Park Ridge layers. The HS model was chosen due to its simplicity and the wide application on Chicago clays in past case studies. The HSS and HC models were chosen due to their consideration on small-strain stiffness. Initial parameters for each of the soil models were based on previous inverse analysis studies that have been carried out for Chicago soils. SAA-1 measurements of the lateral wall displacements at Stages 3, 5 and 7 were used for the observations in the inverse analysis. The soil parameters were calibrated starting at Stage 3 and recalibrated at Stages 5 and 7 using all SAA-1 measurements available up to that stage. Optimized parameters were checked whether they were reasonable and within those expected for the soil. Soil parameters optimized in early stages of the project were used to predict the soil deformation of later stages. The HSS model allowed the best “Class C” predictions of maximum lateral deformation and is considered the most appropriate of the three considered soil models for predicting excavation performance in Chicago clays.

In addition to the undrained finite element simulations, consolidation was considered to assess the time-dependent deformations that were observed in the field measurements. Soil parameter optimization for the HSS model was again carried out for the consolidation model. Optimized soil parameters produced reasonable predictions of the final deformation level.

5.2 Conclusions

The adaptive management approach can be applied to geotechnical constructions by optimizing the soil parameters during earlier stages using inverse analysis techniques and applying the optimized parameters to make predictions of movements at later stages of a project. For reasonable outcomes, the relation between the observed deformations and the construction process must be thoroughly understood.

Based on the results of the analyses of the observed performance at SQBRC presented herein, the following conclusions can be drawn regarding its performance.

1. No more than 8 mm of lateral wall movements were noted until the excavation reached the soft to medium stiff clay of the Blodgett/Deerfield stratum. The largest incremental movements occurred when the excavation was lowered into this stratum.
2. Time-dependent lateral wall movements developed at a rate of about 3 mm/month and persisted until the permanent support walls were either cast against the sheeting at the north wall or braced with flowable fill along the south wall. Maximum lateral movements thus also depend on the amount of time before a temporary wall is structurally constrained.
3. The intermittent presence of an access ramp at the south wall influenced the development of the lateral wall movements at that location as observed in SAA-5. No significant lateral movement was observed until the access ramp was removed. Comparing the wall movements at the end of excavation for the north and south walls, the presence of the access ramp apparently had little impact on the ultimate values. However, if one desires to use

observations to track design estimates or update performance predictions, then the effects of the ramp must be accounted for in the process.

4. Given the similarity in soil conditions, bracing systems and the range of lateral wall movements observed at the SQBRC and Lurie sites, one can expect to be able to predict lateral wall deformations at various locations around a site in similar cases with an accuracy of no more than $\pm 15\%$ of the maximum value.
5. The ratio of excavation-induced maximum settlement to maximum lateral wall movement varies with excavation depth. At later stages near the end of excavation, the ratios based on measurements were approximately 0.8 to 1.0.
6. The normalized wall movements at SQBRC caused by cycles of excavation and bracing varied between 0.22 and 0.32 % at the last two stages of excavation. These measured values can be roughly estimated based on the Clough et al. (1989) chart using system stiffness and factor of safety against basal heave.

Optimization of soil parameters based on observed lateral wall movements were conducted with inverse analysis based on a gradient method. The following conclusions can be drawn regarding the inverse analysis of excavation-induced lateral wall movements at the SQBRC excavation.

1. The HS model optimization based on SAA1Stage3 produced unreasonable predictions of subsequent stages due to the very small deformation levels in the clay strata (6 mm) measured at Stage 3. When optimizing based on data from SAA1Stage3,5 and SAA1Stage3,5,7, lower E_{50}^{ref} values were found that were representative of the larger deformation (strain) levels in the measurements of later stages. The decrease in E_{50}^{ref} with

shear strain suggested the use of a soil model which explicitly represents the small strain stiffness behavior of natural soils.

2. The E_{50}^{ref} and $\gamma_{0.7}$ parameters were optimized for the HSS model optimization. The optimizations using low deformations of SAA1Stage3 resulted in larger stiffness values than expected, characterized by either a large E_{50}^{ref} value or a large $\gamma_{0.7}$ value. To obtain reasonable optimized parameters, a larger range of deformation (strain) must be considered. For the Blodgett/Deerfield, the optimized soil parameters only change 16 % between SAA1Stage3,5 and SAA1Stage3,5,7. Optimized parameters for the Park Ridge reasonably represented the stiff response in the layer. Reasonable soil parameter optimization for the HSS model was completed at SAA1Stage3,5 where the shear strain reached as high as 0.10 %.
3. Results of the sensitivity analyses for the HC model indicate that at most cases κ^* and R_{max} are the best pair of parameters to be optimized. However, because λ^* and κ^* are reasonably measured in laboratory oedometer tests, v_{pp} was chosen as the parameter to be optimized instead of κ^* . Small strain parameters indicated significantly larger sensitivities than the large strain parameters. Correlation analyses indicated that v_{pp} and R_{max} could be optimized reasonably at the same time.
4. Optimizations using the HC model also showed unreasonable parameter values at Stage3 due to the observed small deformation levels. HC model optimizations using SAA1Stage3,5 and SAA1Stage3,5,7 provide reasonable parameters. Optimized parameters for the Blodgett/Deerfield showed very little changes between the two optimization stages. Although the optimized v_{pp} parameters of Park Ridge were significantly different in the two optimization stages, the most influential parameter for the

Park Ridge stratum, R_{\max} , was reasonably optimized at SAA1Stage3,5, and changed by only 15 % when optimized at SAA1Stage3,5,7. Reasonable soil parameter optimization for the HC model was completed at SAA1Stage3,5 where the shear strain reached as high as 0.10 %.

5. Calculations of Root Mean Squared Error (RMSE) values showed that the HSS model made computations of Stage 7 closer to the measurements than the HC model. It can be concluded that the HSS model is most appropriate of the three considered soil models when computing lateral wall movements during an excavation project, at least for the strain levels at SQBRC.
6. To assess the effect of including time-dependent deformations due to pore water pressure changes, optimizations were conducted for a finite element model including consolidation. Optimized HSS model parameters were stiffer than those found in the undrained case due to the additional lateral movements caused by the excess pore water pressure dissipation. Lateral deformations at Stage 10 were computed using the parameters optimized from the consolidation case, producing reasonable predictions within 17 % of the observed values, consistent with the 15 % accuracy one can expect with lateral wall deformations.

References

Arboleda-Monsalve, L.G. (2014). "Performance, Instrumentation and Numerical Simulation of One Museum Park West Excavation." PhD thesis, Northwestern University, Evanston, IL.

Arboleda-Monsalve, L.G., Teng, F., Kim, T. and Finno, R.J. (2017). "Numerical Simulation of Triaxial Stress Probes and Recent Stress-History Effects of Compressible Chicago Glacial Clays." *Journal of Geotechnical and Geoenvironmental Engineering*, 143(7): 04017029.

Atkinson, J.H. and Salfors, G. (1991). "Experimental Determination of Soil Properties." *Proceedings*, 10th ECSMFE, 3, 915-956.

Benz, T. (2006). "Small-Strain Stiffness of Soils and its Numerical Consequences." PhD thesis, Universitat Stuttgart, Stuttgart, Germany.

Blackburn, J.T. (2005). "Automated Remote Sensing and Three-Dimensional Analysis of Internally Braced Excavations." PhD thesis, Northwestern University, Evanston, IL.

Blackburn, J.T. and Finno, R.J. (2007). "Three-Dimensional Responses Observed in an Internally Braced Excavation in Soft Clay." *Journal of Geotechnical and Geoenvironmental Engineering*, 133(11), 1364-1373.

Bryson, L.S. (2002). "Performance of a Stiff Excavation Support System in Soft Clay and the Response of an Adjacent Building." PhD thesis, Northwestern University, Evanston, IL.

Bryson, L.S. and Zapata-Median, D.G. (2012). "Method for Estimating System Stiffness for Excavation Support Walls." *Journal of Geotechnical and Geoenvironmental Engineering*, 138(9), 1104-1115.

Butterfield, R. (1979). "A Natural Compression Law for Soils (An Advance on e-logp'')."

Calvello, M. (2002). "Inverse Analysis of a Supported Excavation through Chicago Glacial Clays." PhD thesis, Northwestern University, Evanston, IL.

- Calvello, M. and Finno, R.J. (2004). "Selecting Parameters to Optimize in Model Calibration by Inverse Analysis." *Computers and Geotechnics*, 31(5), 411-425.
- Cho, W. (2007). "Recent Stress History Effects on Compressible Chicago Glacial Clay." PhD thesis, Northwestern University, Evanston, IL.
- Cho W. and Finno, R.J. (2010). "Stress-Strain Response of Block Samples of Compressible Chicago Glacial Clays." *Journal of Geotechnical and Geoenvironmental Engineering*, 135(1), 178-188.
- Chung, C.K. and Finno, R.J. (1992). "Influence of Depositional Processes on the Geotechnical Parameters of Chicago Glacial Clays." *Engineering Geology*, 32, 225-242.
- Clough G.W. and O'Rourke, T.D. (1992). "Construction Induced Movements of Insitu Walls." *Design and Performance of Earth Retaining Structures, Proceedings, Specialty Conference at Cornell University, NY*, 439-470.
- Clough, G.W., Smith, E.M., and Sweeney, B.P. (1989). "Movement Control of Excavation Support Systems by Iterative Design." *Foundation Engineering: Current Principles and Practices (GSP 22)*, 869-884.
- Delaunay, B. (1934). "Sur la sphère vide." *Bulletin de l'Académie des Sciences de l'URSS, Classe des sciences mathématiques et naturelles*, 6, 793-800 (in French).
- Finno, R.J. (2007). "Use of Monitoring Data to Update Performance Predictions of Supported Excavations." *7th FMGM 2007: Field Measurements in Geomechanics*, 1-30.
- Finno, R.J. (2008). "Linking Field Observations and Performance Prediction Updates during Construction." *Proceedings, 15th Great Lakes Geotechnical/Geoenvironmental Conference, ASCE, Indianapolis, IN*.
- Finno, R.J. and Bryson, L.S. (2002). "Response of Building Adjacent to Stiff Excavation Support System in Soft Clay." *Journal of Performance of Constructed Facilities*, 16(1), 10-20.
- Finno, R.J., Bryson, S. and Calvello, M. (2002). "Performance of a Stiff Support System in Soft Clay." *Journal of Geotechnical and Geoenvironmental Engineering*, 128(8), 660-671.

- Finno, R.J. and Calvello, M. (2005). "Supported Excavations: Observational Method and Inverse Modeling." *Journal of Geotechnical and Geoenvironmental Engineering*, 131(7), 826-836.
- Finno, R.J. and Cho, W. (2011). "Recent Stress History Effects on Compressible Chicago Glacial Clays." *Journal of Geotechnical and Geoenvironmental Engineering*, 137(3), 197-207.
- Finno, R.J. and Chung, C.K. (1992). "Stress-Strain-Strength Responses of Compressible Chicago Glacial Clays." *Journal of Geotechnical Engineering*, 118(10), 1607-1625.
- Finno, R.J., Hiltunen, D.R. and Kim, T. (2012). "Elastic Cross-Anisotropy of Chicago Glacial Clays from Field and Laboratory Data." *Proceedings, State of the Art and Practice in Geotechnical Engineering, GeoCongress 2012, Oakland, CA*, 2609-2618.
- Finno, R.J. and Kim, T. (2012). "Effects of Stress Path Rotation Angle on Small Strain Responses." *Journal of Geotechnical and Geoenvironmental Engineering*, 138(4), 526-534.
- Finno, R.J. and Roboski, J.F. (2005). "Three-dimensional Responses of a Tied-back Excavation through Clay." *Journal of Geotechnical and Geoenvironmental Engineering*, 131(3), 273-282.
- Finno, R.J., Shi, Z., Kim, S., Crafton, N. and Rendell, D. (2017). "Adaptive management evaluation of the SQBRC excavation." *Proceedings, Workshop for Simulation of Construction Processes in Geotechnical Engineering FOR 1136 GEOTECH, Karlsruhe, Germany*, 42-67.
- Gioda, G. and Locatelli, L. (1999). "Back Analysis of the Measurements Performed during the Excavation of a Shallow Tunnel in Sand." *International Journal for Numerical and Analytical Methods in Geomechanics*, 23(13), 1407-1425.
- Glatt, J., Roboski, J. and Finno, R.J. (2004). "Sheetpile-induced vibrations at the Lurie Excavation Project." *Proceedings, Geotrans 2004, ASCE, Los Angeles, CA*, 2130-2138.
- Goldberg, D.T., Jaworski, W.E. and Gordon, M.D. (1976). "Lateral Supports Systems and Underpinning." Report FHWA-RD-75-128, Federal Highway Administration, Washington D.C.
- Gudehus, G., Amorosi, A., Gens, A., Herle, I., Kolymbas, D., Masin, D., Muir Wood, D., Nova, R., Niumunis, A., Pastor, M., Tamagnini, C. and Viggiani, G. (2008). "The Soilmodels.info

Project.” *International Journal for Numerical and Analytical Methods in Geomechanics*, 32(12), 1571-1572.

Hardin, B.O. and Drnevich, V.P. (1972). “Shear Modulus and Damping in Soils: Design Equations and Curves.” *Proceedings, ASCE Journal of the Soil Mechanics and Foundations Division*, 98(SM7), 667-692.

Hashash, Y.M.A. and Finno, R.J. (2008). “Development of New Integrated Tools for Predicting, Monitoring and Controlling Ground Movements due to Excavations.” *Practice Periodical on Structural Design and Construction*, 13(1), 4-10.

Honjo, Y., Wen-Tsung, L. and Guha, D. (1994). “Inverse Analysis of an Embankment of Soft Clay by Extended Bayesian Method.” *International Journal for Numerical and Analytical Methods in Geomechanics*, 18, 709-734.

Hsieh, P.G., and Ou, C.Y. (1998). “Shape of ground surface settlement profiles caused by excavation.” *Canadian Geotechnical Journal*, 35, 1004-1017.

Kern, K.S. (2014). “Behavior of Chicago Desiccated Clay Crust and its Effect on Excavation-Induced Ground Movements.” PhD thesis, Northwestern University, Evanston, IL.

Kim, T. (2011). “Incrementally Nonlinear Responses of Soft Chicago Glacial Clays.” PhD thesis, Northwestern University, Evanston, IL.

Kim, T. and Finno, R.J. (2012). “Anisotropy Evolution and Irrecoverable Deformation in Triaxial Stress Probes.” *Journal of Geotechnical and Geoenvironmental Engineering*, 138(2), 155-165.

Kolymbas, D. (1991). “An Outline of Hypoplasticity.” *Archive of Applied Mechanics*, 61, 143-151.

Lambe, T.W. (1970). “Braced Excavations.” *ASCE Specialty Conference on Lateral Stresses in Ground and Design of Earth-Retaining Structures*, Ithaca, NY, 149-218.

Ledesma, A., Gens, A., Alonso, E.E. (1996). “Estimation of Parameters in Geotechnical Backanalysis – Maximum Likelihood Approach.” *Computers and Geotechnics*, 18(1), 1-27.

- Mana, A.I. and Clough, G.W. (1981). "Prediction of Movements for Braced Cuts in Clay." *Journal of the Geotechnical Engineering Division*, 107(6), 759-777.
- Masin, D. (2005). "A Hypoplastic Constitutive Model for Clays." *International Journal of Numerical and Analytical Methods*, 29, 311-336.
- Masin, D. (2006). "Hypoplastic Models for Fine-Grained Soils." PhD thesis, Charles University, Prague.
- Masin, D. (2011). "Hypoplasticity for Practical Applications, Determination of Material Parameters." PhD course handouts on hypoplasticity, Faculty of Science, Charles University in Prague.
- Masin, D. (2013). "Clay Hypoplasticity with Explicitly Defined Asymptotic States." *Acta Geotechnica*, 8(5), 481-496.
- Masin, D. (2014). "Clay Hypoplasticity Model Including Stiffness Anisotropy." *Geotechnique*, 64(3), 232-238.
- Masin, D. and Rott, J. (2014). "Small Strain Stiffness Anisotropy of Natural Sedimentary Clays: Review and a Model." *Acta Geotechnica*, 9(2), 299-312.
- Morgenstern, N. (1995). "Managing Risk in Geotechnical Engineering." *Proceedings, 10th Pan American Conference on Soil Mechanics and Foundation Engineering*, Volume 4.
- Mu, L., Finno, R.J., Huang, M., Kim, T. and Kern, K. (2015). "Defining the Soil Parameters for Computing Deformations Caused by Braced Excavation." *Maejo International Journal of Science and Technology*, 9(2), 165-180.
- Mu, L. and Huang, M. (2016). "Small Strain based Method for Predicting Three-Dimensional Soil Displacements Induced by Braced Excavation." *Tunnelling and Underground Space Technology*, 52, 12-22.
- Niemunis, A. and Herle, I. (1997). "Hypoplastic Model for Cohesionless Soils with Elastic Strain Range." *Mechanics of Cohesive-Frictional Materials*, 2, 279-299.

O'Rourke, T.D. (1981). "Ground Movements Caused by Braced Excavations." *Journal of the Geotechnical Engineering Division*, 105(4), 481-498.

Ou, C.Y. and Tang, Y.G. (1994). "Soil Parameter Determination for Deep Excavation Analysis by Optimization." *Journal of the Chinese Institute of Engineering*, 17(5), 671-688.

Peck, R.B. (1969). "Deep Excavations and Tunneling in Soft Ground." *Proceedings, 7th International Conference on Soil Mechanics and Foundation Engineering, State-of-the-Art Volume*, 225-290.

PLAXIS (2016). *2D Foundation Manual*.

Poeter, E.P. and Hill, M.C. (1998). "Documentation of UCODE, A Computer Code for Universal Inverse Modeling." *U.S. Geological Survey Water-Resources Investigations Report 98-4080*.

Rechea, C. (2006). "Inverse Analysis of Excavations in Urban Environments." PhD thesis, Northwestern University, Evanston, IL.

Roboski, J.F. (2001). "Soil Parameters for Constitutive Models of Compressible Chicago Glacial Clays." MS thesis, Northwestern University, Evanston, IL.

Roboski, J.F. (2004). "Three-Dimensional Performance and Analyses of Deep Excavations." PhD thesis, Northwestern University, Evanston, IL.

Roboski, J.F. and Finno, R.J. (2006). "Distributions of Ground Movements Parallel to Deep Excavations." *Canadian Geotechnical Journal*, 43(1), 43-58.

Sarabia, F. (2012). "Hypoplastic Constitutive Law Adapted to Simulate Excavations in Chicago Glacial Clays." PhD thesis, Northwestern University, Evanston, IL.

Schantz, T., Vermeer, P.A. and Bonnier, P.G. (1999). "The Hardening Soil Model: Formulation and Verification." *Beyond 2000 in Computational Geotechnics*, Balkema, Rotterdam, 291-290.

Terzaghi, K. (1943). *Theoretical Soil Mechanics*, Wiley and Sons, London and New York, 189-194.

Van Winkle, N.P. (2016). "Performance of the SQBRC Excavation in Chicago." MS thesis, Northwestern University, Evanston, IL.

Wang, J. (2011). "Laboratory Testing on Chicago Hard Clays." Internal Report, Northwestern University.

Whitman, R.V. (2000). "Organizing and Evaluating Uncertainty in Geotechnical Engineering." *Journal of Geotechnical and Geoenvironmental Engineering*, 126(7), 583-593.

Appendix

A. PYTHON code

Example for HS model optimization using SAA1Stage3,5,7

Note: The finite element model PLAXIS 2D employed for the inverse analysis used US units (ft, in). Therefore, the PYTHON code was also developed using US units.

```
import os

# set up file paths
main_dir = r'D:\Google Drive D\Feinberg\Plaxis2D\Hardening Soil\Lurie
Comparison\Optimization_HS\Feinberg_Inverse_Analysis'
folder_paras = main_dir + '/parameter/'
folder_predict = main_dir + '/prediction/'
folder_comput = main_dir + '/computation/'
file_paras = folder_paras + 'proc_paras.txt'
file_predict1 = folder_predict + 'pre_inclinometer1.txt'
file_predict3 = folder_predict + 'pre_inclinometer3.txt'
file_predict5 = folder_predict + 'pre_inclinometer5.txt'
file_phase = folder_comput + 'computation_phase.txt'

# read parameters from file
with open(file_paras,'r') as paras_f:
    paras =(paras_f.read()).split("\n")
    paras_f.close()

# read computation phase from file
with open(file_phase , 'r') as phase_f:
```

```

phases =(phase_f.read()).split("\n')
phase_f.close()
num_phase =int(phases[0])

# connect with remote control server in plaxis:
localhostport_input = 10001
localhostport_output = 10002
plaxis_path = r'C:\Program Files (x86)\Plaxis\PLAXIS 2D'

import imp
found_module = imp.find_module('plxscripting', [plaxis_path])
plxscripting = imp.load_module('plxscripting', *found_module)
from plxscripting.easy import *
s, g = new_server('localhost', localhostport_input)
s_out, g_out = new_server('localhost', localhostport_output)

# change the model parameters
g.HS_DB.setproperties("E50ref",float(paras[0]),"Eoedref",0.7*float(paras[0]),"Gref",1.25*float(
paras[0]),"nu",0.2)
g.HS_ParkRidge.setproperties("E50ref",float(paras[1]),"Eoedref",0.7*float(paras[1]),"Gref",1.25
*float(paras[1]),"nu",0.2)
print ('Parameters have been changed')

# switch on calculation for all stages
g.gotostages()
for i in range(0,12):
    if i <= num_phase:
        g.Phases[i].ShouldCalculate = True
    else:

```

```

g.Phases[i].ShouldCalculate = False

g.calculate()
print ('Calculation finished')

# obtain the lateral displacement for specific points
incre_inclino = 1.64;
num_mspts = 23 # number of measurement points
num_phase = 6
g.view(g_out.Phases[num_phase])
t_inclino = -18.97;          # top elevation of SAA
x_inclino1 = 223+0.5;       # horizontal location of SAA from wall
list_dispx1 = []
for i in range(1,int(num_mspts)+1):
    y_mspts = t_inclino -(i-1)*incre_inclino
    x_mspts = x_inclino1
    disp_x =
g_out.getsingleresult(g_out.Phases[num_phase],g_out.ResultTypes.Soil.Ux,(x_mspts,y_mspts))
    list_dispx1.append(disp_x)
with open(file_predict1,'w+') as dispx_f:
    for disp_x in list_dispx1:
        dispx_f.write("%s\n" %disp_x)
dispx_f.close()
g_out.close()

num_phase = 8
g.view(g_out.Phases[num_phase])
t_inclino = -18.97;
x_inclino3 = 223+0.5;

```

```

list_dispx3 = []
for i in range(1,int(num_mspts)+1):
    y_mspts = t_inclino -(i-1)*incre_inclino
    x_mspts = x_inclino3

    disp_x =
g_out.getsingleresult(g_out.Phases[num_phase],g_out.ResultTypes.Soil.Ux,(x_mspts,y_mspts))
    list_dispx3.append(disp_x)
with open(file_predict3,'w+') as disp_x_f:
    for disp_x in list_dispx3:
        disp_x_f.write("%s\n" %disp_x)
disp_x_f.close()
g_out.close()

num_phase = 10
g.view(g_out.Phases[num_phase])
t_inclino = -18.97;
x_inclino5 = 223+0.5;
list_dispx5 = []
for i in range(1,int(num_mspts)+1):
    y_mspts = t_inclino -(i-1)*incre_inclino
    x_mspts = x_inclino5

    disp_x =
g_out.getsingleresult(g_out.Phases[num_phase],g_out.ResultTypes.Soil.Ux,(x_mspts,y_mspts))
    list_dispx5.append(disp_x)
with open(file_predict5,'w+') as disp_x_f:
    for disp_x in list_dispx5:
        disp_x_f.write("%s\n" %disp_x)
disp_x_f.close()
g_out.close()

```

B. MATLAB codes

Example for HS model optimization using SAA1Stage3,5,7

- Optimization Driver

```

clc
clear

% obtain the initial guess of parameters

main_dir = pwd;

para_folder = [main_dir , '/parameter/'];
pred_folder = [main_dir , '/prediction/'];

%reading parameters
ini_para=csvread([para_folder, 'ini_params.txt']); % initial input for E50ref
for HS
%typ_para=csvread([para_folder,'typ_params.txt']); % typical values for
parameters E50ref,psi for HS
typ_para=ini_para;

%%L-M algorithm

lb=[ , ]; %lower boundary
ub=[ , ]; %upper boundary

rel_step=0.01;

%statement creates an optimization options structure in which a L-M and the
forward differences are used.
% remember to change the tolerances, for 3 parameters 'TolFun',0.0001
options=optimset('TypicalX', typ_para, 'ScaleProblem', 'Jacobian',
'FinDiffRelStep', rel_step, 'Display', 'iter-detailed', 'OutputFcn',
@opt_outfun, 'Algorithm','levenberg-marquardt', 'MaxIter',10, 'FinDiffType',
'forward', 'TolFun', 1e-3, 'TolX' ,1e-3);
%nonlinear least-squares solver
[x,resnorm,residual,exitflag,output,lambda,jacobian] =
lsqnonlin(@(x) fun_obj(x),ini_para,lb,ub,options);%returns a structure lambda
whose fields contain the Lagrange multipliers at the solution x, and the
Jacobian of fun at the solution x

% Obtain the optimized parameters
opt_para = x;

dlmwrite([para_folder , 'opt_params.txt'],opt_para);
% Run FEM with the optimized parameters and get optimized predictions

```

- Objective Function Calculation

```

function y = fun_obj( paras )
% objective function for optimization

% -----
% Load observation and Weight factors
main_dir = pwd;

%'D:\Google Drive\Excavation_Plaxis models\Feinberg_Inverse_Analysis';

obs_folder = [main_dir , '/observation/'];

    saa1 = dlmread([obs_folder, 'ms_saa1.txt']);
    saa1_weight= dlmread ([obs_folder, 'weight_saa1.txt']);
    saa2 = dlmread([obs_folder, 'ms_saa2.txt']);
    saa2_weight= dlmread ([obs_folder, 'weight_saa2.txt']);
    saa3 = dlmread([obs_folder, 'ms_saa3.txt']);
    saa3_weight= dlmread ([obs_folder, 'weight_saa3.txt']);
    saa4 = dlmread([obs_folder, 'ms_saa4.txt']);
    saa4_weight= dlmread ([obs_folder, 'weight_saa4.txt']);
    saa5 = dlmread([obs_folder, 'ms_saa5.txt']);
    saa5_weight= dlmread ([obs_folder, 'weight_saa5.txt']);
    saa6 = dlmread([obs_folder, 'ms_saa6.txt']);
    saa6_weight= dlmread ([obs_folder, 'weight_saa6.txt']);
    saa7 = dlmread([obs_folder, 'ms_saa7.txt']);
    saa7_weight= dlmread ([obs_folder, 'weight_saa7.txt']);
%     y_obs = [saa1;saa2;saa3;saa4];
%     y_obs = [saa1;saa2;saa3;saa4;saa5;saa6];
y_obs = [saa1;saa3;saa5];
%     y_obs = [saa1];
%     weight = [saa1_weight;saa3_weight];
%     weight = [saa1_weight;saa3_weight;saa5_weight];
%     weight =
[saa1_weight;saa2_weight;saa3_weight;saa4_weight;saa5_weight;saa6_weight];
%     weight = [saa1_weight];

% -----
% Run FEM
y_pred = Run_FEM(paras); % convert ft to inch

%% Build objective function

% y_pred_star prediction corresponds to the observations
y_pred_star = y_pred;

y=(y_pred_star-y_obs).*sqrt(weight);

end

```

- Run FEM

```

function y_pred = Run_FEM( paras)
% Function used to call the python and run FEM calculation

% Note paras is in row vector

% Write parameters into txt for python use
% -----

paras(1)=paras(1)*1e4;
paras(2)=paras(2)*1e4;
% paras(3)=paras(3)*1e4;
% paras(4)=paras(4)*1e-5;
% paras(5)=paras(5)*1e-1;
% paras(6)=paras(6)*1e-1;

main_dir = pwd;
para_folder = [ main_dir , '/parameter/'];
script_folder = [ main_dir , '/scripts/'];
pred_folder = [ main_dir , '/prediction/'];

dlmwrite([para_folder, 'proc_params.txt'], paras);

% Call python scripts
%-----
cd 'D:\Google Drive\Feinberg\Plaxis2D\Hardening Soil
Small\Feinberg_Inverse_Analysis'
python_file = [ 'plxpy2d HS Model.py'];
status = system(python_file);

% obtain the output from FEM
%-----
pred_inclin1 = dlmread([pred_folder, 'pre_inclinometer1.txt']);
pred_inclin2 = dlmread([pred_folder, 'pre_inclinometer2.txt']);
pred_inclin3 = dlmread([pred_folder, 'pre_inclinometer3.txt']);
pred_inclin4 = dlmread([pred_folder, 'pre_inclinometer4.txt']);
pred_inclin5 = dlmread([pred_folder, 'pre_inclinometer5.txt']);
pred_inclin6 = dlmread([pred_folder, 'pre_inclinometer6.txt']);
pred_inclin7 = dlmread([pred_folder, 'pre_inclinometer7.txt']);

y_pred = -
[pred_inclin1(1:22);pred_inclin3(1:22);pred_inclin5(1:22)]*12;
% y_pred = -[pred_inclin1(1:22)]*12; % convert to inch and positive for
movement towards the excavation
% y_pred = -pred_inclin1(1:22)*12;
% y_pred = -pred_inclin2(1:31)*12;
end

```

C. Calculations for weights of SAAs

$$\text{Repeatability} = 1.5 \text{ mm} \cdot \sqrt{\frac{d \text{ (m)}}{32 \text{ m}}}$$

where d is the distance from the fixed end.

$$\text{Weight} = \frac{1}{(\text{Repeatability})^2}$$

Weights corresponding to the Blodgett/Deerfield and Park Ridge layers are shaded in the table.

Table C.1 Calculation for weights of SAA-1

Elevation (m CCD)	d (m)	Repeatability (mm)	Weight
4.22	24.50	1.3125	0.5805
3.72	24.00	1.2990	0.5926
3.22	23.50	1.2854	0.6052
2.72	23.00	1.2717	0.6184
2.22	22.50	1.2578	0.6321
1.72	22.00	1.2437	0.6465
1.22	21.50	1.2295	0.6615
0.72	21.00	1.2151	0.6772
0.22	20.50	1.2006	0.6938
-0.28	20.00	1.1859	0.7111
-0.78	19.50	1.1709	0.7293
-1.28	19.00	1.1558	0.7485
-1.78	18.50	1.1405	0.7688
-2.28	18.00	1.1250	0.7901
-2.78	17.50	1.1093	0.8127
-3.28	17.00	1.0933	0.8366
-3.78	16.50	1.0771	0.8620
-4.28	16.00	1.0607	0.8889
-4.78	15.50	1.0440	0.9176
-5.28	15.00	1.0270	0.9481
-5.78	14.50	1.0097	0.9808
-6.28	14.00	0.9922	1.0159
-6.78	13.50	0.9743	1.0535
-7.28	13.00	0.9561	1.0940
-7.78	12.50	0.9375	1.1378

-8.28	12.00	0.9186	1.1852
-8.78	11.50	0.8992	1.2367
-9.28	11.00	0.8795	1.2929
-9.78	10.50	0.8592	1.3545
-10.28	10.00	0.8385	1.4222
-10.78	9.50	0.8173	1.4971
-11.28	9.00	0.7955	1.5802
-11.78	8.50	0.7731	1.6732
-12.28	8.00	0.7500	1.7778
-12.78	7.50	0.7262	1.8963
-13.28	7.00	0.7016	2.0317
-13.78	6.50	0.6760	2.1880
-14.28	6.00	0.6495	2.3704
-14.78	5.50	0.6219	2.5859
-15.28	5.00	0.5929	2.8444
-15.78	4.50	0.5625	3.1605
-16.28	4.00	0.5303	3.5556
-16.78	3.50	0.4961	4.0635
-17.28	3.00	0.4593	4.7407
-17.78	2.50	0.4193	5.6889
-18.28	2.00	0.3750	7.1111
-18.78	1.50	0.3248	9.4815
-19.28	1.00	0.2652	14.2222
-19.78	0.50	0.1875	28.4444
-20.28	0.00	0.0000	-

D. Calculation of Factor of Safety Against Basal Heave

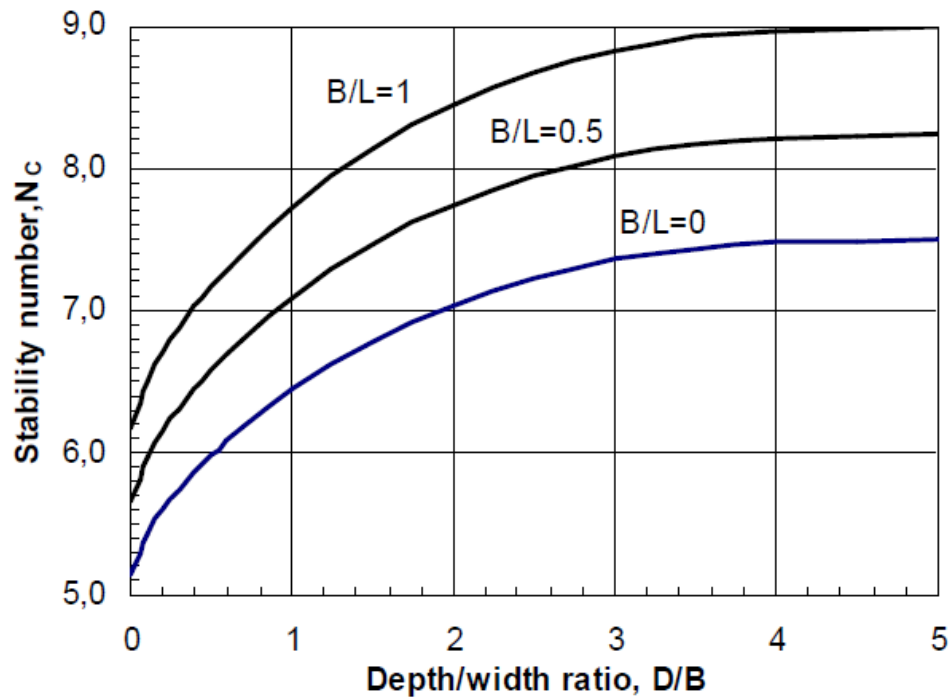


Figure D.1 Stability number with depth/width ratio

- Lurie Center (in SI units)

$$B = 68m$$

$$L = 80m$$

$$B / L = 0.85$$

$$H_1 = 9.8m \quad H_1 / B = 0.14$$

$$H_2 = 12.5m \quad H_2 / B = 0.18$$

$$S_{u(Fill)} = 18.2kPa$$

$$S_{u(Sand)} = 0.2kPa$$

$$S_{u(Blodgett/Deerfield)} = 47.9kPa$$

$$S_{u(ParkRidge)} = 71.8kPa$$

$$S_{u(Hardpan)} = 93.7kPa$$

At Stage 5 (excavation to elev. -5.8 m CCD)

i) When stiff layer is Park Ridge

$$S_{uu} = 11.4kPa$$

$$S_{ub} = 47.9kPa$$

$$\gamma = 18.8kN / m^3$$

$$D = 6.7m$$

$$N_c = 6.3$$

$$FS = 1.8$$

ii) When stiff layer is Hardpan

$$S_{uu} = 11.4kPa$$

$$S_{ub} = 61.3kPa$$

$$\gamma = 18.8kN / m^3$$

$$D = 15.2m$$

$$N_c = 6.3$$

$$FS = 2.2$$

At Stage 6 (excavation to elev. -8.5 m CCD)

i) When stiff layer is Park Ridge

$$S_{uu} = 19.3kPa$$

$$S_{ub} = 47.9kPa$$

$$\gamma = 18.8kN / m^3$$

$$D = 4.0m$$

$$N_c = 6.5$$

$$FS = 1.8$$

ii) When stiff layer is Hardpan

$$S_{uu} = 19.3kPa$$

$$S_{ub} = 64.1kPa$$

$$\gamma = 18.8kN / m^3$$

$$D = 12.5m$$

$$N_c = 6.5$$

$$FS = 1.9$$

- **SQBRC (in US units)**

$$B = 198 \text{ ft} \quad B_3 = 18 \text{ ft}$$

$$L = 221 \text{ ft} \quad L_3 = 20 \text{ ft}$$

$$B / L = 0.90$$

$$H_1 = 35 \text{ ft} \quad H_1 / B = 0.18$$

$$H_2 = 42 \text{ ft} \quad H_2 / B = 0.21$$

$$H_3 = 50 \text{ ft} \quad H_3 / B_3 = 2.78$$

$$S_{u(\text{Fill})} = 380 \text{ psf}$$

$$S_{u(\text{Sand})} = 4 \text{ psf}$$

$$S_{u(\text{Blodgett/Deerfield})} = 1000 \text{ psf}$$

$$S_{u(\text{ParkRidge})} = 1500 \text{ psf}$$

$$S_{u(\text{Hardpan})} = 2000 \text{ psf}$$

At Stage 5 (excavation to elev. -22 ft CCD)

iii) When stiff layer is Park Ridge

$$S_{uu} = 300.5 \text{ psf}$$

$$S_{ub} = 1000 \text{ psf}$$

$$\gamma = 125 \text{ pcf}$$

$$D = 20 \text{ ft}$$

$$N_c = 6.4$$

$$FS = 1.7$$

iv) When stiff layer is Hardpan

$$S_{uu} = 300.5 \text{ psf}$$

$$S_{ub} = 1197.0 \text{ psf}$$

$$\gamma = 125 \text{ pcf}$$

$$D = 33 \text{ ft}$$

$$N_c = 6.4$$

$$FS = 1.9$$

At Stage 7 (excavation to elev. -8.5 m CCD)

iii) When stiff layer is Park Ridge

$$S_{uu} = 417.0 \text{ psf}$$

$$S_{ub} = 1000 \text{ psf}$$

$$\gamma = 125 \text{ pcf}$$

$$D = 13 \text{ ft}$$

$$N_c = 6.6$$

$$FS = 1.7$$

iv) When stiff layer is Hardpan

$$S_{uu} = 417.0 \text{ psf}$$

$$S_{ub} = 1250 \text{ psf}$$

$$\gamma = 125 \text{ pcf}$$

$$D = 26 \text{ ft}$$

$$N_c = 6.6$$

$$FS = 1.8$$

At Stage 9 (excavation to elev. -8.5 m CCD)

i) When stiff layer is Park Ridge

$$S_{uu} = 510.3 \text{ psf}$$

$$S_{ub} = 1000 \text{ psf}$$

$$\gamma = 125 \text{ pcf}$$

$$D = 5 \text{ ft}$$

$$N_c = 8.5$$

$$FS = 7.4$$

ii) When stiff layer is Hardpan

$$S_{uu} = 510.3 \text{ psf}$$

$$S_{ub} = 1361.1 \text{ psf}$$

$$\gamma = 125 \text{ pcf}$$

$$D = 18 \text{ ft}$$

$$N_c = 8.5$$

$$FS = 2.4$$